NANOPOROUS CARBON SCAFFOLDS FOR ENERGY STORAGE APPLICATIONS

by

WARUNI JAYAWARDANA

A DISSERTATION

Presented to the Faculty of the Graduate School of the

MISSOURI UNIVERSITY OF SCIENCE AND TECHNOLOGY

and

UNIVERSITY OF MISSOURI- ST. LOUIS

In Partial Fulfillment of the Requirements for the Degree

DOCTOR OF PHILOSOPHY

In

PHYSICS

2018

Approved by

Eric H. Majzoub, Advisor
Alexey Yamilov, Co- Advisor
Philip Fraundorf
Stephen M. Holmes
Julia E. Medvedeva

PUBLICATION DISSERTATION OPTION

A portion of this dissertation has been prepared in publication format. Although the formatting of these sections follows that of this dissertation, the text has not been changed from the original publication. Therefore, reference cited in these papers appear at the end of each section. Paper I has been previously published in a scientific journal and Paper II is formatted for publication in a scientific journal and is awaiting final review before submission.

Paper I, Pages: 29-71, "Novel Voltage-relaxation GITT and Monte Carlo to Determine Lithium Diffusion and Distribution in TiO_2 and Highly-ordered Nanoporous Hard Carbons", Waruni Jayawardana, Christopher L. Carr, Dongxue Zhao, Eric H. Majzoub, J. Electrochem. Soc. 2018, 165(11), A2824-A2832.

Paper II, Pages: 72-118, "AlH_3 and $LiBH_4$ Confined in N-containing Carbon Scaffolds: A Computational and Experimental Study", Hongyang Zou, Waruni Jayawardana, Xander Benziger, Brennan Dizdar, Christopher L. Carr, James L. White, Farid El Gabaly, Hyunjeong Kim, Kouji Sakaki, Paul Jelliss, Mark S. Conradi, Eric H. Majzoub, Awaiting publication.

ABSTRACT

Nanoporous carbons (NCs) have become increasingly popular in various fields of research due to their unique properties including tunable pore sizes, higher pore volumes and higher surface areas, as well as being able to produce controlled nanostructures. The work presented here uses NC scaffolds with as active hosts for (1) Li-ion battery electrodes and (2) confined metal hydrides (MH) for hydrogen storage applications. In (1) we investigate the Li diffusion characteristics in hard carbons (HCs) that are important for electrochemical applications. We develop a novel method named Voltage-Relaxation Galvanostatic Intermittent Titration Technique (VR-GITT). Parameters derived from the fitting of electrochemical data provide both the diffusion constants as well as morphological information about the diffusion geometry. The VR-GITT method also allows determination of the diffusion constant in the two-phase region of many materials, where the standard GITT method fails. In (2) it is already known that confining MHs in NCs. can alter the kinetics of de/re-hydriding reactions. We investigate the effects of changing the surface electron density in these HCs by the addition of nitrogen (N). The various chemical environments for the surface nitrogens include pyridinic and pyrrolic. The pyridinic N contains a lone pair of electrons that should be available to form Lewis-acid/base complexes that interact with confined MHs, and provide a favorable (wetting) surface energy for incorporation of AlH_3, $LiBH_4$, and other hydrides into the carbons. Our results indicate that both B and Al interact with these pyridinic Ns upon introduction to the HCs. The infiltration of $LiBH_4$ is straightforward, while the infiltration of AlH_3 requires oxygen reduction techniques during the carbon scaffold synthesis.

ACKNOWLEDGMENTS

I would like to thank my advisor, Prof. Eric H. Majzoub, for his tremendous support throughout my PhD. This achievement will not be possible without his guidance and patience. He provided me an excellent work environment to do my research with the help of the other group members and our collaborators.

I would also like to thank my committee members Dr. Philip Fraundorf, Dr. Stephen Holmes, Dr. Julia Medvedeva, and Dr. Alexey Yamilov for serving in my committee as well as for providing me valuable suggestions in different aspects of my work. I really appreciate the help from Dr. David Osborn and Dr. Nigam Rath for helping me to setting up some of the experiments.

I appreciate the given opportunity form the Department of Physics, to pursue my goals. Moreover, I thank the University of Peradeniya, Girls' High School and Sarasavi Uyana Maha Vidyalaya for giving me free education. I convey my gratitude to all the members of physics department who supported me throughout this PhD. I also thank our collaborators from Sandia National Laboratory, Livermore, Washington University in St. Louis and Saint Louis University. I like to thank my former and current group members who helped me in different ways to get hands-on experience on the instruments and for the helpful discussions. I appreciate all my friends for being with me to share the experiences and excitement during life.

Finally, I would like to thank my all family members. I want to thank specially for my late father, mother, brother and my in-laws for supporting me and believing on me. Moreover, my husband Amila for providing care and encouragement all the time.

TABLE OF CONTENTS

Page

PAPER

SECTION

LIST OF ILLUSTRATIONS

SECTION Page

PAPER II

SECTION

LIST OF TABLES

1. INTRODUCTION

1.1. THE GROWING DEMAND FOR ENERGY

Energy is a key ingredient in day-to-day life. The consumption of energy is increasing along with the rapid growth of the planet's population and the advancement of the standard of living. According to International Energy Outlook 2017, energy consumption has been increasing and will continue to increase by 28% between 2015 and 2040.[1] Figure 1.1 represents the predicted energy demand until 2040. This rapid growth of energy demand cannot be fulfilled only by the limited reserves of non-renewable energy sources like petroleum, natural gas, and coal. Use of fossil fuels leads to emission of CO_2 to the atmosphere. Even though, the emission intensity of energy, represented by CO_2 per unit of energy, has decreased from 2011.[2] This is due to the use of lower emission fuels and renewable energy sources, therefore the attention on the production of renewable sources still remains significant. There are several hurdles to overcome when considering renewable energy sources such as the efficiency, reliability and cost effectiveness. Currently, the United States obtains 81 % of its total energy from fossil fuels.[3] It is difficult to find energy sources to compete with coal/fossil fuels. However, considering the existing amount of fossil fuels and global warming, the necessity of clean energy sources has become more important. Extensive research has been focusing on the various aspects of energy related fields over the past few decades. Not only the enhancements of energy related materials but also improved energy storage systems are crucial to accomplish the future energy demand. The research described in this thesis address these two important aspects by developing a novel analysis method for energy

related materials and investigating promising materials for hydrogen energy storage. In order to provide some background information, different energy storage systems and their main features will be discussed in the next section.

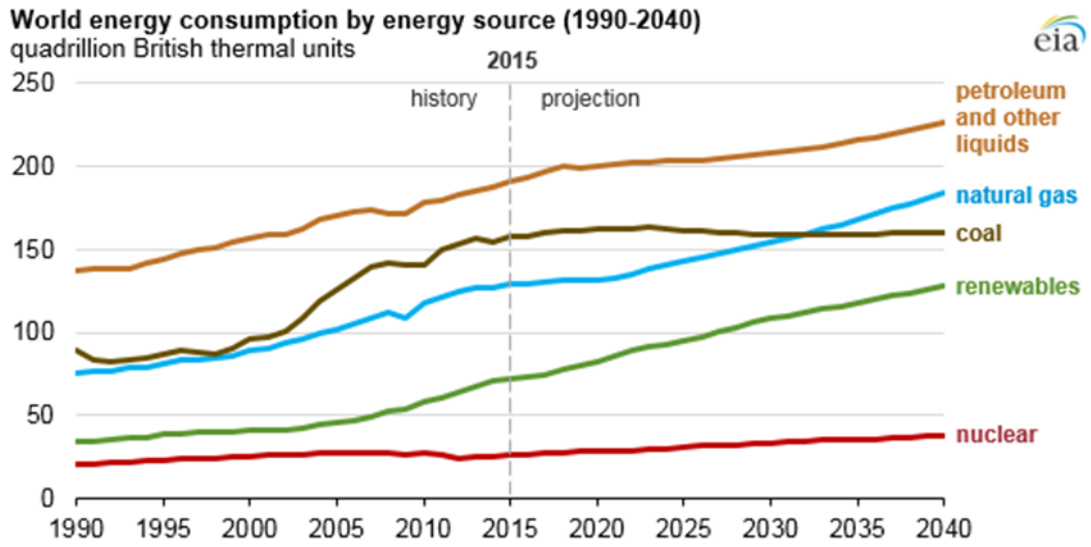

Figure 1.1. Predictions of future energy demand.

1.2. ENERGY STORAGE AND CONVERSION SYSTEMS

Energy storage systems can store energy and deliver it later when the demand is high, helping energy sustainability. Energy comes in numerous forms such as chemical, electrical, potential, radiation, kinetic, and latent heat. There are several different existing energy storage and conversion systems. These systems convert energy from forms which pose a challenge to be conveniently or economically stored. Batteries, fuel cells and super capacitors are the main chemical energy storage and conversion systems. In these systems, chemical energy is converted to electrical energy and vice versa.[4] The main

focus on this thesis is on active materials that are used in batteries and fuel cells. Both of these systems are comprised of an anode, a cathode, and electrolyte and convert chemical energy to electrical energy and vice versa using redox reactions occurring at the electrodes. These two systems differ from the location of the energy storage and conversion. A battery can be identified as a closed system where anode and cathode serve as both charge transfer media and active masses for the redox reactions. In contrast, fuel cells are open systems which acquire active masses from outside the system. Electrodes only act as charge transfer media in fuel cells.[4]

1.2.1. Battery Storage System. Primary and secondary batteries are the two main battery categories. A primary battery can be used only one time, whereas the secondary battery (rechargeable battery) can be reused many times.[4] Figure 1.2 shows a diagram of a Li ion battery system. When the two electrodes are connected from an external circuit, electron flow occurs from the lower potential electrode (negative/anode) to higher potential electrode (positive/cathode). During this process, ions are transported across the electrolyte in order to maintain the charge balance. In secondary batteries, the recharge process can be achieved by applying high voltage between the anode and cathode in the opposite direction of the ion movement.[5]

1.2.2. Fuel Cell System. Fuel cells are mainly used in areas such as portable power generation, stationary power generation and power for transportation.[7] A diagram of a fuel cell is shown in Figure 1.3. Both the hydrogen fuel and the oxidant or oxygen from the air need to be supplied continuously to the system. Hydrogen atoms become ionized due to the catalyst present at the anode and then the positively charged hydrogen ions travel through the electrolyte while the electrons travel through the external circuit.

Finally, they combine with the oxygen atoms at the cathode during the operation process. The anode, cathode and the overall full cell reactions are given in equations 1, 2 and 3 respectively. Fuel cells provide the cleanest energy since their byproducts are only water and heat.

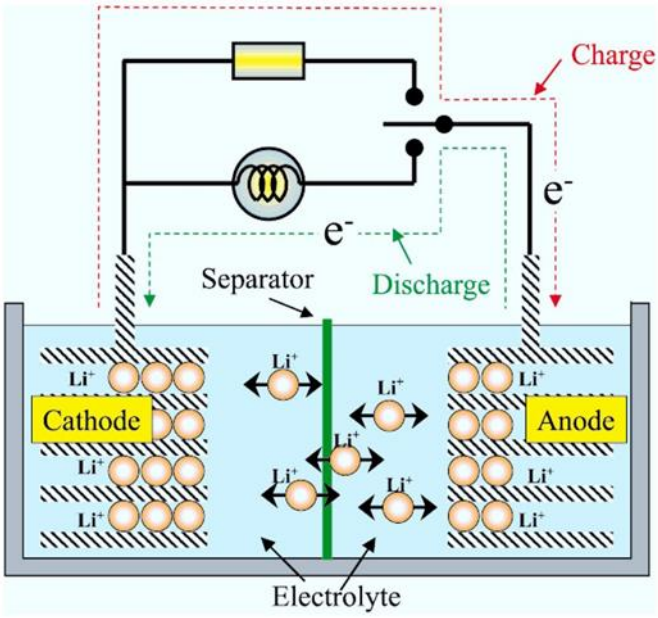

Figure 1.2. Schematic diagram of a Li-ion battery.[6]

Anode Reaction $H_2 \Rightarrow 2H^+ + 2e^-$ (1)

Cathode Reaction $\frac{1}{2}O_2 + 2H^+ + 2e^- \Rightarrow H_2O$ (2)

Overall Reaction $H_2 + \frac{1}{2}O_2 \Rightarrow H_2O$ (3)

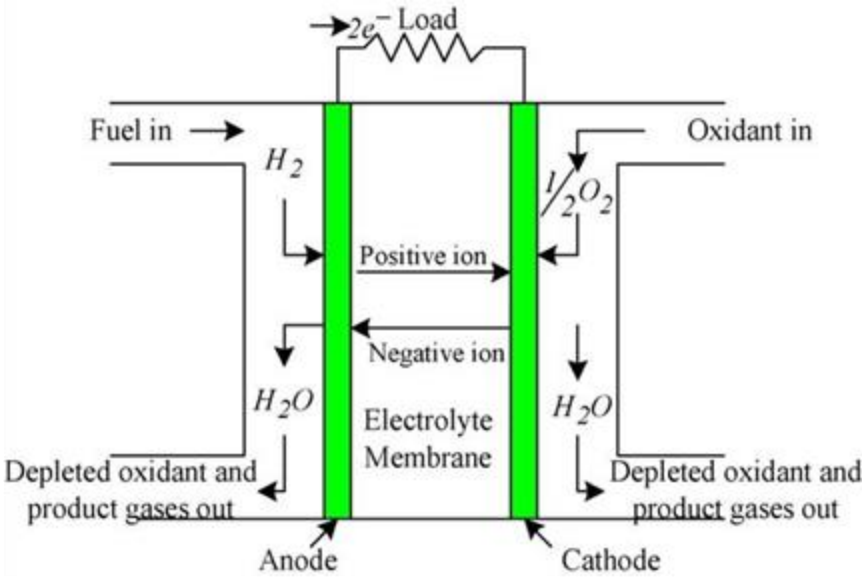

Figure 1.3. Schematic diagram of a fuel cell.[8]

There are different types of fuel cells depending on the choice of the electrolyte and the fuel. The Proton Exchange Membrane (PEM) fuel cell uses a proton conductive polymer as electrolyte. The electrolyte is sandwiched between two porous electrically conductive electrodes. There is a catalyst layer normally made with platinum between the interface of the electrolyte and the porous electrode.[9] The low operating temperature (~100 °C) makes this fuel cell type ideal for automotive vehicles.[8]

1.3. HYDROGEN PRODUCTION AND STORAGE

Hydrogen is an energy carrier, not an energy source. It can carry a tremendous amount of energy and transform its chemical energy to electric energy via a chemical reaction. It has 142 MJ of chemical energy per mass, which is much higher than hydro

carbon fuel.[10] For the fuel cell reaction, oxygen can be obtained from the air. However, hydrogen must be produced and then stored somehow before using it in the fuel cell. Hydrogen can be produced from water, bio mass, natural gas, oil, and gasification of coal.[11] In the US, annually, the highest amount of hydrogen is produced via natural gas reforming.[12] Details of some of the hydrogen production methods and their by-products are as follows. The natural gas reforming process consists of two steps. First, hydrocarbons are split using steam to generate carbon monoxide and hydrogen. Then the water gas shift reaction is used to get hydrogen and carbon dioxide from carbon monoxide.[13] Coal gasification is a very complex process involving several reactions. Generally, in the first stage under high temperature, coal separates into oil, light hydrocarbons, tars and phenols. After that, the mixture is subjected to the water gas shift reaction and finally, undergo methanation.[13] The sustainability of the aforementioned high yielding production pathways are problematic since both natural gas and coal belong to non-renewable energy sources. On the other hand, electrolysis of water and bio mass processing production pathways can use renewable energy sources such as solar energy, wind, and geothermal energy. The amount of hydrogen content in the biomass is small compared to the fossil fuels. For example, the lignocellulosic biomass has four times smaller amount of hydrogen than the natural gas.[13] Using different gasification methods, biomass can be converted into a synthesis gas mixture composed of hydrogen, carbon monoxide, carbon dioxide and methane. Calcium-based carbon dioxide sorbent can be used to maximize the hydrogen content in the mixture.[14] Electrolysis of water is the process of splitting water into oxygen and hydrogen using electric current. This method is the most eco-friendliest method with other advantages such as high purity, simple

process, and abundant sources.[15] However, hydrogen production methods from renewable energy resources needs several improvements/modifications to completely replace hydrogen production from non-renewable sources.

Hydrogen storage plays a key role in the hydrogen economy. It is important to find methods to store hydrogen safely and cost-effectively for use in applications. There are three main ways of storing hydrogen and each method has both advantages and disadvantages associated with them as discussed below. First, hydrogen can be stored in high pressure compressed gas tanks up to 800 bar. This method allows to store higher amount of gas in a small space providing 36 kgm^{-3} volumetric energy density.[16] The other advantage of this method is the simplicity; the ability to use gas phase hydrogen directly from the storage tank. Compressed gas tanks must be light weight in order to obtain higher gravimetric energy densities. Use of carbon fiber reinforced plastic materials is a good solution for this problem.[17] The second method is storing hydrogen in the liquid form inside tanks. This is also called cryogenic storage because, hydrogen needs to cool down to 20 K to maintain the liquid state. The method provides higher volumetric energy densities than the compressed gas storage. For example, a liquid hydrogen tank can store 2.33 times more hydrogen compared to compressed gas tank. The problems related to this method are the need of better insulation for the tanks, higher hydrogen liquification rate, and hydrogen boil off.[10,16,17] As a result of these problems, the energy penalty is high in these cryogenic storage systems. Moreover, when it comes to hydrogen fuel cell vehicles, having an on-board high-pressure hydrogen tank or liquid hydrogen tank can lead to safety concerns.

The third method is material-based hydrogen storage, either through condensation of the gas on some scaffold or forming chemically bound hydrogen. This is the safest way to store hydrogen for on board fuel cell applications. Material-based storage can be divided into two categories, namely physisorption and chemical storage.[10,18] In the physisorption method, generally, adsorption occurs via weak Van-der Waal forces and weak electrostatic forces between the hydrogen and the material surface.[19] There are several studies on hydrogen physisorption on different materials such as zeolite, porous carbons, metal organic frameworks, and covalent organic frameworks.[10,19] The amount of adsorbed hydrogen depends on the surface area and micro/mesopore volumes of the materials. Even though it is a completely reversible process, the higher adsorption amounts can only be obtained at lower temperatures. Introduction of heteroatoms or light metal atoms in to the host framework can increase the amount of adsorbed hydrogen by increasing the binding energy of hydrogen due to dipole interactions. For instance, 4.2 % of hydrogen storage was observed for boron nitride nano tubes with collapsed structure at room temperature.[20]

Materials that can produce hydrogen through a chemical reaction are used in the hydrogen chemical storage systems. Some examples of such materials are ammonia (NH_3), metal hydrides, carbohydrates, synthetic hydrocarbons, and liquid organic hydrogen carriers.[10] One focus in this thesis is hydrogen storage in metal hydrides, which will be discussed further in the next sub section.

1.4. HYDROGEN STORAGE IN METAL HYDRIDES

Some metals, intermetallic compounds, and alloys can absorb hydrogen under moderate pressure and temperature, forming metal hydrides.[21] Due to the absorption, hydrogen can safely be stored in these metal hydrides at lower pressure and higher density state compared to other hydrogen storage methods. Even though storing hydrogen in metal hydrides is safer, the associated weight penalty is problematic for onboard hydrogen storage for transportation applications. Several studies conducted on the metal hydrides area focus on synthesizing new materials to fulfil the requirement of low temperature fuel cell applications. For most of the automotive applications, metal hydrides must have high gravimetric (> 6 wt % H_2 or 2 kW $h^{-1}kg^{-1}$) and volumetric (0.045 kg H_2 L^{-1} or 1.5 kW h L^{-1}) hydrogen densities along with suitable kinetic and thermodynamic requirements at low temperature conditions (~100 °C)[22].

Metal hydrides can be categorized into three groups: (1) Binary hydrides (MH_x), (2) Interstitial Metallic/Intermetallic hydrides (AB_XH_Y), and (3) Complex Hydrides (ME_xH) (E=boron (borohydrides), nitrogen (amides), aluminum (alanates). When metal absorbs hydrogen gas during the formation of the metal hydride, it releases heat exothermally and forms a chemical energy rich metal hydrogen bond. Normally, metal lattice expands about 10-20 % during the formation. During this transition, first solid solution containing small amounts of hydrogen (alpha phase) is formed and then another new phase (beta phase) grows with the increasing amount of hydrogen. As a result, a plateau pressure is observed in the pressure-composition-isotherm (PCT) containing both alpha and beta phases. The heat release during the process can be measured using the

enthalpy parameter from the gradient of the van't Hoff plot, which is derived from the plateau pressures of the PCT at different temperatures.[23]

There are several other uses of metal hydrides apart from the hydrogen storage such as using them in Li-ion batteries[23,24], using them as reducing agents[25] and catalysts[26]. Hydrides, which are important for the hydrogen storage applications will be discussed on the next sub sections as it is one of the focuses on this thesis.

1.4.1. Binary Hydrides. (MH_x). Binary hydrides are the simplest form of hydrides, containing only two elements, one of which is hydrogen. They have a single step decomposition with the decomposition enthalpy similar to the negative of the formation enthalpy. Some of the examples of binary hydrides that show promising results for hydrogen storage and their hydrogen weight percent numbers as follows; AlH_3 (10.1 wt%), MgH_2 (7.7 wt%), and VH_2 (3.81 wt%). Alane (AlH_3) has gained lot of attention as it has higher volumetric hydrogen capacity (148 g/L) than liquid hydrogen. Not only that, it also has high gravimetric hydrogen capacity.[22] This material is a metastable material. It is not thermodynamically stable at room temperature, but it is kinetically stabilized by the surface oxide layers. The decomposition of alane can be written as follows;

$$AlH_3 \rightarrow Al + \frac{3}{2}H_2 \qquad (4)$$

The formation of alane is highly favorable (enthalpy ΔH =7 kJ/mol H_2). So, very high-pressure conditions above 2.5 GPa are needed to reform alane from the Al and H_2 gas.[27] Alane has been known for more than 75 years. First, alane amine and etherate adducts were synthesized in the sixties. Then, first non-solvated form of AlH_3 was synthesized by Chizinsky et al. using an ethereal reaction between $AlCl_3$ and $LiAlH_4$.[28]

After that, Brower et al. prepared six different non-solvated alane phases α, α′, β, γ, δ and ε and a non-solvated or slightly solvated ζ phase using the same method.[29] The most commonly studied alane phases in the literature are α, β and γ.

There have been several studies to investigate alane as a hydrogen storage material. Freshly prepared α, β and γ phases show considerable decomposition below 100 °C.[16] It has also found that higher desorption rates can be obtained by doping alane with small amounts of LiH. [27]

1.4.2. Interstitial/Intermetallic Metallic Hydrides (AB_XH_Y). Normally, Metal 'A' forms stable binary hydrides. Metal 'B' does not form stable hydrides; however, it may help to dissociate hydrogen molecule. Early transition metals, rare-earth metals, or Mg can be used as metal A. Examples for type B metals are Ni, Co, Cr, Fe, Mn, or Al. Metal hydrides can be grouped in to five different categories. Several different types of hydride forms have been investigated for potential hydrogen storage applications**.** Out of these different hydride forms, AB, AB_2, A_2B and AB_5 families have shown promising results for hydrogen storage related applications. Some of the metal hydrides which are grouped into each of these categories are Mg_2NiH_4, $TiFeH_2$, $ZrMn_2H_{3.6}$ and $LaNi_5H_{6.5}$ respectively. Drawbacks of the intermetallic hydrides are low hydrogen storage capacities by weight, slow kinetics, and complicated activation procedures.[21]

1.4.3. Complex Metal Hydrides (ME_xH). Complex metal hydrides composed of light elements, such as Li and Na, have become potential candidates for hydrogen storage applications due to their high hydrogen storage capacities, high hydrogen densities and mild dehydrogenation conditions.[31] Typically, complex hydrides decompose in multiple

steps and may decompose to very stable metals, which are hard to rehydride back to the original form.[32]

Sodium aluminum hydride ($NaAlH_4$), mostly known as sodium alanate, has total of 7.4 wt% of hydrogen capacity. The material has three step decomposition as follows.

$$NaAlH_4 \rightarrow \frac{1}{3} Na_3AlH_6 + \frac{2}{3}Al + H_2, \ 3.7\ wt\ \% \quad (5)$$

$$Na_3AlH_6 \rightarrow NaH + Al + \frac{2}{3}H_2, 1.85\ wt\ \% \quad (6)$$

$$NaH \rightarrow Na + \frac{1}{2}H_2\ ,, 1.85\ wt\ \% \quad (7)$$

Bogdanovic et. al showed that this material can release and absorb 5.6 wt % (only first two steps of the decomposition) of hydrogen when doped with $TiCl_3$ or Ti-alkoxide catalyst.[33] This discovery gained lot of attention towards the complex metal hydrides as hydrogen storage materials.

Moreover, complex metal hydrides like $LiBH_4$, which has very high gravimetric capacity (18.5 wt %) and high volumetric density (121 kgm^{-3}), are investigated as hydrogen storage materials.[34] The main problem with $LiBH_4$ is the inability to rehydride it back under moderate temperature and pressure conditions.

1.5. NAOPOROUS CARBON SCAFFOLDS FOR ENERGY STORAGE

Nanoporous carbons have several unique properties, which are favorable for energy conversion and energy storage applications, including Li ion batteries[35–37] , hydrogen storage materials[38–40] and supercapacitors[41,42]. Apart from the chemical inertness, electrical conductivity and higher stability of regular carbon materials, these

nano porous carbons have highly ordered structures with higher pore volumes and surface areas, tunable pore sizes, and the ability to dope with hetero atoms without destroying the framework. Use of these materials for energy storage applications provides advantages in many ways. Examples of these numerous advantages include: higher surface areas provide a large number of interaction sites for absorption processes, large pore volumes are beneficial to load guest species into the framework for different applications and to reduce the strain relaxation and expansion during electrochemical cycling. Moreover, uniform and tunable pore sizes help to transport of atoms, ions and large molecules through the bulk material.[43]

1.5.1. Introduction to Nanoporous Carbon Materials. According to the International Union of Pure and Applied Chemistry (IUPAC) definition, porous materials can be classified into three groups based on their pore sizes: microporous (< 2 nm), mesoporous (2-50 nm) and macroporous (> 50 nm). There are two currently existing methods to synthesize porous carbon scaffolds with well-defined pores and narrow pore distributions: hard templating technique and soft templating technique.[44–47]

The hard-templating technique uses pre-synthesized templates to obtain the required structures. These templates do not interact chemically with the carbon precursors. Normally, the template material is washed away at the end of the preparation process. Fist type of highly ordered mesoporous carbon (CMK-1) was prepared from MCM-48 hard template in 1999 with uniform 3 nm pore diameters.[48] This finding opened up the path for so many other ordered carbon structures. Some of the examples for silica templates that can be found in the literature are SBA-15, MCM-48, SBA-1, SBA-16, KIT-6 and KIT-5.[49–52]

In the soft templating technique, the assembly process occurs through self-assembly which is mainly depend on the chemical interactions between carbon precursor and template.[53] In order to obtain mesoporous carbon using soft templating method precursor materials must have the ability to self-assemble into nanostructures, the mixture should contain at least one of pore-forming component and carbon-yielding component, the pore-forming material should have ability to survive during the curing temperature but need to decompose during carbonization, and the carbon yielding component should be able to form highly cross-linked polymeric material.[53] There are very few materials that can fulfil these requirements. Two different soft templating systems namely Poly(ethylene oxide)-b-poly(propylene oxide)-b-poly(-ethylene oxide)(PEO-PPO-PEO)/ Resol system and PEO-PPO-PEO)/Resol formaldehyde/silica system was used in the projects discussed in this thesis to synthesis nanoporous carbon.

The nanoporous carbons examined in various chapters of this thesis can be categorized into two groups: CMK3 (hard templating method) and NPC (soft templating method). NPC has higher surface areas, pore volumes and higher average pore size compared to CMK3 group. Generally, NPC material exceeds 1000 m^2/g surface area with ~1.5 cc/g pore volume.

1.5.2. Nanoporous Carbon for Hydrogen Storage Applications. Nanoporous carbon can be used to alter thermodynamics and kinetics of the metal hydrides through nanoconfinement. It is well known that nano sized materials have different properties with respect to their bulk material.[56] Nanoconfinement can be obtained by melt infiltration or solution impregnation. In the metal hydrides, nanoconfinement provide

large surface area-to-volume ratios yielding higher specific surface area for the hydrogen to exchange. Moreover, it reduces the hydrogen diffusion distances within the material.[57]

According to previous studies it has been found that systems like $LiBH_4$ incorporated into porous carbon[39] and NaAlH4 incorporated into porous carbon[39,58,59,60] show enhanced desorption properties as well as improved reversibility. In addition, Gao et al. has observed formation of nanosized $NaAlH_4$ instead of Na_3AlH_6 during cycling indicating a shift of the thermodynamic equilibrium after melt infiltration.[60] Functionalized carbon have been used to investigate the chemistry between the infiltrated material and the carbon scaffold. In a previous study by our group revealed that $LiBH_4$ infiltrated into nitrogen doped carbon is kinetically stabilized compared to the nonfunctionalized carbon scaffold. More details of this system will be investigated as a part of this thesis project.[61]

Functionalization of nanoporous carbons adds additional properties for these carbons. Ordered mesoporous carbons have synthesized with various organic or inorganic functional moieties such as hetero atoms, amines, metal nanoparticles, metal oxides according to previous reports.[54] Doping of hetero atoms (B, N, S, and P) substitutes some carbon atoms from the carbon structure. This leads to alter the electronic, electrical and surface charge properties of the resulting material.[55] Specifically, nitrogen doping and the effects from the nitrogen doping on the metal hydrides will be discussed in this thesis.

1.5.3. Nanoporous Carbon for Li-ion Batteries. Ordered Nanoporous carbons have been investigated as both anode and cathode material because of their higher pore volume, interconnected mesopore channels and nanosized mesopore walls.[62,62] These properties help to improve the performances of Li-ion battery by facilitating faster ion

transport and accommodating the strain relaxation during charging and discharging. There are several studies in the literature on composite negative electrode materials made with combining porous carbon materials and materials such as SnO_2,[63,64] TiO_2[65] and MnO_2[66].

Pure forms of nanoporous carbons are also used in anode materials. A study shows that carbon derived from inorganic-organic-surfactant tri-constituent co assembly method can deliver better capacity values compared to the carbon made from organic-organic di-constituent assembly. Also, the study shows 500 mAh/g of capacity retention even after 50 cycles for the material.[36] In another study by Sakia et al. two different mesoporous structures (CMK3 and CMK8) were investigated electrochemically and found that the CMK8 has more favorable prosperities like higher reversible capacity, better cycling ability and rate capability.[35]

1.6. LITHIUM DIFFUSION IN ELECTRODE MATERIALS

There are several electrochemical techniques such as Galvanostatic Intermittent Titration Technique (GITT), Electrochemical Impedance Spectroscopy (EIS), and Potential Intermittent Titration (PITT) to find the Li diffusion coefficient inside an electrode material.[67,68,69] The GITT is one of the most widely used diffusion measurements in the literature. This method composed of series of short current pluses followed by a long relaxation period. GITT was first introduced by Weppner and Huggins in 1977 for a mixed conducting Li_3Sb electrode system. In this study, diffusion coefficients were obtained for a planer geometry assuming the diffusion process follows Fick's law inside the electrode.[70]

Even though the GITT method is extensively used to calculate diffusion coefficients, this method is not applicable along a voltage plateau. As a result, GITT is not viable method to calculate diffusion coefficients along the plateau in two phase materials such as TiO_2[71], olivine $LiFePO_4$[72] and spinel $Li_4Ti_5O_{12}$[72]. In this thesis we will be using a stretched exponential function to analyze the relaxation curve obtained from the GITT and use the extracted time constant to calculate the diffusion coefficients along with the particle size. The advantages associated with this new Voltage-relaxation GITT (VR-GITT) are the ability to use it for both one-phase and two-phase materials and the ability to obtain geometry related information.

1.7. OUTLINE OF WORK

The work presented here is related to the energy storage applications; specifically, Li ion batteries and nanoconfined metal hydride systems for PEM fuel cells.

In section two, detailed descriptions of the experimental methods such as preparation of different carbon scaffolds, preparation of coin cells, various characterization methods and analysis used in the work are presented.

Paper I is a previously published study which contains Li diffusion measurements for both carbon and TiO_2 materials together with computational approach to calculate Li distribution inside the electrode materials using reverse Monti Carlo method. The diffusion analysis method, Voltage-relaxation Galvanostatic Intermittent Titration Technique (VR-GITT) employed in the work is a newly developed method using stretched exponential.

Paper II contains a study about interactions between carbon scaffold and metal hydrides. In here, AlH_3 infiltrated carbons and $LiBH_4$ infiltrated carbons were investigated using XRD, NMR, and gas desorption measurements.

Section three includes desorption measurements and results on the nanoconfined $NaAlH_4$ with and without the nitrogen functionalization. Finally, last section contains main conclusions of the entire work presented in the thesis.

2. EXPERIMENTAL METHODS

A number of different experimental techniques were used to characterize and investigate our systems. In this section those experimental procedures are discussed in detail. This chapter is divided into three subsections. In the first subsection synthesis and characterizations of nanoporous carbons are discussed which were used as anode materials in the coin cells and as the substrate for the infiltration of metal hydride materials in the following sections. Then, preparation and electrochemical measurements for the Li-ion coin cells is presented in the second subsection. Finally, characterizations and thermal investigations for infiltrated metal hydrides are described in the third subsection.

2.1. SYNTHESIS AND CHARACTERIZATION OF NANOPOROUS CARBONS

In this following section preparation of different carbon types are discussed followed by the characterization methods.

2.1.1. Sample Preparation. In this section specific carbon preparations are described in detail. As discussed in the introduction, both soft templating and hard templating carbon synthesis procedures were employed to get nanoporous carbons in different projects. These carbons were prepared using previously published literature.[41,44–47,73]

2.1.1.1. Soft templated carbon. Two types of soft templating techniques were used as discussed below. They are organic-organic self-assembly and organic-inorganic

self-assembly. The main component for soft templating method is resol precursor. It can be synthesized from the following procedure.

- Resol precursor preparation. First, 6.1 g of phenol was melted in a shlenk flask at 40 °C. Then, 1.3 g of 20 wt% NaOH solution was added under stirring. After 10 minutes, 10.5 g of formalin was added dropwise using a syringe. The mixture was maintained under 50 °C throughout the process. Then, the temperature of the mixture was raised to 70 °C and stirred for 80 minutes. Next, 1N HCl was added dropwise to neutralize the mixture after cooling it to room temperature. The solution was vacuumed at 45 °C to remove the water. Ethanol was added to dissolve the resulting gel like product yielding 20 wt% resol-ethanol final mixture. Then, the solution was allowed to settle overnight. Finally, the supernatant resol-ethanol mixture was poured to separate flask and used for the next processes.
- Organic-organic self-assembly method. In a typical procedure, 10 g of F127 was dissolved in 200 g of ethanol. Then, 50 g of resol precursor was added and stirred for 10 minutes to obtain a homogeneous mixture. Next, the solution was poured into dishes and heated in the oven at 100 °C for 24 hours. The resulting transparent films were scraped and crushed into fine powders. Calcination (350 °C) and carbonization (800 °C) were carried out in the tube furnace with 2.4 % O_2/N_2 gas mixture. The heating ramp rate was 1 °C/min below 600 °C and 5 °C/min above 600 °C.

- Organic-inorganic self-assembly method. In a typical procedure, 8 g of Pluronic F-127 tri-block co-polymer and 7.5 g of dicyandiamide was added to a mixture of 100 g of ethanol, 50 g of H_2O, and 10 g of 0.2 M HCl. Resol-ethanol solution and 10.4 g of tetraethyl orthosilicate (TEOS) were added to the mixture stepwise followed by a stirring step of 1 hour at 40 °C. Then, the whole mixture was stirred for another 2 hours at 40 °C. The mixture was poured into glass pans and placed in an oven at 45 °C for 8 hours. Resulting uniform films were thermopolymerized at 100 °C for 24 hours. Next, the obtained film was scraped from the pan and ground into a fine powder. Then, the calcination and the carbonization were carried out at 250 °C for 2 hours and 700 °C for 3 hours respectively under flow of nitrogen gas. The silicate was removed by etching the carbon with 5 wt % HF solution for two days followed by a washing step with deionized water and ethanol. Finally, the carbon sample was dried at 100 °C to remove the remaining moisture due to washing step.

2.1.1.2. Soft templated carbon with nitrogen functionalization. In a typical procedure, first, 100 g of ethanol, 50 g of H_2O and 10 g of 0.2 M HCl was added into a flask. Then, 8 g of F-127 tri-block co-polymer and 7.5 g of dicyndiamide are added to the solution. After 1 hour stirring at 40 °C, 10.4 g of TEOS and 25 g of 20 wt% resol-ethanol solution were added and continued stirring for another 2 hours at 40 °C. After that, the mixture was transferred into glass pans and placed in an oven at 45 °C for 8 hours for the solvent evaporation. Next, thermopolymerization was carried out by baking the resultant films at 100 °C for another 24 hours. The films were scraped from the pans and ground

into fine powder. Calcination and carbonization process were done under nitrogen gas at 250 °C for 2 hours and 700 °C for 3 hours respectively. Silicate was removed by etching with 5 wt% HF solution for two days under stirring. Then, the carbon sample was washed with deionized water and ethanol and dried at 90 °C for 12 hours.

2.1.1.3. Hard templated carbon. First, 6.25 g of sucrose was dissolved in 0.7 g of H_2SO_4 and 25 g of H_2O mixture. Then, 5 g of the hard-templating material (SBA-15) was added to the mixture and stirred for 15 minutes. A white color slurry was obtained after mixing step. Next, the mixture was subjected to two heat treatment steps at 100 °C for 6 hours and 160 °C for 6 hours. The resulting black/brown powder was again added to a mixture containing 4 g of sucrose, 0.45 g of H_2SO_4 and 25 g of H_2O mixture and stirred for 25 minutes. After that, previously mentioned two heat treatments were repeated for the sample. The carbonization was performed at 900 °C with a ramp rate of 1 °C/min below 600 °C and 5 °C/min above 600 °C temperature. The process was carried out under argon gas for 3 hours in the tube furnace. The hard template was removed by etching the carbon with 5 wt % HF solution. Etching process was continued for two days and washed with deionized water and ethanol. Finally, the carbon sample was dried at 100 °C in the drying oven.

2.1.1.4. Hard templated carbon with nitrogen functionalization. First, 6.75 g of ethylenediamine (EDA) and 15 g of carbon tetrachloride (CTC) were added to a jacketed flask at room temperature. Next, 2.5 g of SBA-15 silicate template was added slowly while stirring the mixture to obtain homogeneous mixture and after the addition the complete mixture was allowed to stir another 1 hour. Then, the temperature of the mixture was increased to 90 °C and refluxed for 6 hours. The resulting brown color solid

was placed in a drying oven at 100 °C for 12 hours. After that, the solid was ground into a fine powder and carbonized in the tube furnace. The carbonization temperature, ramp rate and the duration were 600 °C, 3 °C/min, and 5 hours respectively. 5 wt% HF was used to remove the silica template from the carbon/silica composite. The process was carried out by stirring the carbon/silica composite with HF acid for two days followed by a washing step with the ethanol. Finally, carbon was dried at 90 °C for 12 hours to get a dry carbon powder.

2.1.2. Nitrogen Adsorption Desorption Measurements. Nitrogen adsorption desorption isotherms were measured from SA3100 (Coulter) analyzer at 77 K. First, all the carbon samples were outgassed at 300 C for 12 h, and then loaded in to the sample glass values inside the glove box (O_2< 1 ppm, and < water 0.5 ppm). The Brunauer-Emmett-Teller (BET) method was used to calculate the specific surface area (S_{BET}) from the adsorption isotherm branch in a relative pressure range from 0.02- 0.5 bar. Both total pore volume (V_{Total}) and the pore size distributions were calculated using Barrett-Joyner-Halenda (BJH) method. The total pore volume was estimated from the adsorbed amount at a relative pressure P/P0 of 0.98.

2.1.3. Scanning Electron Microscope (SEM). Particle sizes of the different carbon samples were measured using the SEM images. First, double sided tape was attached to the sample holder. Then, a small amount of carbon powder was spread on the tape. Next, the sample was inserted into the SEM machine and let it to vacuumed for 3 hours. Finally, a SEM of images were obtained at different magnifications.

2.2. EXPERIMENTAL MEASUREMENTS FOR LI-ION BATTERIES

In this following section preparation of coin cells and electrochemical measurements are discussed.

2.2.1. Preparation of Coin Cells. First, carbon materials were baked at 300 °C and polyvinylidene fluoride (PVDF) (301F) at 110 °C using custom built Sievert type apparatus respectively overnight. The purpose was to remove moisture from the electrode materials. The whole assembly process was done inside an argon filled glove box with oxygen and water content below 1 ppm. Next, carbon, PVDF and N-methyl-2-pyrrolidone (NMP) was mixed using a mortar and pestle to obtain a homogeneous mixture. In the process, carbon was used as active material, PVDF was used as binder and NMP was used as solvent. The ratio between active material and binder was 9:1. Normally, carbon black is added to get good thermal conductivity. Since the goal is to measure diffusion in the pure forms of carbon, no carbon black was added in the preparation. Electrodes were prepared by coating a thin layer of the slurry on a battery grade Cu foil. These electrodes were baked at 70 °C for 10 minutes and then again at 120 °C for overnight inside the glove box. Coin cells were assembled with a metallic lithium chip as a reference/counter electrode and a carbon electrode as the working electrode. 1 M $LiPF_6$ in a mixture of 1:1 ethylene carbonate (EC) and diethylene carbonate (DEC) was used as the electrolyte. Two layers of separators (Celgard brand) were sandwiched between Li metallic chip and the working carbon electrode with a few drops of electrolyte. Finally, a coin cell was sealed under pressure of 50 kg/cm^2 using MTI; MSK 110 hydraulic crimping machine using negative and positive caps (CR2032, 20d*3.2 mm). During the sealing, a spacer and a wave spring was used additionally to obtain a

better seal and a good alignment inside the coin cell. Some of the steps of coin cell preparation is shown in Figure 2.1.

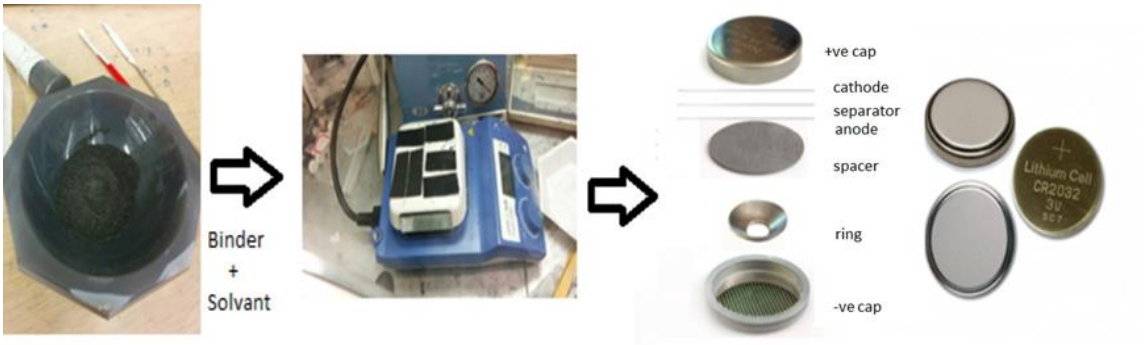

Figure 2.1. Different stages of Li-ion battery preparation process.

2.2.2. Electrochemical Measurements. Electrochemical measurements were taken from the Maccor 4300 instrument. All cells were rested for at least two hours to saturate before taking any measurements. Cycling temperature was assumed to be constant (room temperature) throughout the experiments.

2.2.2.1. Capacity measurements. To obtain capacity values coin cells were cycled between 0.00 V - 3.00 V. The current used in the experiment was 30 mA/g. The mass of the mass of the electrode was obtained from difference between the empty Cu electrode and the coated Cu electrode. The mass of the active material mass of the electrode was calculated using the ratio between carbon and the PVDF.

2.2.2.2. Diffusion measurements. Diffusion Coefficients were measured from the Galvanostatic Intermittent Titration Technique (GITT). This method is composed of constant current pluses followed by a relaxation period. Normally, current pluses are short compared to the rest pluses in order to provide enough time to redistribute the Li

ions inside the electrode. Electrodes that were cycled before for capacity measurements were used to avoid the effects from the solid electrolyte interphase (SEI). In the measurements, 15 minutes current pulses with an approximately C/2 current and 4 hours of relaxation were used. The C value was calculated based on the cycling measurement results for each battery. The insertion of Li ions was carried out until the voltage of the cell reaches 0 V.

2.3. EXPERIMENTAL MEASUREMENTS FOR NANOCONFINED METAL HYDRIDES

In this following section infiltration procedures for AlH_3 and $LiBH_4$ discussed followed by the characterization of those samples.

2.3.1. Sample Preparation. Two different methods for confining metal hydrides were used in the experiments. They are solution infiltration and melt infiltration. AlH_3 infiltrations were performed by the Saint Louis University. All the carbon samples were baked at 300 °C overnight under vacuum to remove moisture prior to the infiltration.

2.3.1.1. AlH_3 infiltration. Solution infiltration was carried out with approximately 1:1 and 1:10 ratios of AlH_3: carbon. In a typical loading procedure, first carbons were suspended in a ~ 6 ml of Toluene and then added calculated amount of dimethylethylamine alane (DMEAA) in to the solution. Next, mixture was continuously stirred for 3 days. After three days, carbons were allowed to settle down to the bottom of the flask and supernant was removed. Finally, carbon samples were vacuumed to remove residual solvents. In the lower doping samples, to remove the excess DMEAA, samples were washed using toluene until no DMEA NMR peaks observed from the solution 1H

NMR. This step cause to remove some of the added DMEAA from the mixture and hence the exact final loading between AlH3: carbon was unknown in the system.

Higher loading samples were made without the washing step with toluene. Two different vacuum temperatures (25 °C and 40 °C) were used in the higher loading sample preparation in order to investigate the temperature effect on the final product. Finally, for the comparison DMEAA powder was made by vacuuming the commercially bought DMEAA liquid at 25 °C.

2.3.1.2. $LiBH_4$ infiltration. Melt infiltration of carbon with LiBH4 was carried out using the Sievert type apparatus set up. The targeted pore filling was 30% of the substrate. The calculation was based on the total pore volume of the substrate and the mass and the bulk density (0.666 g/cm3) of the LiBH4. Prior to the packing inside the stainless-steel sample holder, the mixture was evenly mixed using mortar and pestle for about 15 min. After that, mixture was heated to 300 □C, soaked for 40 min under 100 bar of H2 pressure and allowed to cool to room temperature under pressure.

2.3.2. X-Ray Powder Diffraction Measurements. XRD measurements were performed with Cu Kα radiation source on a Rigaku Ultima IV multipurpose X-ray diffraction system. Mylar film was used to cover the sample during the measurements. This prevent the sample contacting with air and moisture.

2.3.3. Desorption Measurements. A custom-built Sievert type apparatus with calibrated fixed volumes was used to obtain these measurements. The system is consisted with two gas ports (He, H_2) and a vacuum port. Sample temperature and manifold temperatures are measured using type K thermocouples. The system is connected with the computer to automatically record the pressure and **temperature values of the**

manifolds and the sample. The stainless-steel sample holder can use to handle air sensitive materials. Normally, samples are loaded inside a Ar filled glove box (O_2 < 1ppm) and transported to the set up with closed manual value. After connecting the sample holder to the end port, the manual valve is slowly opened to connect the sample with the rest of the set up. Samples are heated using a cylindrical resistive heating element which is connected to PID controller. During the heating process, both sample holder and heating element is wrapped with glass fiber blanket to minimize the heat dissipation.

For the desorption measurements samples were heated with 4 °C/min rate while collecting the released gas into the fixed volumes. Pressure correction calculation was performed for the raw pressure data using ideal gas law equations. This step was performed to remove the pressure increasement due to heating of the gas. The weight percent numbers were calculated using the hydride mass and the previously measured system volumes.

PAPER

I. NOVEL VOLTAGE-RELAXATION GITT AND REVERSE MONTECARLO TO DETERMINE LITHIUM DIFFUSION AND DISTRIBUTION IN TiO_2 AND HIGHLY-ORDERED NANOPOROUS HARD CARBONS

Waruni Jayawardana, Christopher L. Carr, Dongxue Zhao*, Eric H. Majzoub

Center for Nanoscience and

Department of Physics and Astronomy

University of Missouri – St. Louis

St. Louis, MO 63121

*Current address: Department of Physics, Greenville University, Greenville, IL 62246

ABSTRACT

Amorphous hard carbons (AHCs) and metal oxides such as TiO_2 are of interest in applications for energy storage including pseudo/super-capacitors and lithium-ion batteries. We present measurements of lithium diffusion and distribution in anatase TiO_2 and several ordered AHCs prepared by soft/hard-templating techniques, some with capacities > 800 mAh/g. The investigated AHCs have surface areas between 60-937 m^2/g and pore volumes between 0.04-1.01 cc/g. Li-diffusion was measured using two complimentary techniques (1) Galvanostatic Intermittent Titration Technique (GITT), and (2) a stretched exponential to investigate the voltage-relaxation (VR) GITT curve. VR-GITT provides two parameters related to (i) the geometry through which the diffusion is occurring, and (ii) a time scale yielding the diffusion constant with

knowledge of an appropriate length scale. Both methods find diffusion constants in very good agreement with each other. Most importantly, the VR-GITT fitting parameters serve as a distinctive characterization tool and are able to distinguish between AHCs with different pore geometries and synthesis techniques. Further analysis of the VR curves was performed by numerical integration of the diffusion equation and reverse Monte Carlo simulated annealing to investigate the Li density profile in both TiO_2 and the carbons, and suggest that lithium may plate nanopores of AHCs.

1. INTRODUCTION

State-of-the-art Li-ion battery anodes in commercial consumer electronic devices are based on graphite, with a maximum theoretical specific capacity of LiC_6, of 372 mAh/g. Potentially viable anode materials, which include Sn and Si have high specific capacities of 994 mAh/g and 4200 mAh/g respectively, exceeding the capacity of graphite, and therefore are desirable alternatives.[1] Amorphous hard carbons have been extensively investigated as anode materials for Li-ion applications.[1–7]

Hard carbons (HC) are disordered materials; any graphitic domains present have very short coherence length (10-20 nm) as measured by X-ray diffraction.[8] HCs made with phenolic resins, as opposed to carbon sources such as sucrose, start with aromatic structures and can have more extended fullerene-like order depending on the carbonization temperature.[9] HCs compared to commercially available graphite show higher Li-ion capacity, but lower rate capabilities. For example, Ni et al. has demonstrated that HCs derived from phenolic resins can deliver 526 mAh/g capacity, which is about 40% higher than graphite.[2] The main drawbacks of hard carbons are large

irreversible capacity, the hysteresis in the voltage profile between charge and discharge cycles, and the low density of materials.[1,3–5,10]

Previous research on non-ordered hard carbon materials for Li-ion battery applications include studies of irreversible/reversible capacity reduction[6,7,11], understanding the Li insertion mechanisms[12–14] and improving capacity by doping with other materials.[15,16] Buiel et al. has discussed reducing the irreversible capacity by 50 mAh/g by applying ethylene gas using a chemical vapor deposition technique to minimize the air exposure of the materials.[6] Also, in another published report by Buiel et al., it has been shown that reversible capacities are decreasing due to the formation of fullerenes inside the micro pores with the increasing heat treatment temperature.[11] Guo et al. has demonstrated that reversible capacity of 1675 mAh/g can be obtained by a composite of SiO_2 and hard carbon prepared by a hydrothermal reaction.[15]

Ordered hard carbons have also been investigated as anode materials due to their unique properties. Li et al. has conducted a study to analyze the electrochemical properties of ordered mesoporous carbon prepared by the inorganic-organic-surfactant tri-constituent co assembly method and found that the material can deliver reversible specific capacity of 1048 mAh/g along with good cycling ability and capacity retention of 500 mAh/g even after 50 cycles.[17] A comparative study has been conducted by Saikia et al. to investigate two different ordered mesoporous structures, namely CMK3 and CMK8 for anode materials and shown that CMK8 structure has more favorable properties like higher reversible capacity, better cycling ability and rate capability than CMK3.[18]

Apart from a Li ion battery material, hard carbons can be used in several other energy related applications. Hard carbons have unique properties such as chemical

inertness, higher stability, ordered structures with higher pore volumes and surface areas, the ability to introduce hetero atoms into the surface without destroying the structures, and tunable pore sizes.[2,3,19,20] These properties of carbon are beneficial in hydrogen storage applications,[21–26] super capacitors,[20,27] and in the latest Na-ion battery technology[14,28]. In hydrogen storage materials mesoporous carbons can be used for the nanoconfinement of metal hydrides, which allows one to alter the thermodynamic and kinetic properties with respect to the bulk hydrides. Hard carbon materials have been used as a substrate for infiltration of different metal hydrides including $LiBH_4$[21,22], $NaAlH_4$[23], $Li_4BN_3H_{10}$[24]. Liu et al. has investigated the decomposition and wetting behavior of confined $LiBH_4$ inside nanoporous hard carbon prepared from low temperature pyrolysis of phenolic resins and found that the diborane gas release can be eliminated by confining the $LiBH_4$ in 2 nm pores. Lowering of the desorption temperature of $LiBH_4$ compared to the bulk is also observed when it is confined in the ordered nanopores of the carbon.[21] Supercapacitor electrodes made with template based hard carbon materials which have 3D structures and controllable pore sizes can deliver high specific capacitance; approximately 100-300 Fg^{-1} in aqueous medium and 50-150 Fg^{-1} in organic medium.[20]

Moreover, hard carbons may be used in solid-state batteries for confinement of active materials such as conversion reactions where limited diffusion of reactants may improve reversibility. Additionally, solid electrolytes at the forefront of research contain fast Li-ion conductors[29-32] may be interfaced with hard carbon materials where the diffusion of Li at the interface becomes important to control the electronic and ionic conductivities between solid electrolyte and the electrode surface. For example, mixed

conductive Li_2S nano composite electrodes can be made with Li_2S as active material, polyvinylypyrrolide (PVP) as the carbon source, and Li_6PS_5Cl as solid electrolyte in ethanol for all solid state lithium sulfur batteries.[33] $LiBH_4$ also can be used as solid electrolyte together with composite electrodes made with elemental sulfur and carbon additives.[31] In the NASICON type solid electrolytes better electron conduction can be obtained by mixing the materials with single wall carbon nano tubes for all solid state lithium oxygen batteries.[32]

The use of alternative carbon-based anodes requires detailed diffusion investigation to understand the Li diffusion mechanisms inside these carbons. Moreover, proper diffusion analysis would reveal information about favorable structural properties of electrode materials for battery applications. Even though several studies have been conducted to analyze electrochemical properties such as capacity, rate performance, and charge-discharge performance of ordered mesoporous carbons, only a few diffusion analysis studies have been reported in the literature. To the best of our knowledge, this is the first detailed diffusion study conducted on pure forms of ordered mesoporous carbons synthesized by organic-organic di-constituent assembly (NPC-1), organic-inorganic-surfactant tri-constituent assembly (NPC-2) and nanocasting method (CMK3) carbon materials.

The nanoporous hard carbons discussed in this work are highly ordered, with well-defined pore structure. These carbon materials have surface areas in excess of 600 m^2/g, pore volumes between 0.4-1.5 cc/g and uniform pore size distributions. Two synthesis techniques used to obtain our ordered carbons are (1) nanocasting that uses a

hard silicate template, and (2) soft templating, which uses organic-organic or organic-inorganic self-assembly processes.[34–37]

Diffusion measurements: There are several electrochemical techniques for determining diffusion coefficient of Li ions inside a host material. The Galvanostatic Intermittent Titration Technique (GITT)[38], electrochemical impedance spectroscopy (EIS), and potential intermittent titration (PITT) are some examples of such techniques.[39] GITT is one of the most widely used diffusion analysis methods in the literature. Diffusion coefficients are calculated based on the voltage response during the current pulse and the equilibrium voltage change after the relaxation is complete. The diffusion constant calculated from the original GITT presentation was derived assuming that the diffusion process inside the electrode follows Fick's Law.[38]

Although the GITT process has been known for some time, it was designed to measure the diffusion constants during the current pulse and there is much less work on the voltage response during the relaxation. In this work we introduce a variation on the GITT technique based on an analysis of the voltage relaxation *between* current pulses. We refer to this as voltage-relaxation GITT or VR-GITT. This method uses the same experimental procedure as GITT, but employs a stretched exponential to analyze the relaxation data instead of the voltage response during the galvanostatic current. From the stretched exponential one obtains a time constant representing the time Li ions take to redistribute after each current pulse inside the electrode material, and a geometry-dependent parameter that distinguishes diffusive behavior in different local environments. The use of a stretched exponential to extract the time constant and hence diffusion coefficient has not been used with the GITT technique. Most importantly, materials with

flat voltage plateaus can use VR-GITT to analyze the diffusion coefficient along the plateau, which we illustrate with a two-phase material in the supporting information. Second, we have combined our VR-GITT electrochemical measurements with reverse Monte Carlo to infer the lithium distribution in the carbons as a function of composition. To our knowledge the use of Monte Carlo methods, combined with a variation of the GITT technique is new.

As a demonstration of the utility of the methods we have described, we show VR-GITT applied to the well-studied nanoparticle anatase TiO_2 and demonstrate how it is able to give the diffusion constant as a function of Li concentration. We determine the diffusion constant as the Li_xTiO_2 undergoes a phase transition. The results we obtain provide a powerful confirmation of the theoretical and other experimental work on anatase TiO_2, in particular indicating very easily the transition from beta-TiO_2 to the lithium titanate 1:1 phase.[40-46] The use of the stretched exponential in fitting the voltage relaxation curves also gives very accurate open cell voltages as the asymptotic plateau of the exponential. This can be clearly seen in the extracted plateau voltages for TiO_2 in the samples.

Below we present the diffusion dynamics of different types of carbons with different pore structures using GITT and VR-GITT. This allows us to understand the variations of diffusion coefficients in highly ordered mesoporous carbons by comparing the differences and similarities with each other. Our GITT diffusion results validate the new VR-GITT diffusion method.

The first part of the paper describes the VR-GITT technique in detail and is used to characterize the hard carbons we have synthesized. Diffusion coefficients are presented as a function of Li-concentration. The latter part of the paper describes the density profiles of lithium in the hard carbons as a function of Li-concentration determined using a reverse Monte Carlo technique.

2. EXPERIMENTAL METHODS

Four types of carbons were prepared according to the following synthesis procedures. Out of these four, two carbon types with 2D hexagonal structure (NPC-1, NPC-2) were prepared using soft template technique. NPC-1 was synthesized according to the referenced literature.[34] In this preparation phenolic resins were used as the carbon precursor and triblock copolymer as soft template in the organic-organic self-assembly process. NPC-2 was prepared by the inorganic-organic-surfactant self-assembly method according to the literature.[35] In this process tetraethyl orthosilicate (TEOS) was used to obtain higher surface areas and pore volumes. The third carbon type was composed of solid carbon rods (CMK3) which was prepared using the hard template method. CMK3 was prepared using sucrose as carbon source and SBA-15 as the hard template material.[36] Finally, for comparison, to get a lower pore volume, the fourth type of carbon (GNPC) was prepared similar to NPC-1 synthesis process but, without triblock copolymer material.

Brunauer-Emmett-Teller (BET) method was used to calculate the surface area and Barrett- Joyner-Halenda (BJH) method was used to calculate the total pore volume. Pore size distributions from the adsorption branch were analyzed from both NLDFT models

and BHJ method. Total pore volume was calculated by the amount adsorbed at a relative pressure of 0.99. These experiments were carried out using nitrogen adsorption isotherms at 77 K by Coulter SA3100 analyzer for the synthesized samples followed by outgassing process at 300 °C for at least 1 hour. NPC-1, NPC-2 and CMK3 were analyzed by the 2D-nonlocal density functional theory (2D-NLDFT) Cylinder Heterogeneous Surface model using the SAIEUS program[47] since these samples contain cylindrical nanopore channels in the P6m symmetry. The 2D heterogeneous surface model was used for the GNPC type. Next, particle sizes of these samples were analyzed by ImageJ[48] software using Scanning Electron Microscopy (SEM) images. Finally, powder X-ray diffraction (XRD) measurements were performed with Cu Kα radiation source on a Rigaku Ultima IV multipurpose X-ray diffraction system.

Coin cell preparation: In this study two-electrode coin cells were used for the electrochemical analyses. All carbon materials and polyvinylidene fluoride (PVDF) (301F) were baked using custom built Sievert type apparatus at 300 °C and at 110 °C respectively overnight. The purpose was to remove moisture from the electrode materials. The whole assembly process was done inside an argon filled glove box with oxygen content below 1 ppm. Four different slurries were made using synthesized carbon samples as active material, PVDF as binder and N-methyl-2-pyrrolidone (NMP) as solvent. The ratio between active material and binder was 9:1. No carbon black was added in the process. Electrodes were prepared by coating thin layer of the slurry on a battery grade Cu foil. These electrodes were baked at 70 °C for 10 minutes and then at 120 °C for overnight inside the glove box. Coin cells were assembled with metallic lithium chip as reference/counter electrode and a carbon electrode as the working

electrode. 1 M $LiPF_6$ in a mixture of 1:1 ethylene carbonate (EC) and diethylene carbonate (DEC) was used as the electrolyte. Two layers of Celgard brand separators were sandwiched between Li metallic chip and working carbon electrode which was eventually sealed under pressure of 50 kg/cm^2 using hydraulic crimping machine (MTI; MSK 110). All cells were rested for two hours to saturate before taking any measurements.

Electrochemical measurements: First, cells were cycled for 7 cycles between 0.00 V and 3.00 V vs Li/Li^+ with constant current density of 30 mA/g using Maccor 4300 model to avoid effects of solid electrolyte interphase formation (SEI) for the diffusion measurements. Then all the cells were rested for one day and subsequently subjected to galvanostatic intermittent titration technique (GITT). This method is composed of constant current pluses followed by a relaxation period. In the experiment, 15 minutes current pulses with an approximately C/2 current and 4 hours of relaxation were used. The C value was calculated based on the cycling measurement results for each battery. More details can be found in the supporting information. The GITT process was continued until the carbon electrode reached a voltage of zero with respect to Li/Li^+. Before the de-insertion current pulses began, the sample was allowed to soak at zero volts for 10 hours to ensure full insertion. De-insertion continued with current pulses of C/2 for 15 minutes and 4 hour relaxation period. All the voltage vs time measurements were recorded at room temperature using a Maccor model 4300 instrument.

Data fitting: Powder x-ray diffraction data were fitted using fityk[49] software in order to obtain Bragg peak widths from the experimental results. All the recovery voltage

curves were fitted using xmgrace software[50] to extract the VR-GITT parameters, α and τ, as discussed below.

3. RESULTS AND DISCUSSION

Structural Characterization of the Carbons: According to the BET results in Figure 1a, all of the carbon types except GNPC exhibit a type IV isotherm based on the IUPAC classification.[51] This indicates the presence of mesoporosity and microporosity in the samples resulting in large pore volume and surface area. GNPC has a type I isotherm, exhibiting very low surface area and a micro-porous nature in contrast to the other samples. GNPC was made with phenolic resins without polymer (F127), it therefore has no ordered morphology at the nanoscale, yet retains a disordered carbon structure.[52] Figure 1b shows the pore size distribution of the samples from NLDFT models. NLDFT method provides a better understanding about the lower pore size regions (< 2 nm) compared to the BJH method.[53] Nonetheless, poor fitting in the micropore region caused higher standard deviations (Table S1) for CMK3 and NPC-1 compared to NPC-2. We use 2D Cylindrical model for CMK3 even though it has more slit like pores as evident from the reported H3 type hysteresis loop.[36] This is probably the reason we obtain higher standard deviations for CMK3 carbon. Pore size distributions from the BJH method are also included in supplementary documents for comparison (Figure S2). All of the carbon types except GNPC contain micropores and mesopores according to the pore size distributions. Summary of N_2 Physisorption results are given in the Table 2. The SEM images (Figure S3) show the particle size variation between different carbon samples. The particle size of the GNPC was assumed to be similar to NPC-1 since these samples

were sieved through the same 74 µm size sieve. The largest particle size for the carbons CMK3, NPC-1, NPC-2, and GNPC are show in Table 1.

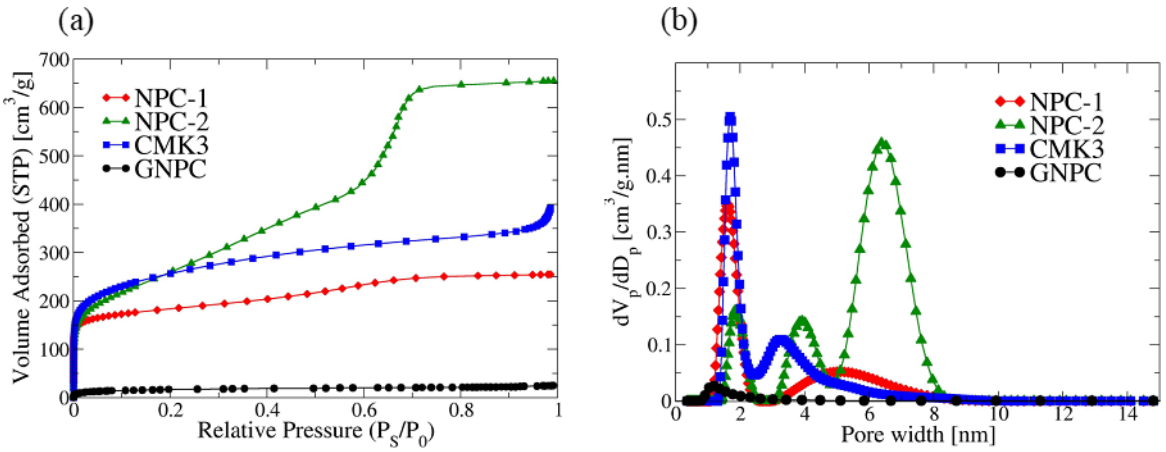

Figure 1. (a) Nitrogen adsorption isotherms for synthesized carbon samples at 77 K, and (b) Pore size distributions calculated from the adsorption branch. The highest surface area and pore volume are for NPC-2.

Figure 2 shows wide-angle XRD patterns for all the carbon samples. These XRD patterns have been used in Scherrer equations to calculate the (002) interlayer spacing and coherence length which are shown in Table 1. The broad peaks corresponding to graphitic (002) and (100) at around 26° and 43° two theta, respectively, indicates no significant long-range order; the carbon network itself is glassy, with very small graphitic nanodomains. However, the GNPC structure shows higher intensity and somewhat narrow peaks with slightly lower d spacing and higher coherence lengths compared to the other carbon samples. This suggests that the GNPC structure may be slightly more graphitic on the nanoscale, compared to the other ordered carbons.

Table 1. Characterization of carbon samples from Nitrogen Physisorption and X-ray measurements.

Sample	Surface Area[a] [m^2/g]	Total Pore Volume[d] [cm^3/g]	d Spacing[c] [nm]	Coherence Length[d] [nm]	Largest Particle Size[e] [μm]
NPC-1	644	0.39	0.39	0.83 ± 0.01	121.13
NPC-2	937	1.01	0.39	0.78 ± 0.01	144.0
CMK3	905	0.60	0.38	0.78 ± 0.01	103.59
GNPC	60	0.04	0.39	0.88 ± 0.01	121.13
Graphite	-	-	0.336	45.3 ± 0.2	-

[a]Calculated by the BET method. [b]Estimated by the amount adsorbed at a relative pressure of 0.99. [c,d]Calculated from the (002) Bragg peak and the Scherrer equation.

Voltage-relaxation GITT Measurements: In addition to analyzing the voltage response during the current pulse, it is useful to examine the relaxation of the open cell voltage (OCV) following current pulses. The depolarization technique, developed for planar interfaces,[54,55] can be used to analyze the OCV relaxation curve in order to get diffusion coefficients in thick electrode pellets. In the depolarization method, the diffusion coefficient is calculated from the gradient obtained from a plot of the logarithm of [OCV(t) - OCV(t=∞)] vs time. In contrast we employ a stretched exponential to analyze the relaxation curves and refer to our approach as voltage relaxation (VR-GITT), and we calculate diffusion constants assuming a spherical particle geometry. It is

important to note that during the diffusive relaxation process the dominant contribution comes from the largest particles in the material. SEM indicates these sizes are in the micron range.

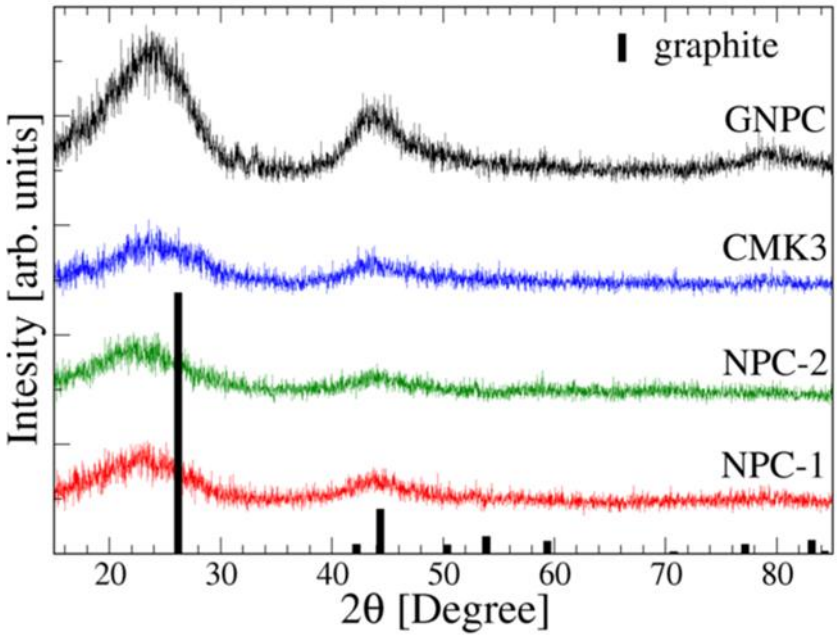

Figure 2. Powder XRD experimental results for carbon samples. Broad intensity around 26° and 43° suggest the amorphous nature of the carbon.

It is known that the stretched exponential is more appropriate to model relaxation and decay processes than the standard exponential function.[56–58] Prominent examples include polymer dynamics, and diffusive processes such as rehydration. The above mentioned different systems can be explained with stretched exponential function, $\exp\left[-(t-t_0/\tau)^{\alpha}\right]$, having either fixed or variable alpha (α) between zero and one and tau (τ) larger than zero depending on the system.[56] In diffusive processes the α parameter is shape-related and is important behavior to understand in our material where the pores

and channels are ordered. Marabi et al. has shown that the stretched exponential shape factor α can have distinct values depending on the geometry and the mechanism of water uptake such as 0.67, 0.72 0.81 for spheres, cylinders and slabs respectively when considering rehydration.[59]

A simple stretched exponential for a typical voltage relaxation in our electrochemical data is captured by the expression in Eq. (1)

$$V = V_{max}\left[1 - \left(\frac{V_{max} - V_{min}}{V_{max}}\right)\exp\left(-\left(\frac{t - t_0}{\tau}\right)^{\alpha}\right)\right] \quad (1)$$

where, V_{max} is the relaxed open cell voltage obtained from the fitting, V_{min} is the minimum voltage of the recovery curve, $(t\text{-}t_0)$ is the relaxation time (difference between initial and final relaxation time), τ is the time constant, and α is the shape-related factor. Fitting of the stretched exponential to a typical VR curve is shown in Figure S4. The diffusion constants following every current pulse were calculated using

$$D = \frac{L^2}{\tau} \quad (2)$$

where L is the radius of the largest particle. To validate the diffusion constants calculated from our extracted time constants, diffusion coefficients were also calculated based on the standard GITT equation which is based on a one-dimensional diffusion process[60]:

$$D = \frac{4r^2}{\pi t}\left(\frac{\Delta E_S}{\Delta E_t}\right)^2 \quad (3)$$

here r is the radius of the particle, t is the duration of the current pulse, ΔE_s is the change in equilibrium voltage during the current pulse, ΔE_t is the total transient voltage change after the IR drop. This equation holds when $t \ll (r^2/D)$ .The voltages of the experimental GITT curves are shown in Figure S5. The VR-GITT data show that NPC-1

has the lowest recovery voltage and fastest relaxation process. This suggests that NPC-1 may not have as deep trap sites discussed in Mochida et al. as compared to CMK3 and NPC-2.[12] A possible explanation may be the following. When some portion of Li ions intercalate into deep trap sites on the first insertion they will have diffusion barrier activation energies larger than the other intercalated Li ions during the voltage recovery. Therefore, the recovery voltages may provide some information about the trap sites. Li resident in a deep trap site will increase the diffusion rate for diffusing Li that cannot enter the site. A competing mechanism, however involves the blocking of a diffusive path by the resident Li. These competing effects may be difficult to determine from the VR-GITT data.

We note one drawback of the standard GITT technique is the ΔE_s term in the numerator of equation (3) which represents the change in equilibrium voltage of the material upon, e.g. insertion of Li. In a two-phase region where the equilibrium voltage does not change ΔE_s would be zero, the diffusion constant may not be calculated in this manner. See for example Zhu and Wang.[61] However, if one uses the voltage relaxation curve and extracts the time constant, a calculation of the diffusion constant is possible with knowledge of the relevant length scale for the diffusion. As it is sometimes difficult to measure diffusion constants, especially over a large concentration region, the VR-GITT technique provides one more characterization tool. For these purposes, and also to provide a more well-studied standard for our analysis that follows, we show the VR-GITT technique applied to nanoparticle anatase TiO_2. This material has been investigated for lithium-ion anodes and its nanoparticle phase diagram is understood as a function of Li concentration.[40–46] We present diffusion measurement results across the entire two-

phase region of anatase TiO_2 + beta Li titanate during Li insertion and de-insertion. The VR-GITT results for anatase TiO_2 demonstrate the ease of use and power of the method. In the Li-Ti-O system there are three phases of relevance for lithium-ion battery applications: (1) alpha-phase anatase with stoichiometry $Li_\delta TiO_2$, (2) beta lithium titanate, $Li_{0.5}Ti_1O_2$, and (3) gamma phase $Li_1Ti_1O_2$. These phases and the nanoparticle phase diagram have been investigated previously.[40-46] (The preparation of our nanoparticle anatase TiO_2 is described in the supplementary.)

The VR-GITT results for 35 nm anatase TiO_2 is shown in Figure 3. Figure 3a shows the fitted final voltages from the stretched exponential yielding the plateau voltage. First, it is clear that there is a plateau region for the 35 nm particles. Insertion of lithium into anatase TiO_2 proceeds via a two-phase region corresponding to the transformation of alpha-TiO_2 to the beta lithium titanate phase. The length of the plateau becomes shorter with smaller particle size (See the supplementary Figure S6 for 11 nm particle size), in agreement with the reported nanoparticle phase diagram in the literature.[40] The drop in potential near full insertion corresponds to the formation of the gamma phase with 1:1 ratio of Li:Ti. The ionic conductivity in this phase is lower, and there is a corresponding change in the extracted VR-GITT parameters.

The extracted tau parameters and corresponding diffusion coefficients are shown in Figure 3b, and 3d. Most interestingly, small changes in the extracted tau parameter indicate a diffusion coefficient that increases as the concentration of lithium increases during the phase transition from alpha to beta. The reason that the diffusion coefficient of Li^+ increases is the following.[42] Density functional theory calculations show that at low lithium concentration in anatase TiO_2 there is strong localization of the electron e^- from

the intercalated Li to a 3d state of the closest Ti center, forming a bound polaronic state of the Li^+ to the Ti center. This binding is roughly 56 meV. As the lithium concentration increases in the anatase TiO_2 and these gap states begin to fill and form a delocalized band, the binding of Li^+ to these states falls, manifesting as a higher diffusion rate of Li^+. VR-GITT measurements of lithium intercalation into anatase TiO_2 illustrate the above explanation in detail. Further, Figure 3c shows the extracted shape parameters from the VR-GITT fits and indicate that the diffusion proceeds largely with the same character (spherical) except at the point where the formation of the gamma Li_1Ti_1 phase appears. There the alpha parameter increases noticeably.

Lithium diffusion in hard carbon: Figure 4 contains the extracted time constants and α parameters vs Li concentration using equation (1) for different carbon samples. Voltages that relax sharply at the beginning of the relaxation are given by smaller values of α. The extracted α values generally lie between 0.2 - 0.5. As evident in Figure 4a the α shape parameter clearly distinguishes carbons synthesized with and without silicate in the preparation process. The shape parameter data fall into two distinct groups. A strong variation of α for carbons NPC-1 and GNPC without silicate and a non-varying α for carbons NPC-2 and CMK3 prepared with silicate. The time constants are generally increasing and shown in Figure 4b, with the exception of the one non-porous carbon GNPC, which shows a rapid drop in τ. The low capacity in these measurements is due to large current density used during the VR-GITT pulse.

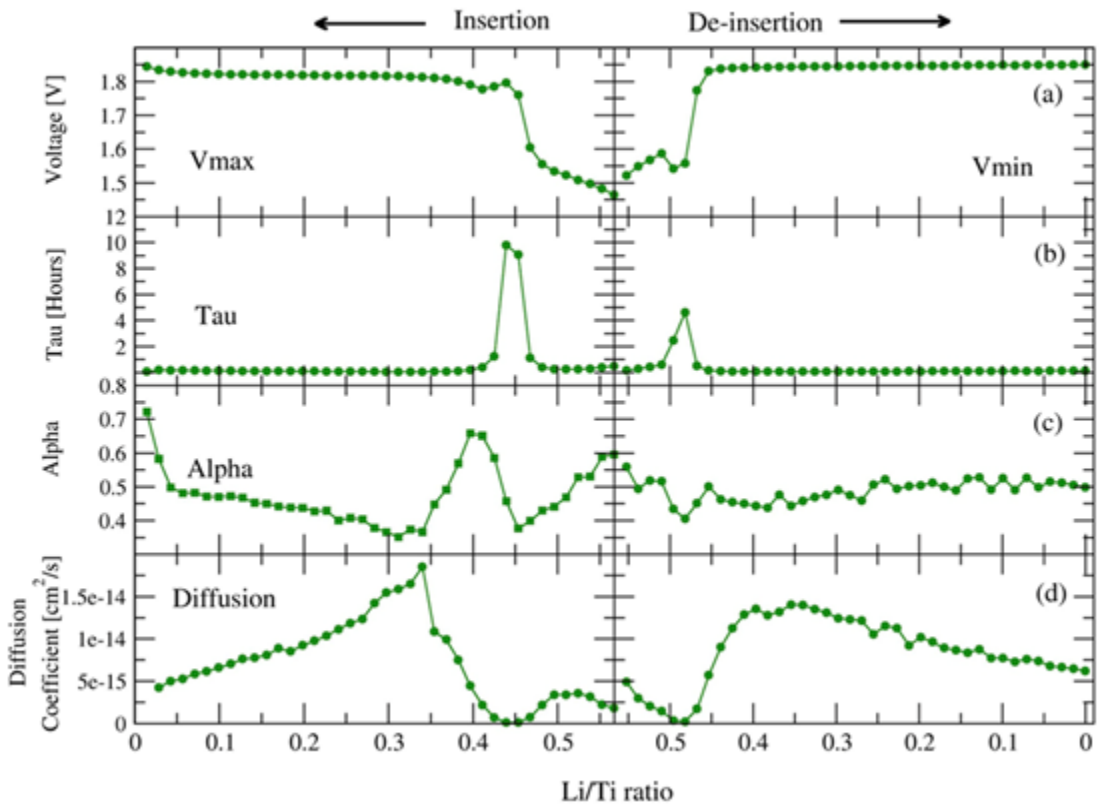

Figure 3. (a) VR-GITT fitted voltages, (b) Extracted time constants (τ), (c) Stretched exponential shape parameters (α), and (d) Diffusion coefficients form VR-GITT method for 35 nm nanoparticle anatase TiO_2.

Figure 5 shows the diffusion coefficients for carbon samples from both the VR-GITT time constant (equation 2) and the standard GITT (equation 3). These results show very good agreement with each other. All the obtained diffusion coefficients from VR-GITT and GITT are in the range of 10^{-7} and 10^{-9} cm^2s. This shows an agreement with the range of reported diffusion coefficients for carbonaceous materials.[39,62–64] However, due to the lack of the Li diffusion measurements for the exact materials discussed in this study, we cannot compare the values directly.

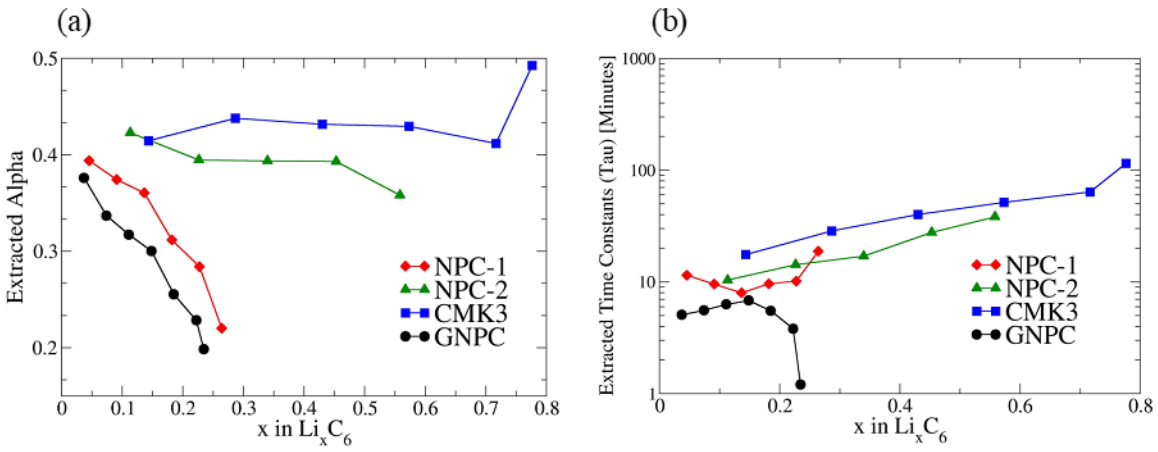

Figure 4. (a) Extracted Alpha (α) values as a function of Li concentrations, and (b) Extracted time constants (τ) as a function of Li concentrations for carbon samples. Tau and Alpha were obtained by VR-GITT analysis method.

GNPC shows the highest diffusion coefficients. This may be due to more graphitic nature of the GNPC sample. Persson et al. have shown that Li diffusion values in highly oriented pyrolytic graphite (HOPG) in the direction parallel to graphene layers is about ~10^{-7}- 10^{-6} cm^2s^{-1} whereas the diffusion along the grain boundaries is about ~10^{-11} cm^2s^{-1} through computational calculations.[65] This suggests if our GNPC has more graphitic nano-domains it should have a higher diffusion coefficient.

Computational Modeling of the Lithium Density Profile: Li plating is a well-known phenomenon which occurs specially under low temperatures, high current pulse and high State of Charge (SOC). There have been several studies reported in literature about the investigation of Li deposition inside electrode material under different conditions. One common finding is that uneven Li plating leads to form dendrites and may even pierces the separator causing internal short circuit of the battery.[66-72] Li plating inside the electrode material without leading to dendritic growth depending on the

morphology of the electrode material is also found to be possible. This phenomenon can lead to very high reversible capacities for the materials. In these cases, formation of metallic Li occurs inside the interior of the pores or in the cavities/defect sites of the material and it will not lead to form destructive dendrites on the electrode surface.[73–76]

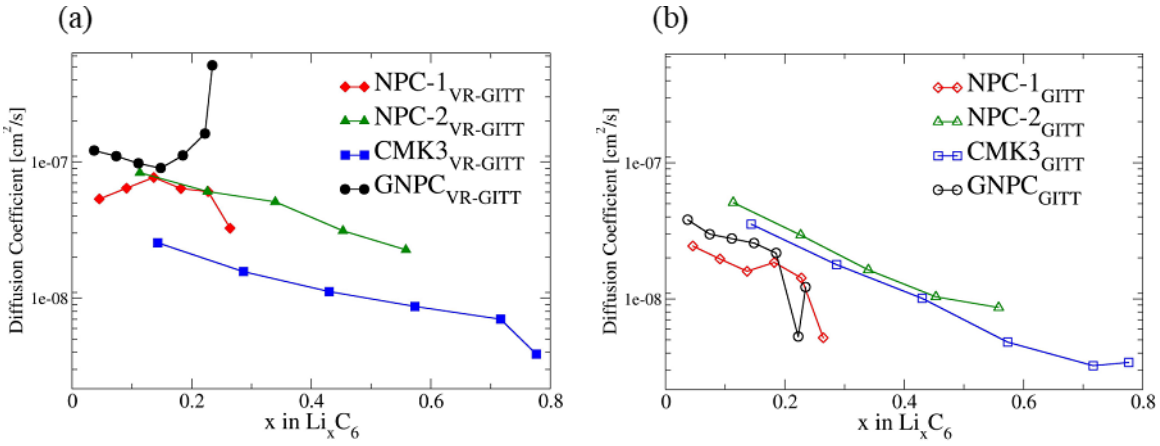

Figure 5. Diffusion results from (a) VR-GITT method (closed symbols), and (b) GITT method (open symbols). The maximum difference between two methods with in order of one magnitude for all the other materials except for GNPC.

The lithium capacities in excess of LiC_6 in the cycling data strongly suggest that lithium must be plating inside the pores of the carbon. Interestingly, NPC-2 type carbon with very high specific area and pore volume can give reversible capacities above 1000 mAh/g which is more than two times of the standard graphite capacity (Figure S7). One hypothesis is that the lithium plates during the relatively high current pulse on insertion in the GITT measurement, and then diffuses through the carbon slowly. If this is the case, we expect a non-uniform distribution of lithium in the carbon particles during insertion. After full insertion and during the de-insertion VR-GITT measurements, we expect that this non-uniformity will be smaller.

In order to investigate the distribution profile of lithium in the carbon particles we employed computational modeling of the diffusion process during the voltage relaxation on each insertion and de-insertion. We extracted density profiles numerically by integrating the diffusion equation and using Monte Carlo methods to determine the lithium density profile following every VR-GITT current pulse. The details are as follows.

The outer edge of the particle that is in contact with the electrolyte is the surface that provides the measured voltage response. Our objective was to use this voltage response to calculate the concentration profile of lithium in the particles immediately following the current pulse in the VR-GITT experiments. We deduced the initial lithium profile by assuming lithium was incorporated into the (mostly surface region) of the carbon particles during the (short) current pulse, and that this high-concentration diffused into the carbon particles over the relaxation period of the measurement (Figure S8). The resulting voltage response is given by the concentration of the lithium on the outer edge of the particle (Figure S9). In order to make the computations tractable we assumed spherical particles. To obtain the time evolution of the lithium concentration we used a standard Crank-Nicolson integration routine with Dufort-Frankel near $r = 0$. Our computations allowed for a diffusion constant that varied as a function of distance from the center of the particle, $D(r)$. This assumption allows for the difference in diffusion rates along the pore channels and/or through the carbon matrix itself. The simplification that D is only a function of r and not a complicated function of the carbon pore morphology is a reasonable one on based on the length scale ratio of the pore size (10^{-9} m range) to the particle size (10^{-6} m range). The carbon particles are not monolithic ordered

structures, but are comprised of small domains of ordered pores. The size of the domains is much smaller than the micrometer size of the largest carbon particles.

For each voltage response curve, collected during the VR-GITT measurement, we determined the initial lithium density profile in the particle using standard Monte Carlo simulated annealing (MCSA) to fit the experimental voltage response. The cost function was therefore the difference between the experimental voltage relaxation and the computed voltage response, given an initial density profile. An example MCSA computation is shown in Figure S10. For all computations the integrated density was normalized to unity and the resulting density profiles $f(r)$, and diffusion constant profiles $D(r)$ are dimensionless.

Monte Carlo details: We used $N = 20$ spherically concentric shells or bins in a particle for the simulations. In each shell the density and diffusion constant profiles were allowed to vary according to three different configuration changes, (i) scaling of the overall profile, $f \rightarrow (1 +/- \delta)*f$ (ii) increase or decrease of profile, $f \rightarrow (f +/- \delta)$, (iii) increase or decrease profile of single bin, $f_i \rightarrow (f_i +/- \delta)$. An exponential annealing schedule was used with $T(n) = \exp(-n/n_0)$, with $n_0 = 2$, and a total of 10 temperature steps. The number of configuration changes for each temperature was $N_c = 10^3$. The value of δ for each of the configuration changes was chosen so that rejection percentages were in the range of 65 % to 75 %.

The relaxation curve at each VR-GITT data point represents the diffusion of lithium in the particles at either an increasing or decreasing total Li concentration if the measurement was taken as an insertion or de-insertion. The initial lithium density profiles $f(r)$, are plotted as a function of the cycle number and the particle radius in Figure 6.

Peaks appearing along the density profiles *f(r)* vs radius graph denote high Li concentration positions in the particle. In our model we consider outer surface as the surface where electrolyte makes contact with the carbon particle. This includes both the outer edge of the particle and the inner surface of the nanopore channel. High Li concentration points appearing along the radius of the particle should be due to agglomerations/plating of Li inside the nanopore channels. In previous studies Li plating in defects and cavities have been observed for graphene and mesopore carbons.[74,75] Moreover, intercalation of plated Li into graphite during relaxation period have been reported.[77] Uhlmann et al. have reported that the shape of the voltage curve during charging and during relaxation for graphite in the presence of plating. However, we have no two-phase region and we did not observe any voltage plateau in voltage relaxation curves for our amorphous hard carbon materials.[77]

There are no reports in the literature of direct observation of Li plating or intercalation of plated Li for our carbons. However, plating and intercalation occur in graphite and graphene support the possibility of a similar phenomenon happening inside the amorphous carbons used in this paper. According to BET analysis our carbon samples have hexagonal nanopore structures. These pore channels are not perfectly smooth and have cavities and sharp protrusions along the pore channels. So, during high current pulse, it is likely that Li may plate in these areas and diffuse into the particle during the relaxation.

The results of the MCSA computations are revealing. First, we note that the variation of the inferred diffusion coefficients was small (within a factor of 5) across the VR-GITT measurement of a sample and a varying diffusion constant was not necessary

to obtain the density profiles. Second, the density profile becomes flat as the concentration of lithium reaches its maximum value and returns to a more featured landscape upon de-insertion (Figure 6).

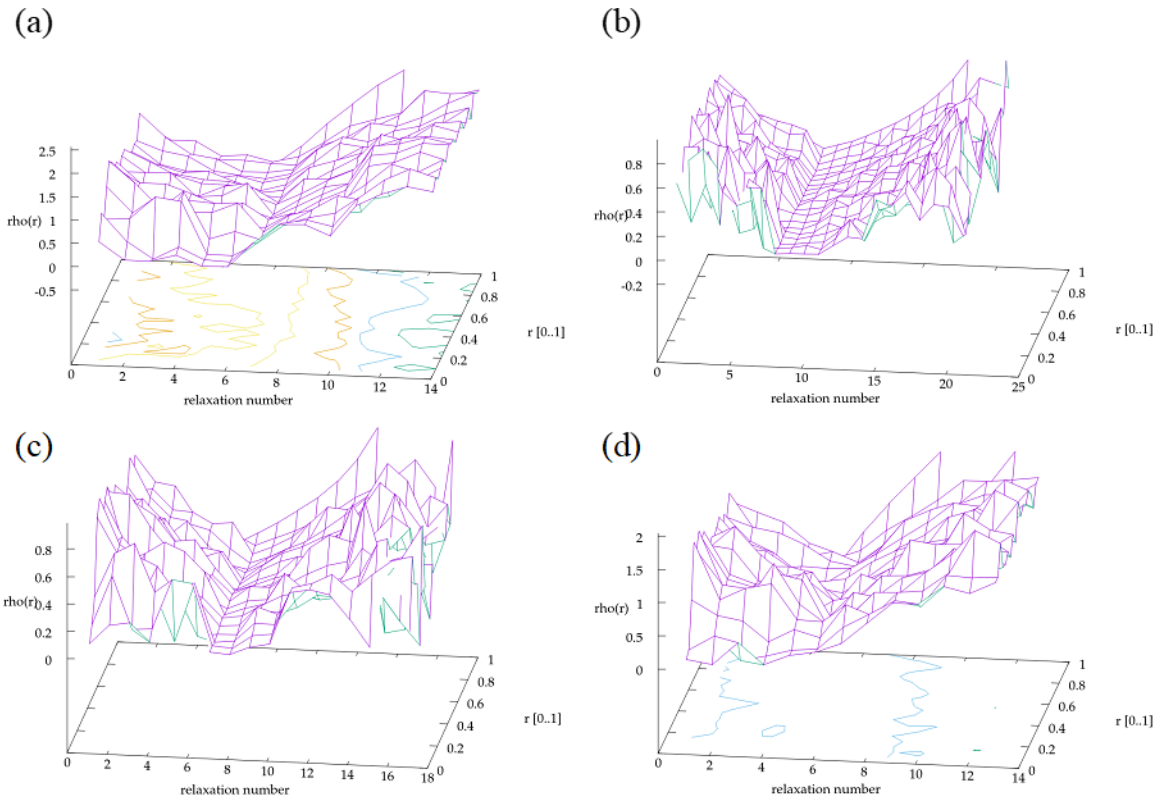

Figure 6. Lithium density profiles computed from the voltage relaxation curves for each carbon sample during both insertion and de-insertion. The valleys appear near full insertion. (a) CMK3, (b) GNPC, (c) NPC-1, and (d) NPC-2.

A flat voltage profile indicates evenly distributed Li inside the pores. The zero voltage soaking step following the VR-GITT insertion pulses evidently increases the Li concentration and smooths its density profile. After the voltage soaking period, the density profiles stay flat until few de-insertion current pulses for GNPC and NPC-1. This may suggest that a higher amount of Li plating occurs in these samples compared to

NPC-2 and CMK3. This is in contrast to a well-studied material such as anatase TiO_2 nanoparticles. An example of the VR-GITT applied to this material shows a very flat landscape of lithium concentration profile across insertion and de-insertion and only an increase in the density right at the edge of the particle upon full insertion (Figure S11).

To support our density profile analysis, we quantified the degree of fluctuation in the density plots. The results indicate that the computed lithium profiles of the carbon samples are significantly more non-uniform than the standard provided by the TiO_2 anatase nanoparticles. Figure 7 shows the standard deviation for the calculated density profiles at each step of the VR-GITT process, i.e., the fluctuations in the profile from $r=0$ to $r=1$, for each relaxation curve that was fitted using MCSA. The similarity between the samples prepared with silicate (CMK3, NPC-2) or without (NPC-1, GNPC) is again very apparent in the de-insertion standard deviations. A direct comparison of the carbon data with the standard TiO_2 is not possible because of the difference in particle size and due to the differences in the experimental procedure. In our TiO_2 experimental procedure, no soaking step was involved between insertion and de-insertion. However, the time scale for relaxation of all of the samples is of the order required by the approximate known diffusion constants for carbon and TiO_2, and so the standard deviation profiles do provide some indication of the initial lithium density profiles inside the particles.

Our results show that the density profiles in the carbons become more uniform (smaller standard deviation) as the Li concentration increases and the most uniform following the zero voltage soaking step. This indicates that the Li is most evenly distributed at full insertion. A calculation of the pore volume of the materials and the Li concentration from the VR-GITT measurements shown in the SI indicate that if plating

occurs in the pores, it fills no more than about 10-20 % of the pore volume. Interestingly for the GNPC-type carbon, which has the lowest pore volume, this number is calculated to be around 100%. This suggests that if plating initiates on the 'sharp' edges of the pore walls during a high current pulse, it may evenly distribute itself over the surface of the pore wall and/or intercalate over time.

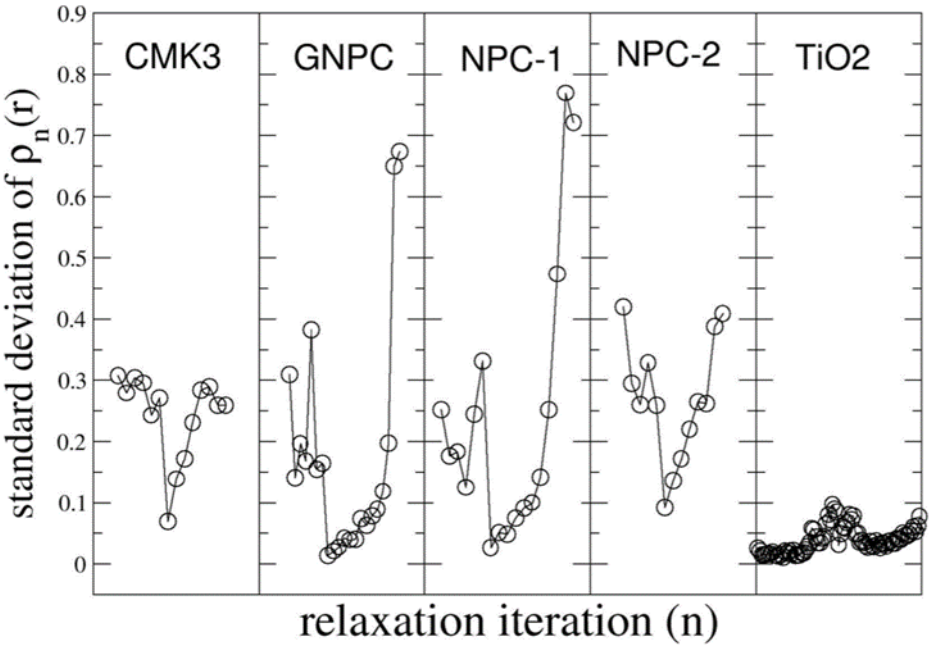

Figure 7. Standard deviations of the voltage profile for each voltage relaxation curve for both insertion (first data points) and de-insertion. The standard deviation is lowest for fully inserted samples of carbon. The TiO_2 standard shows relatively much lower fluctuation of the lithium density in the particles.

4. CONCLUSIONS

The lithium ion diffusion in ordered amorphous hard carbons was investigated using the voltage relaxation data from standard GITT measurements. Our results indicate that both GITT and VR-GITT diffusion constant results are generally in agreement with

each other. All carbon diffusion coefficients investigated in this study were in the range of 10^{-7} and 10^{-9} cm^2s from both methods. Moreover, our results show that the newly developed VR-GITT method is also helpful in distinguishing differences between carbon samples. Particularly, carbon samples made with and without silicate can be clearly identified from the α parameter obtained by VR-GITT. The fact that our method can distinguish between different carbon preparation techniques means it is able to distinguish microstructural features of the carbon. The methods here may be used to characterize new electrochemical materials in addition to carbons. For example, the alpha parameter may be extracted for a variety of anode and cathode candidates over a range of Li concentrations that may be very specific to the preparation method of the material.

In addition to the newly developed VR-GITT method, this paper presents a new approach to investigate the inside of electrode by calculating Li density profiles. Initial Li density profiles derived from the voltage relaxation data provide information about the Li distribution inside the particle just after the current pulse. According to our results, we observed non-uniform Li distributions inside the carbon particles. We believe this non-uniformity is due to Li plating during the high current pulse. We were also able to show that higher amount of Li plating occurs in the non-silica based carbon samples. Our results suggest that mitigating the plating problem in high-current charging environments may be possible with engineered nanoporous electrodes where plating may be directed to occur inside a pore structure with a small free pore volume.Finally, our results show that the VR-GITT technique is a simple method for investigating diffusion in the two-phase region of materials where there is a flat voltage profile that makes the standard GITT unreliable.

ACKNOWLEDGMENTS

The authors thank David Osborn for assistance in the XRD measurements and obtaining SEM images. This work was partially supported by funds from the Research Board Award from the University of Missouri. The authors gratefully acknowledge research support from the Hydrogen Materials Advanced Research Consortium (Hy-MARC), established as part of the Energy Materials Network under the U.S. Department of Energy, Office of Energy Efficiency and Re- newable Energy, Fuel Cell Technologies Office, under Award Number DOE – EE0007656.

SUPPORTING INFORMATION

Current calculation for the diffusion measurements were carried out based on the final capacity value (C) for each battery after seven cycles. Current used for the diffusion was C/2 for each current pulse.

For example:

Final capacity – C mA/g, Mass of the active material – M g

Current used in the GITT method – (C/2) mA/g * (M) g

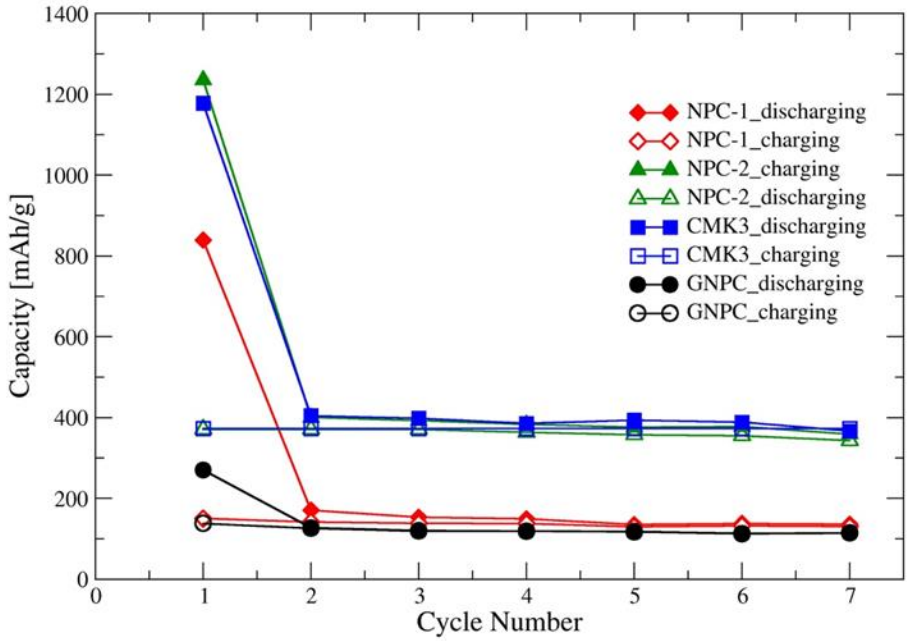

Figure S1. Capacity vs Cycle numbers for the first 7 cycles. NPC-1 and CMK3 show higher capacity compared to NPC-1 and GNPC.

Table S1. Standard deviations of the fits from 2D-NLDFT models.

Sample name	Standard deviation [nm]
NPC-1	2.28
NPC-2	0.79
CMK3	1.31
GNPC	0.05

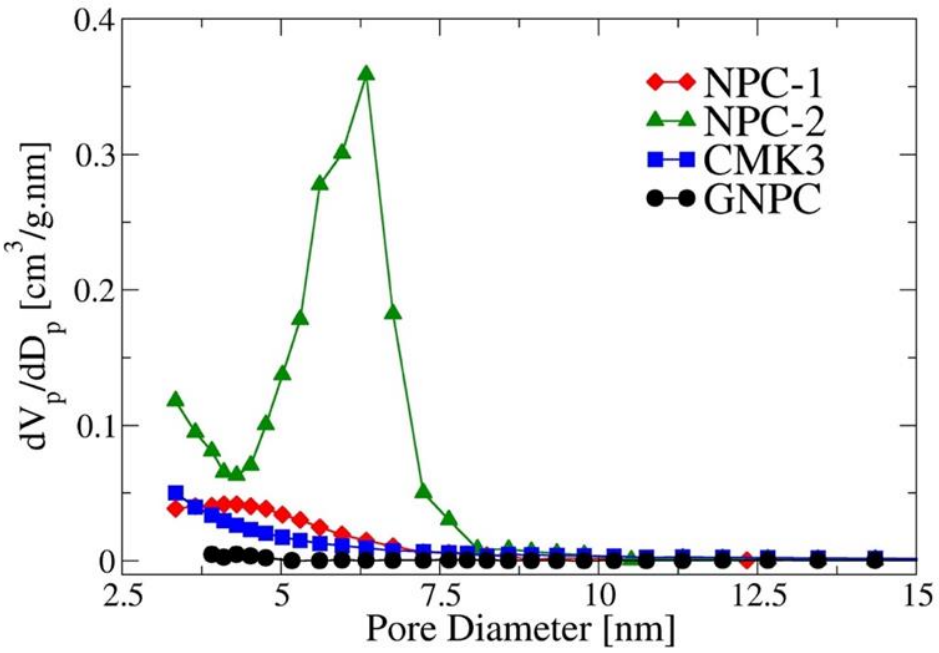

Figure S2. Pore size distributions from BJH method. Minimum pore size that can be obtained from BJH was ~ 3 nm.

a) b) c)

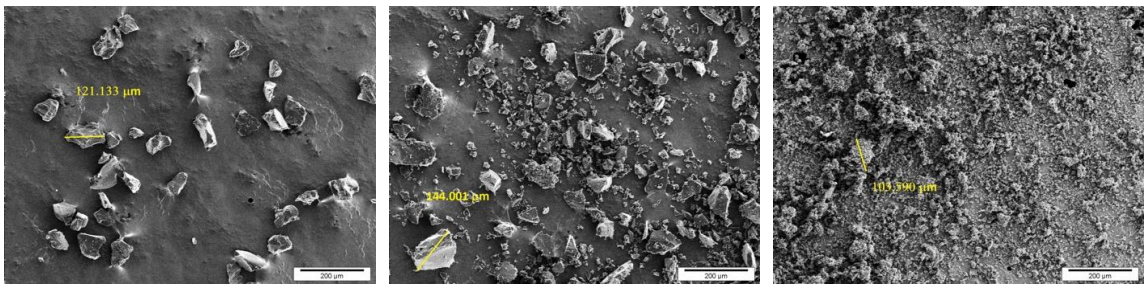

Figure S3. SEM images of carbon samples used for the study. a) NPC-1, b) NPC-2 and c) CMK3.

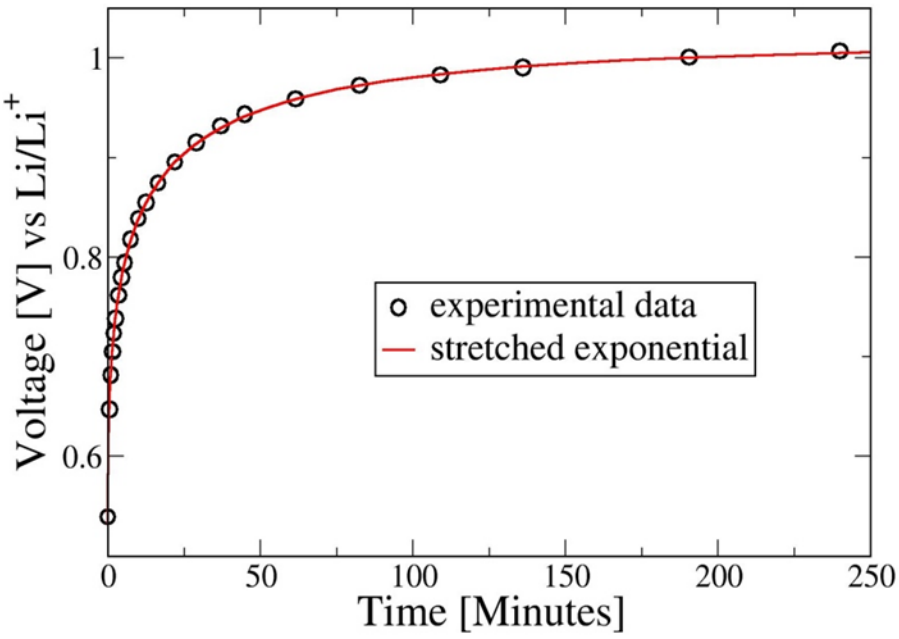

Figure S4. Fit of stretched exponential to a typical voltage relaxation curve in the VR-GITT procedure.

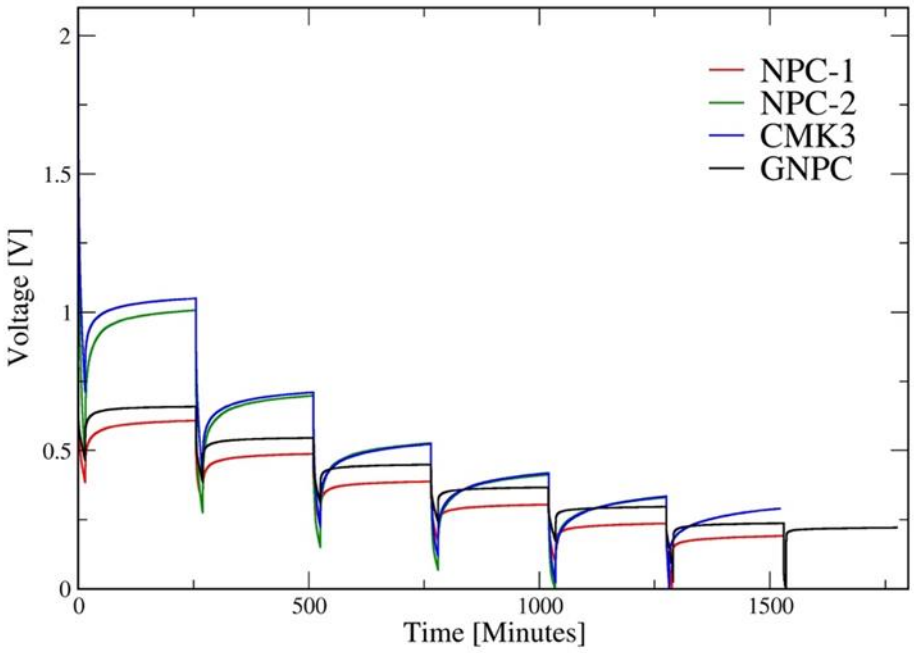

Figure S5. Experimental Li- insertion GITT curves for the carbon samples.

VR-GITT Technique Applied to Nanoparticle Anatase TiO_2.

Hydrolysis synthesis process: In a typical process deionized water and hydrochloric acid solutions were prepared with different concentrations of H+ for the hydrolysis process. In one example, a 200 ml mixture of 50 ml 12 mol/L hydrochloric acid and 150 ml deionized water has an H+ concentration of 3 mol/L (pH = -0.48). The deionized water and hydrochloric acid solution was mixed well with vigorous stirring for 5 minutes with a stir bar. The precursor solution was a mixture of 15 ml ethanol (Decon: ethanol 200 proof) and 5 ml titanium (IV) isopropoxide (Sigma-Aldrich: ≥ 97.0 %). The precursor mixture solution was slowly poured into the deionized water and hydrochloric acid solution followed by vigorous stirring at room temperature for 2 hours. Then the transparent liquid mixture was poured into petri dishes and the mixture was evaporated at

room temperature in air for 6 days. The white-yellow precipitates were washed with ethanol 3 times and then dried in air for 2 hours until the ethanol was evaporated. The precipitates were then dried in a vacuum oven at 100 °C for 4 hours and ground into fine powders using an agate mortar and pestle. Finally, the as-prepared powders were annealed in a tubular furnace (Lindberg tube furnace Model-54233) in air under elevated temperatures from 150 °C to 750 °C for 2 hours to obtain the desired particle sizes. Two particle sizes, 11 nm and 35 nm, were prepared for GITT measurements. In the experiment, 0.25 hours current pulses with C/10 current and 2.5 hours of relaxation were used.

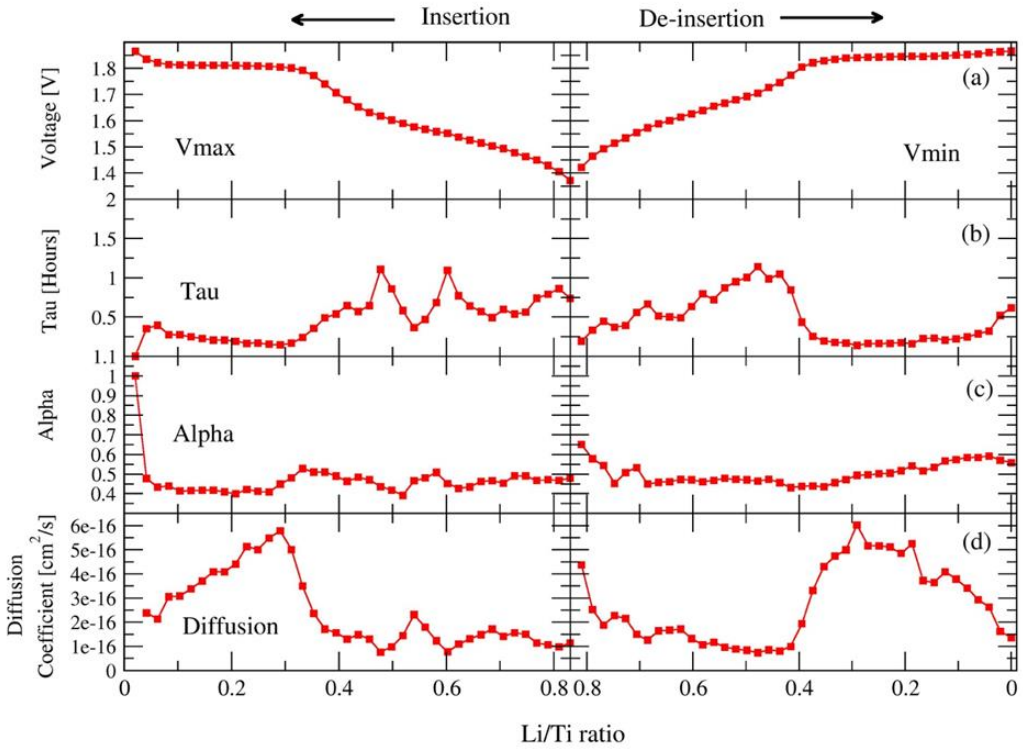

Figure S6. VR-GITT fitted voltages (a), Extracted Tau (time constant) values (b), Stretched exponential shape parameters (c) and Diffusion coefficients form VR-GITT method (d) for 11 nm nanoparticle anatase TiO_2.

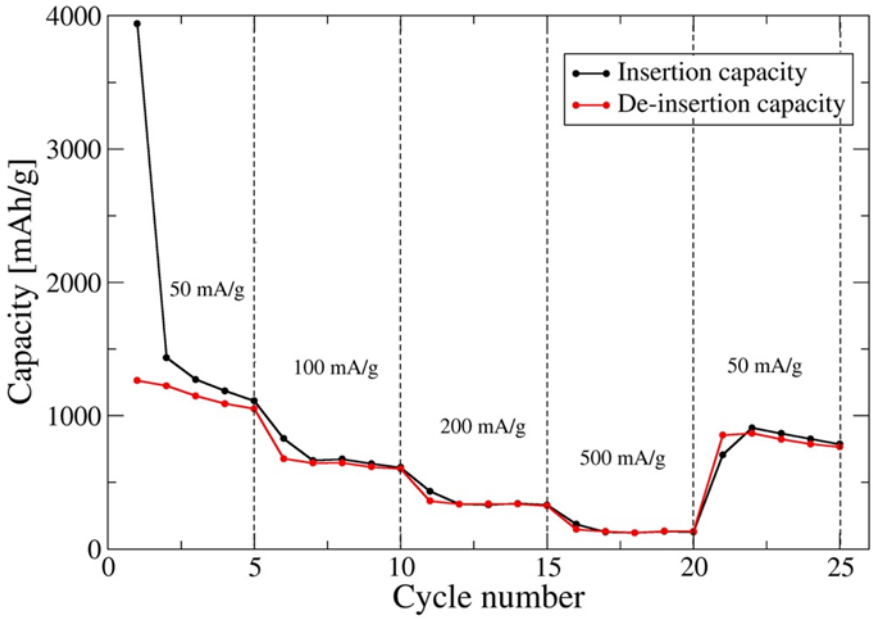

Figure S7. Capacity vs cycle number results for NPC-2 type carbon exhibiting high capacities. (Sample information; surface area = 1939.94 m^2/g, pore volume = 2.48 cc/g)

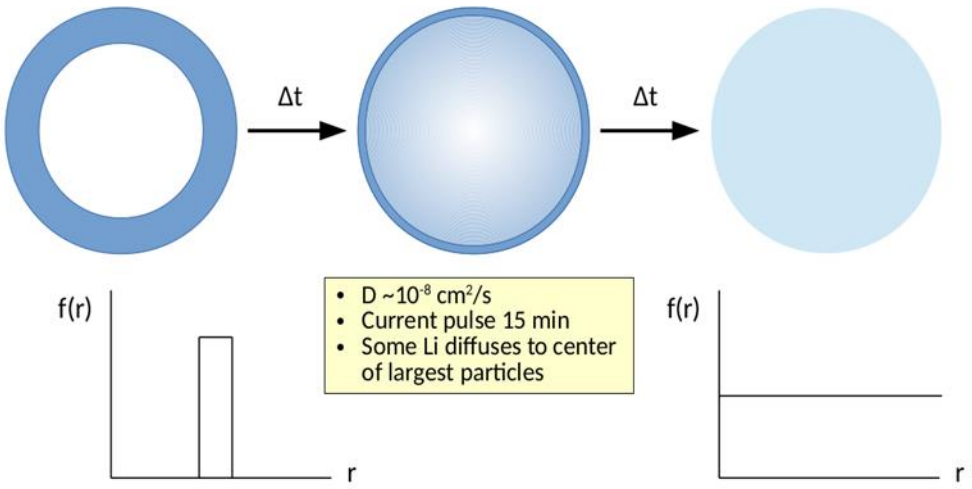

Figure S8. Idealized VR-GITT process and the resulting density, f(r), of lithium in the electrode. The current pulse leaves a shell of Li on the outer region of the particle (left figure) that diffuses into the particle over time, resulting in a uniform distribution (right).

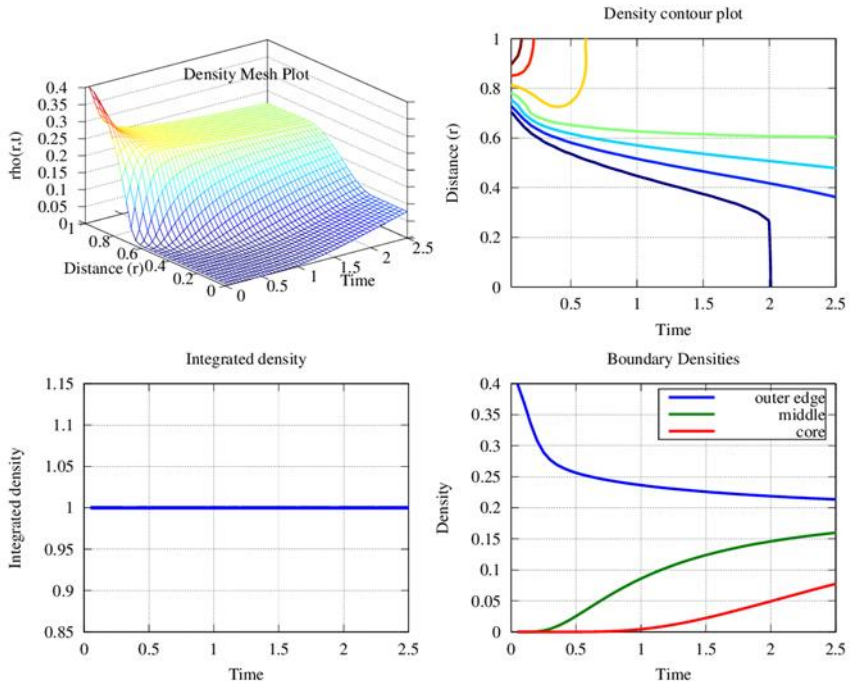

Figure S9. Computed lithium concentration inside a spherical particle as a function of time using a Crank-Nickolson integration scheme. The initial condition is a shell of lithium on the outer edge that diffuses into the center of the particle (top left). The density on the outer edge as a function of time (lower right) is proportional to the measured potential.

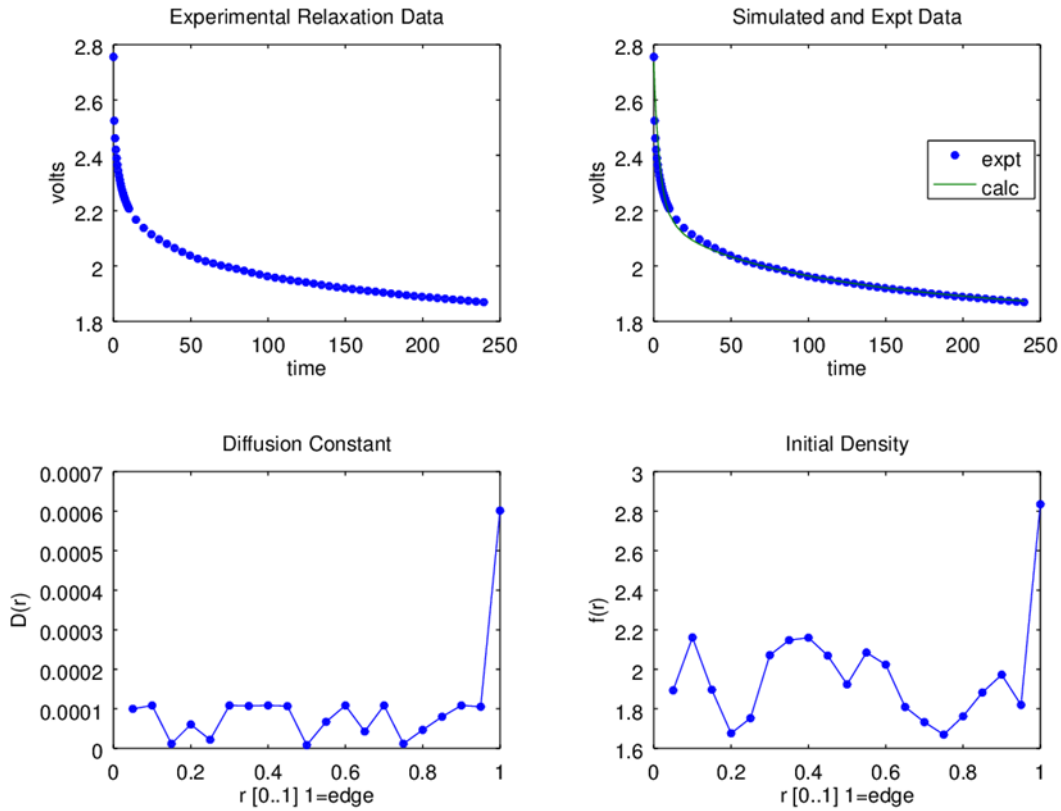

Figure S10. Representative density profile (lower right) and diffusion constant (lower left) determined from a Monte Carlo optimization of the initial profile as a function of radius from the center of a particle. The resulting Monte Carlo fit to the data is shown in the top right graph.

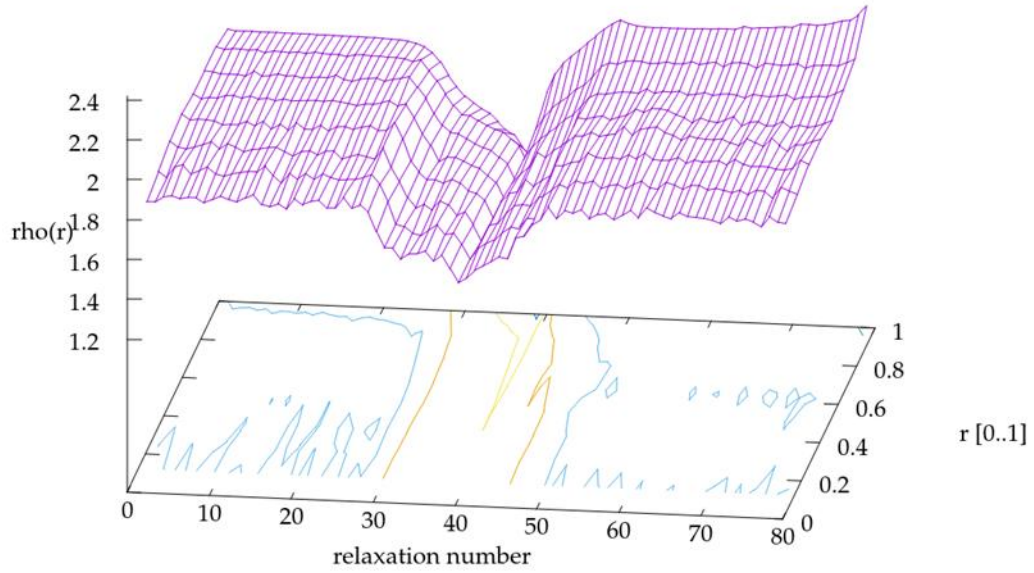

Figure S11. Computed lithium density profile of nanoparticle anatase TiO_2. Note the flatness of profile across both insertion and de-insertion.

Li volume and Carbon volume were calculated as follows:

Li volume= Total amount of Li moles*Molar mass of Li/ (density of the Li)

Carbon volume= BET pore volume*mass of the electrode material.

Table S2. Amount of filled Li inside the carbon at the end of the GITT insertion current pulses.

Sample	(Li volume/Carbon volume) *100
GNPC	110
NPC-1	12
NPC-2	10
CMK3	23

REFERENCES

1. S. Goriparti, E. Miele, F. De Angelis, E. Di Fabrizio, R. Proietti Zaccaria, and C. Capiglia, *J. Power Sources*, **257**, 421 (2014).

2. J. Ni, Y. Huang, and L. Gao, *J. Power Sources*, **223**, 306 (2013).

3. F. Yao, D. T. Pham, and Y. H. Lee, *ChemSusChem*, **8**, 2284 (2015).

4. S. Gautier, F. Leroux, E. Frackowiak, A. M. Faugere, J.-N. Rouzaud, and F. Beguin, *J. Phys. Chem. A*, **105**, 5794 (2001).

5. M. Winter, J. O. Besenhard, M. E. Spahr, and P. Novak, *Adv. Mater.*, **10**, 725 (1998).

6. E. Buiel and J. R. Dahn, *J. Electrochem. Soc.*, **145**, 1977 (1998).

7. E. Buiel and J. R. Dahn, *Electrochimica Acta*, **45**, 121 (1999).

8. K. Guerin, A. Fevrier-Bouvier, S. Flandrois, B. Simon, and P. Biensan, *Electrochimica Acta*, **45**, 1607 (2000).

9. P. J. F. Harris, *Philos. Mag.*, **84**, 3159 (2004).

10. B. Scrosati, *Electrochimica Acta*, **45**, 2461 (2000).

11. E. Buiel, A. E. George, and J. R. Dahn, *J. Electrochem. Soc.*, **145**, 2252 (1998).

12. I. Mochida, C.-H. Ku, and Y. Korai, *Carbon*, **39**, 399 (2001).

13. J. R. Dahn, T. Zheng, Y. Liu, and J. S. Xue, *Science*, **270**, 590 (1995).

14. D. A. Stevens and J. R. Dahn, *J. Electrochem. Soc.*, **148**, A803 (2001).

15. B. Guo et al., *Electrochem. Commun.*, **10**, 1876 (2008).

16. J. Read, D. Foster, J. Wolfenstine, and W. Behl, *J. Power Sources*, **96**, 277 (2001).

17. H. Q. Li, R.-L. Liu, D.-Y. Zhao, and Y.-Y. Xia, *Carbon*, **45**, 2628 (2007).

18. D. Saikia, T.-H. Wang, C.-J. Chou, J. Fang, L.-D. Tsai, and H.-M. Kao, *Rsc Adv.*, **5**, 42922 (2015).

19. Y. Song, L. Li, Y. Wang, C. Wang, Z. Guo, and Y. Xia, *ChemPhysChem*, **15**, 2084 (2014).

20. Y. Zhai, Y.Dou, D.Zhao, P. F. Fulvio, R. T. Mayes and S.Dai, *Adv. Mater.*, **23**, 4828 (2011).

21. X. Liu, D. Peaslee, C. Z. Jost, and E. H. Majzoub, *J. Phys. Chem. C*, **114**, 14036 (2010).

22. C. L. Carr and E. H. Majzoub, *J. Phys. Chem. C*, **120**, 11426 (2016).

23. C. L. Carr, W. Jayawardana, H. Zou, J. L. White, F. E. Gabaly, M. S. Conradi, V. Stavila, M. D. Allendorf, and E. H. Majzoub, *Chem. Mater.*, **30**, 2930 (2018).

24. X. Liu, D. Peaslee, and E. H. Majzoub, *J. Mater. Chem. A*, **1**, 3926 (2013).

25. A. F. Gross, J. J. Vajo, S. L. Van Atta, and G. L. Olson, *J. Phys. Chem. C*, **112**, 5651 (2008).

26. R. D. Stephens, A. F. Gross, S. L. V. Atta, J. J. Vajo, and F. E. Pinkerton, *Nanotechnology*, **20**, 204018 (2009).

27. L. L. Zhang and X. S. Zhao, *Chem. Soc. Rev.*, **38**, 2520 (2009).

28. S. Komaba, W. Murata, T. Ishikawa, N. Yabuuchi, T. Ozeki, T. Nakayama, A. Ogata, K.Gotoh, and, K. Fujiwara, *Adv. Funct. Mater.*, **21**, 3859 (2011).

29. Y. Meesala, A. Jena, H. Chang, and R.-S. Liu, *ACS Energy Lett.*, **2**, 2734 (2017).

30. 30. J. G. Kim, B. Son, S. Mukherjee, N. Schuppert, A. Bates, O. Kwon, M. J. Choi, H. Y. Chung, and S. Park, *J. Power Sources*, **282**, 299–322 (2015).

31. A. Unemoto, S. Yasaku, G. Nogami, M. Tazawa, M. Taniguchi, M. Matsuo, T. Ikeshoji, and S. Orimo, *Appl. Phys. Lett.*, **105**, 083901 (2014).

32. Y. Liu, B. Li, H. Kitaura, X. Zhang, M. Han, P. He, and H. Zhou, *ACS Appl. Mater. Interfaces*, **7**, 17307–17310 (2015).

33. F. Han, J. Yue, X. Fan, T. Gao, C. Luo, Z. Ma, L. Suo and C. Wang, *Nano Lett.*, **16**, 4521(2016).

34. Y. Meng, D. Gu, F. Zhang, Y. Shi, L. Cheng, D. Feng, Z. Wu, Z. Chen, Y. Wan, and A. Stein, *Chem. Mater.*, **18**, 4447 (2006).

35. R. Liu, Y. Shi, Y. Wan, Y. Meng, F. Zhang, D.Gu, Z.Chen, B.Tu, and D. Zhao, *J. Am. Chem. Soc.*, **128**, 11652 (2006).

36. S. Jun, S. H. Joo, R. Ryoo, M. Kruk, M. Jaroniec, Z. Liu, T. Ohsuna, and O. Terasaki, *J. Am. Chem. Soc.*, **122**, 10712 (2000).

37. C. Liang, Z. Li, and S. Dai, *Angew. Chem. Int. Ed.*, **47**, 3696 (2008).

38. W. Weppner and R. A. Huggins, *J. Electrochem. Soc.*, **124**, 1569 (1977).

39. P. Yu, B. N. Popov, J. A. Ritter, and R. E. White, *J. Electrochem. Soc.*, **146**, 8 (1999).

40. M. Wagemaker, W. J. Borghols, and F. M. Mulder, *J Am Chem Soc*, **129**, 4323 (2007).

41. K. Yang, Y. Dai, B. Huang, and M.-H. Whangbo, *Chem Mater*, **20**, 6528 (2008).

42. B. J. Morgan and G. W. Watson, *Phys Rev B Condens Matter*, **82**, 144119 (2010).

43. U. Lafont, D. Carta, G. Mountjoy, A. V. Chadwick, and E. M. Kelder, *J Phys Chem C*, **114**, 1372 (2010).

44. K. Shen, H. Chen, F. Klaver, F. M. Mulder, and M. Wagemaker, *Chem Mater*, **26**, 1608 (2014).
45. B. J. Morgan and G. W. Watson, *J Phys Chem Lett*, **2**, 1657–1661 (2011).

46. W. J. H. Borghols, D. Lützenkirchen-Hecht, U. Haake, E. R. H. van Eck, F.M. Mulder, and M. Wagemaker, *Phys Chem Chem Phys*, **11**, 5742–5748 (2009).

47. J. Jagiello, *Langmuir*, **10**, 2778 (1994).

48. C. A. Schneider, W. S.Rasband and K. W. Eliceiri, *Nat. Methods*, **9**, 671 (2012)

49. M. Wojdyr, *J. Appl. Crystallogr.*, **43**, 1126 (2010)

50. P. J. Turner, Cent. Coast. Land-Margin Res. Or. Grad. Inst. Sci. Technol. Beaverton OR (2005).

51. 51.K. S. Sing, D. H. Everett, R. A. W. Haul, L. Moscou, R. Pierotti, J. Rouquerol, and T. Siemieniewska, *Pure Appl. Chem.*, **57**, 603 (1985).

52. W. E. Van der Linden and J. W. Dieker, *Anal. Chim. Acta*, **119**, 1 (1980).

53. J. Landers, G. Y. Gor, and A. V. Neimark, *Colloids Surf. Physicochem. Eng. Asp.*, **437**, 3 (2013).

54. R. Amin, D. B. Ravnsbæk, and Y.-M. Chiang, *J. Electrochem. Soc.*, **162**, A1163 (2015).

55. R. Amin and Y.-M. Chiang, *J. Electrochem. Soc.*, **163**, A1512 (2016).

56. R. S. Anderssen, S. A. Husain, and R. J. Loy, *Anziam J.*, **45**, 800 (2004).

57. J. Klafter and M. F. Shlesinger, *Proc. Natl. Acad. Sci.*, **83**, 848 (1986).

58. P.G. de Gennes, *Macromolecules*, **35**, 3785 (2002).

59. A. Marabi, S. Livings, M. Jacobson, and I. S. Saguy, *Eur. Food Res. Technol.*, **217**, 311 (2003).

60. M. Ecker, T. K. D. Tran, P. Dechent, S. Käbitz, A. Warnecke, and D. U. Sauer, *J. Electrochem. Soc.*, **162**, A1836 (2015).

61. Y. Zhu and C. Wang, *J. Phys. Chem. C*, **114**, 2830–2841 (2010).

62. M. Park, X. Zhang, M. Chung, G. B. Less, and A. M. Sastry, *J. Power Sources*, **195**, 7904 (2010).

63. J. Yang, X. Zhou, J. Li, Y. Zou, Z. X. Wang, and J. Tang, *Mater. Chem. Phys.*, **135**, 445 (2012).

64. H. Guo, X. Li, X. Zhang, H. Wang, and W. Peng, *New Carbon Mater.*, **22**, 7 (2007).

65.K. Persson, V. A. Sethuraman, L. J. Hardwick, Y. Hinuma, Y. S. Meng, A. van der Ven, V. Srinivasan, R. Kostecki, and G. Ceder, *J. Phys. Chem. Lett.*, **1**, 1176 (2010).

66. C. T. Love, O. A. Baturina, and K. E. Swider-Lyons, *ECS Electrochem. Lett.*, **4**, A24 (2015).

67. S. Frisco, D. X. Liu, A. Kumar, J. F. Whitacre, C. T. Love, K. E. Swider-Lyons, and S. Litster, *ACS Appl. Mater. Interfaces*, **9**, 18748 (2017).

68. Z. Li, J. Huang, B. Y. Liaw, V. Metzler, and J. Zhang, *J. Power Sources*, **254**, 168 (2014).

69. Q. Liu, C. Du, B. Shen, P. Zuo, X. Cheng, Y. Ma, G. Yin, and Y. Gao, *RSC Adv.*, **6**, 88683 (2016).

70. M. Rosso, T. Gobron, C. Brissot, J.-N. Chazalviel, and S. Lascaud, *J. Power Sources*, **97**, 804 (2001).

71. M. Z. Mayers, J. W. Kaminski, and T. F. Miller III, *J. Phys. Chem. C*, **116**, 26214 (2012).

72. J.H. Cheng, A. A. Assegie, C.-J. Huang, M.-H. Lin, A. M. Tripathi, C. C. Wang, M. T. Tang, Y. F. Song, W. n. Su, and B. J. Hwang, *J. Phys. Chem. C*, **121**, 7761 (2017).

73. H. Honbo, K. Takei, Y. Ishii, and T. Nishida, *J. Power Sources*, **189**, 337 (2009).

74. X. Su, F. Dogan, J. Ilavsky, V. A. Maroni, D. J. Gosztola, and W. Lu, *Chem. Mater.*, **29**, 6205 (2017).

75. R. Mukherjee, A. V. Thomas, D. Datta, E. Singh, J. Li, O. Eksik, V.B. Shenoy, and N. Koratkar, *Nat. Commun.*, **5**, 3710 (2014).

76. J. Niu, R. Shao, J. Liang, M. Dou, Z. Li, Y. Huang, and F. Wang, *Nano Energy*, **36**, 322 (2017).

77. C. Uhlmann, J. Illig, M. Ender, R. Schuster, and E. Ivers-Tiffée, *J. Power Sources*, **279**, 428 (2015).

II. AlH_3 AND $LiBH_4$ CONFINED IN N-CONTAINING CARBON SCAFFOLDS: A COMPUTATIONAL AND EXPERIMENTAL STUDY

Hongyang Zou[1,†], Waruni Jayawardana[2,†], Xander Benziger[3], Brennan Dizdar[2,#], Christopher L. Carr[2], James L. White[4], Farid El Gabaly[4], Hyunjeong Kim[5], Kouji Sakaki[5], Paul Jelliss[3], Mark S. Conradi[1,6], Eric H. Majzoub[2,*]

1. Washington University, Dept. of Physics-1105, Saint Louis, MO 63130, USA
2. University of Missouri- St. Louis, Center for Nanoscience and Department of Physics and Astronomy, One University Blvd, St. Louis, MO, 63121, USA
3. Department of Chemistry, Saint Louis University, St Louis, Missouri, 63103, USA
4. Sandia National Laboratories, Livermore, California 94550, USA
5. National Institute of Advanced Industrial Science and Technology, 1-1-1 Higashi, Tsukuba, Ibaraki 305-8565, Japan
6. ABQMR Inc., Albuquerque, New Mexico 87106, United States

Prepared for the submission to Journal of Physical Chemistry.

*author for correspondence

† these authors contributed equally

current address- Physics Department, Harvard University, Cambridge, Massachusetts 02138

ABSTRACT

$LiBH_4$ and AlH_3 are both attractive hydrogen storage candidates with substantial hydrogen capacity, but the thermodynamics and kinetics of the hydriding and dehydriding processes are unfavorable. Confining metal hydrides in nanosize carbon scaffolds can alter the thermodynamics and kinetics. The size effect has been well studied, but the chemical interaction between the metal hydrides and the carbon scaffold is not clear. Nitrogen-containing carbon scaffolds may provide a specific type of easily observed interaction; the formation of a Lewis-acid/base complex with infiltrated B-H and Al-H moieties. ^{15}N NMR for ^{15}NCMK3-type carbon scaffold indicates both pyridinic ^{15}N and pyrrolic ^{15}N. This interaction may allow a degree of control on the kinetics and possibly thermodynamics of nano scale hydrides confined in the pores. DFT calculations indicate many favorable binding sites in the scaffold where solution-bound AlH_3 in an amine-based adduct such as dimethylethylamine alane (DMEAA) may exchange with surface pyridinic N on the scaffold. Moreover, calculations show alane will also bind strongly with non-nitrogen-containing defect sites on the carbon scaffold as well. We report XRD, XPS, NMR, synchrotron X-ray, and gas desorption measurements for AlH_3 infiltrated into the carbon scaffolds under different conditions. Our results suggest that low-oxygen content scaffolds may provide the best hosts.

1. INTRODUCTION

Energy storage for transportation is increasingly moving away from fossil fuels and toward electrochemical and other technologies including hydrogen storage. Hydrogen-powered vehicles utilizing a proton-exchange membrane (PEM) fuel cell will

likely be the technology that supplants battery-powered transportation. Barriers to this technology include issues with the storage of hydrogen in solid form, where the thermodynamics of the charge/discharge process dictate the feasibility of a material.

Lithium borohydride ($LiBH_4$) and alane (AlH_3) are two of the top candidates for solid-state hydrogen storage. They both have a large mass-fraction of potentially reversibly stored H, (13.6 wt %) for $LiBH_4$[1] and (10.1 wt %) for AlH_3[2]. However, the enthalpy change during hydrogen desorption is too high for $LiBH_4$ (75 kJ/mol H_2) and too low for AlH_3 (11 kJ/mol H_2.[3] The large enthalpy of $LiBH_4$ requires high temperatures for desorption and also requires extensive thermal management if used in a hydrogen bed. The low enthalpy of alane means a very large overpressure (10^5 bar) of hydrogen gas is necessary for reversibility. These hydrides are generally not reversible under modest conditions in their pure form. To meet the Department of Energy requirement for onboard hydrogen storage applications, porous scaffolds have been studied to modify the thermodynamics and kinetics of the metal hydrides.[1,3–6] Confining metal hydrides in these porous scaffolds leads to a large increase the surface-area to volume ratio of the hydride, large surface interface between hydride and scaffold, allowing some control of the interfacial energies between the scaffold and the hydride.

Nano porous carbon have been used to infiltrate several different metal hydrides such as $LiBH_4$ [3,7], $NaAlH_4$ [4], $Li_4BN_3H_{10}$ [8] extensively. Previous NMR studies of $LiBH_4$ in carbon scaffold found that the layer of $LiBH_4$ near the scaffold walls have rapid reorientations and faster translational diffusion of BH_4^- anions.[1] In a recent study by Carr and Majzoub, the effect of nitrogen functionalization of the carbon scaffold on the metal hydride has been investigated and showed that using nitrogen doped carbon scaffolds can

increase the activation energy of $LiBH_4$ by ~30 kJ/mol compared to using undoped carbon scaffolds.[3] This study indicates kinetic stabilization of the hydride due to the N heteroatoms in the scaffold. This result is contrary to previous work showing that metal hydrides can be destabilized through confinement in nanoporous scaffolds; some materials show stabilization depending on the surface chemistry of the scaffold. There is limited fundamental understanding of the interaction between porous scaffold surface and metal hydrides. In this paper, we investigate the possibility that pyridinic nitrogen and the infiltrated hydrides may be acting as a Lewis-acid/base complex.

In order to understand the bonding between the infiltrated material and the N-containing carbon scaffold through NMR, it is important to use ^{15}N. The abundant isotope for nitrogen is ^{14}N, which is spin one with an electric quadrupole moment, making the NMR experiments difficult or impossible. Here we melt infiltrate $LiBH_4$ into ^{5}NCMK3 carbon scaffolds (synthesis described below) or solution infiltrate AlH_3 into ^{15}NCMK3 carbon scaffold with dimethylethylamine-alane (DMEAA) solution.

Our investigation includes characterization using ^{15}N NMR, synchrotron X-ray pair-distribution analysis (PDF), H_2 gas desorption, and a first-principles/density-functional theory (DFT) study of the interaction between the nitrogen nuclei on the scaffold and the metal hydrides. We will show that both $LiBH_4$ and AlH_3 interact with the pyridinic nitrogen on the carbon scaffold both experimentally and through our computational results. In addition, we show that the oxygen reduction pre-treatments on the carbon scaffold and lower temperature conditions for the solution infiltration of AlH_3 in these scaffolds can increase the amount of AlH_3 that can be infiltrated.

2. COMPUTATIONAL METHODS

Density functional theory and first-principles calculations: Electronic structure and total energy calculations were performed with the quantum chemistry code General Atomic and Molecular Electronic Structure System (GAMESS)[9,10] and/or the density functional theory (DFT) plane wave code Vienna Ab-initio Simulation Package (VASP)[11–14]. Non-periodic binding energies of alane with DMEA, pyridine, and ammonia were calculated in the gas phase using GAMESS and VASP as a benchmark for VASP calculations on the larger carbon scaffold systems. GAMESS calculations of the binding energies for DMEA-alane (DMEAA), ammonia-alane, and pyridine-alane were calculated using four levels of theory. (1) Restricted open shell Hartree-Fock (ROHF) with the Pople N31G basis set, (2) unrestricted Hartree-Fock (UHF) with DFT using the PW91 (V6) exchange correlation functional and the Pople N311G basis set, (3) the hybrid B3LYP with UHF, and (4) the highest level using G3MP2 with restricted HF.

Plane wave cut-off energies of 300 eV were used in the VASP calculations with some specific calculations repeated at 600 eV for structures that include heteroatom pyridinic nitrogen on the carbon scaffold. For all VASP calculations projector augmented wave (PAW) pseudopotentials[15] were used for the interaction of the electrons with the ions. The generalized gradient approximation[16] was used with the exchange correlation of Perdew and Wang (PW91)[17]. All calculations were performed at the gamma point except the few that employed a 600 eV cutoff, where they used a 2×2×2 Monkhorst Pack[18] grid. All structures and adsorbates were relaxed using conjugate gradient methods in VASP until the forces on the ions were below 0.005 eV/Å.

In order to make the calculations tractable we used a 98 atom monolayer sheet (7x7x1 graphene supercell) as the scaffold, following Mason et al.[19]. A study by Valencia et al.[20] indicates that relaxation geometries are largely unaffected by additional graphene layers while binding energies tend to increase by approximately 0.1 eV upon the addition of a second layer and are unaffected by subsequent layers.

The primary graphene defects examined for alane binding include monovacancies, diamond and dogbone bivacancies, and trivacancies. Removing two adjacent atoms on a graphene sheet gives a diamond-shaped opening with four dangling bonds. Trivacancies fromed by removing three adjacent atoms leaves an opening with five dangling bonds. Finally, bivacancies formed by removing two atoms on opposite sides of a ring leaves a dogbone-shaped opening with six dangling bonds. Nitrogen heteroatoms were incorporated in the edge sites of the defected graphene sheets. In Table 1 the number of dangling bonds is $D=D_0-N_{hterm}-N_N$, where D_0 is the number of dangling bonds from removal of carbon atoms. The existence of pyridinic nitrogens in N-substituted carbons is well known experimentally and is approximately a third of all the nitrogen[3,4], the rest being pyrolic and quaternary. N/C ratios as large at 0.2 are possible through the preparation methods discussed in the experimental section. Given this fraction of nitrogen atoms, and the defect density of hard carbons of approximately 10^{20} cm^{-1} [21], an examination of up to two pyridinic nitrogens in the case of trivacancy and three in the case of monovacancy is reasonable. The remaining carbon atoms in the defects may also be hydrogen-terminated, given that graphene sheets naturally terminate their lattice ends in the presence of hydrogen. Increasing the number of hydrogen

terminated carbons increased the binding energy of AlH_3 to the surface, therefore all of the calculated results show fully terminated carbons in the defects.

After allowing the sheets to relax via DFT to their lowest energy configurations, a molecule of alane was placed on top of the sheet with an Al-N distance of 2.04 Å, the Al-N bond length in the pyridine-alane Lewis-acid/base complex. The alane was placed at one of two sites: directly above a nitrogen atom or in the center of the sheet defect. Relaxed structures in which the AlH_3 did not maintain its molecular integrity were discarded, these typically included structures without full hydrogen termination of the carbons in the defect, resulting in decomposition of the AlH_3 and hydrogen terminating those carbons.

The wetting or adsorption energy is defined as $E = (E_{ad} – E_s – E_m)/f.u.$, where E_{ad} is the total energy of the adsorbate and sheet, E_s the energy of the lone sheet, and E_m the energy of the lone adsorbate. Negative energies indicate thermodynamically favorable adsorption configurations for alane on the sheet. We note that gas-phase molecular alane is the thermodynamic reference in this definition. Adsorption energies were then compared to the binding energies of alane to several Lewis-acid/base complexes, e.g. DMEA. A larger adsorption energy than binding energy in the complexes suggests a favorable chance of a change of bases for the alane from the molecule to the sheet.

3. EXPERIMENTAL METHODS

Sample preparation: A variety of carbon scaffolds were prepared, with the following nomenclature. NPC = nanoporous carbon (no added heteroatoms); NNPC = nitrogen-containing NPC; CMK3 = nanoporous carbon prepared as described below;

NCMK3 = nitrogen-containing CMK3. NPC and NCMK3 carbons were prepared using both soft and a hard templating techniques. In the NPC synthesis procedure, mesoporous structures were obtained from inorganic-organic-surfactant tri-constituent co-assembly process. NPC was prepared using phenolic resol as the carbon precursor, silicate oligomers as the inorganic precursor and triblock co polymer as the soft template. NCMK3 preparation procedure involves polymerization reaction between ethylenediamine (EDA) and carbon tetrachloride (CTC). In this procedure, SBA-15 was used as the hard templating material and EDA as the nitrogen source. Detail descriptions of preparation procedures for these two carbon types can be found in the previous publications.[3,4,22,23] The ^{15}NCMK3 was prepared according to the same procedure as NCMK3 but, with replacing regular EDA with ^{15}EDA for the better NMR experiments. An additional step was followed to get the reduced oxygen NPC carbon as follows. NPC carbon sample was loaded in to the furnace and the furnace tube was purged with Ar gas overnight. While the system was flushing with 5 % H_2 gas and 95 % Ar gas mixture with 100 cc/min rate, the sample was heated to 700 °C at a rate of 5 °C/min, and soaked for 2 hours at 700 °C. After that it was allowed to cool down under the same gas mixture. All the carbon scaffolds were baked at 300 °C overnight under vacuum to remove moisture prior to the infiltrations.

Melt infiltration of ^{15}NCMK3 with $LiBH_4$ was carried out using the Sieverts-type apparatus. The targeted pore filling was 30 %. The calculation was based on the total pore volume of the ^{15}NCMK3 and the mass and the bulk density of the $LiBH_4$ (0.666 g/cm^3). The sample mixture was packed inside the sealed stainless-steel sample holder followed by a mixing step of $LiBH_4$ and ^{15}NCMK3 using mortar and pestle. The mixture

was then heated to 300 °C (above the melting temperature of $LiBH_4$), soaked for 40 min under 100 bar of H_2 pressure and allowed to cool to room temperature under pressure.

Solution infiltration of alane using dimethylethylamine alane (DMEAA) complex solution (0.5 M in toluene) was carried out with two different AlH_3 to carbon mass ratios. In a typical loading procedure, carbons were suspended in ~ 6 ml of toluene and then a calculated amount of DMEAA was added. Next, the mixture was continuously stirred for 3 days. After three days, the carbons were allowed to settle down to the bottom of the flask and the supernatant was removed. Finally, carbon samples were vacuumed to remove residual solvents.

In the low loading samples (AlH_3: carbon= 1:10), to remove the excess DMEAA, samples were washed using toluene until no Dimethylethylamine (DMEA) NMR peaks were observed from the ^1H NMR of the washed away toluene solution. This step resulted in removing some of the added DMEAA from the mixture and hence the exact final loading between AlH_3 and carbon was not precisely known in the system. Higher loading samples (AlH_3: carbon= 1:1) were made without the washing step with toluene. Two different vacuum temperatures (25 °C and 40 °C) were used in the higher loading sample preparation in order to investigate the temperature effect on the final product. Finally, for comparison, DMEAA powder was made by vacuuming the commercially bought DMEAA solution at 25 °C.

Characterization measurements: Nitrogen adsorption desorption isotherms were measured with SA3100 (Coulter) analyzer at 77 K. First, all the carbon samples were outgassed at 300 °C for 12 h, and then loaded into the sample holder inside the glove box (O_2 < 1 ppm, and water < 0.5 ppm). The Brunauer-Emmett-Teller (BET) method was

used to calculate the specific surface area (S_{BET}) from the adsorption isotherm branch in a relative pressure range from 0.02- 0.5 bar. Both total pore volume (V_{Total}) and the pore size distributions were calculated using Barrett-Joyner-Halenda (BJH) method. The total pore volume was estimated from the adsorbed amount at a relative pressure P/P_0 of 0.98. X-ray photoelectron spectroscopy (XPS) was performed under UHV conditions (residual pressure better than 1 × 10−8 Torr) using a Physical Electronics 10−360 electron energy analyzer and an Omicron DAR400 Al K-alpha (photon energy = 1487 eV) or Mg K-alpha (photon energy = 1254 eV) X-ray source. Indium foil was used to mount the dried carbon samples. Samples were transferred to the spectrometer from the glove box without an air exposure using a clean transfer holder. All XPS peaks were baseline corrected using a Shirley background, and synthetic peaks of mixed Gaussian−Lorentzian (70%/30%) line-shape were used to fit the spectra. Spectra were calibrated to the main C 1s peak at 284.5 eV.

Powder X-Ray diffraction (PXRD) measurements were taken with a Rigaku Ultima IV X-Ray diffractometer with Cu K_α radiation source. Mylar film was used to prevent the sample from contacting the air or moisture during the measurements.

For nuclear magnetic resonance (NMR) studies, samples were packed into 5 mm OD pencil rotors (for measurement on a 7.04 T magnet) and 2.5 mm OD pencil rotors (for measurement on a 13.86 T magnet) inside an argon glove box (1 ppm H_2O, 0.5 ppm O_2). During the transportation and storage, the packed rotors were sealed inside a glass vial, which was then sealed in two layers of plastic ziplock bags filled with desiccant to make sure they were not air exposed. All magic angle spinning (MAS) measurements were made at room temperature. N_2 boil-off from a liquid nitrogen dewar supplied pure

N_2 gas for the bearing and drive gas needed to spin the rotors, thus inhibiting air-related degradation of the samples. The chemical shift in parts per million (ppm) of the ^{15}N and ^{27}Al peaks were externally referenced to ^{15}N labeled glycine powder (0 ppm) and 1.0 M $Al(NO_3)_3$ aqueous solution (0 ppm), respectively.

The ^{15}N MAS (F_S=25 kHz) NMR measurement in Figure 2 were performed using a Redstone spectrometer and Bruker 2.5 mm probe on a 13.86 T ^{15}N frequency 59.769 MHz superconducting magnet. The Hahn echo pulse sequence is 90^0 pulse (11.8 μs), wait tau time (40 μs), and then followed by a 180^0 pulse (23.6 μs). The cross-polarization magic angle spinning (CPMAS) pulse sequence is a 90^0 pulse (3.2 μs) in ^1H channel followed by 1 ms contact time. In the contact time, there is a pulse in ^{15}N channel that follows the Hartmann-Hahn condition while it is the spin lock pulse in ^1H channel. After the contact time, acquire NMR signal in ^{15}N channel.

The ^{15}N MAS (F_S=5 kHz) NMR measurement in Figure 3 were performed using a Redstone spectrometer and 5 mm Otsuka electronics probe on a 7 T (^{15}N frequency 29.89 MHz) superconducting magnet. The Hahn echo pulse sequence is 90^0 pulse (8.5 μs), wait tau time (200 μs) and then followed by 180^0 pulse (17 μs). The ^{27}Al MAS NMR measurement in Figure 6 were performed using a home-built spectrometer and 5 mm Chemagnetics probe on a 7.04 T (^{27}Al frequency 78.085 MHz) superconducting magnet. The spectra were obtained after central transition 90^0 pulse (1.2 μs).

4. RESULTS AND DISCUSSION

All calculations were performed in VASP with a cutoff of 300 eV. All structures below retain the AlH_3 molecule integrity.

Table 1. Alane binding energies in eV.

Structure	no. terminating hydrogen atoms	no. nitrogen atoms	Alane binding energy [eV]	Nearest Al-N distance [Å]
bivacancy/armchair_1H	5	1	-4.80*	2.085
monovacancy/0H_CENT	3	0	-2.33	--
trivacancy/0H_CENT	5	0	-2.19	--
trivacancy/1H_FAR1_PERP	4	1	-2.09	2.210
trivacancy/1H_PERP_ALTLOC	4	1	-1.88	2.075
special/edge_on_edge_	all	1	-1.74	1.990
trivacancy/1H_CENT	4	1	-1.70	2.120
trivacancy/2H_CENT	3	2	-1.57	2.125
monovacancy/1H_PERP	2	1	-1.42	2.155

Table 1. Alane binding energies in eV. (cont.)

DMEA-alane	--	1	-1.40	2.075
special/strip_3N_ (edge 3N)	0	3	-1.28	2.025
special/strip_5N_	0	5	-1.24	2.000
trivacancy/2H_PERP	3	2	-1.24	2.195
monovacancy/2H_PERP	1	2	-1.13	2.120
trivacancy/1_PARTIALH**	2	1	-1.07	2.095
trivacancy/3H_CENT	2	3	-0.82	2.135
monovacancy/1_PERP**	0	1	-0.75	2.100
special/strip_1N_	0	1	-0.61	2.060
trivacancy/1_CENT**	0	1	-0.51	2.175
* calculated at 600 eV cutoff with 2×2×2 kpoint mesh				
** dangling bonds present in the opening				

Computational results and discussion: The binding energies of gas-phase alane to several molecules is shown in Figure 1 where, in particular, the binding energy of AlH_3-DMEA is about 1.4 eV. Our calculated binding energies are in agreement with the high

level of theory calculations in Allendorf, et al.[24]. Several favorable configurations, those with a binding energy greater than 1.4 eV, for the adsorption of alane onto the nitrogen doped graphene were found as shown in Table 1. The most favorable configuration observed was an AlH_3 molecule placed near the center of a bivacancy with a single pyridinic nitrogen, and the second is a monovacancy with no heteroatom nitrogen. The bivacancy binding energy in Table 1 is far larger than the rest of the entries, whose values are closer to the gas-phase binding energies shown in Figure 1. The large energy difference in this case is likely due to the larger number of terminating hydrogen atoms in the sheet. The geometries of this structure are shown in Figure S1. The variation of the binding energy with the number of nitrogen atoms or hydrogen atoms in the defects are shown in Figures S1, S2. The correlation is clear for the number of terminating hydrogen atoms, where an increase in the binding energy occurs with more terminating hydrogen. Evidently, five terminating hydrogen atoms with one pyridinic nitrogen results in particularly strong binding.

In general, it was observed that the adsorption energy of alane onto the sheets becomes less favorable as the number of pyridinic nitrogen atoms increases. However, as the number of nitrogens decreases, more terminating hydrogens should be present, and given that the adsorption energy decreases going from five terminating hydrogens to four terminating hydrogens in a trivacancy, the trend with the number of N atoms may be attributable to the presence of more terminating hydrogen and not higher nitrogen doping. Adsorption energies tend to be higher in trivacancies than in monovacancies for nitrogen-doped sheets, this may be due to less hydrogen present in the monovacancy but also

because a smaller defect offers the alane less space to reorient itself to be exposed to the nitrogen lone pairs.

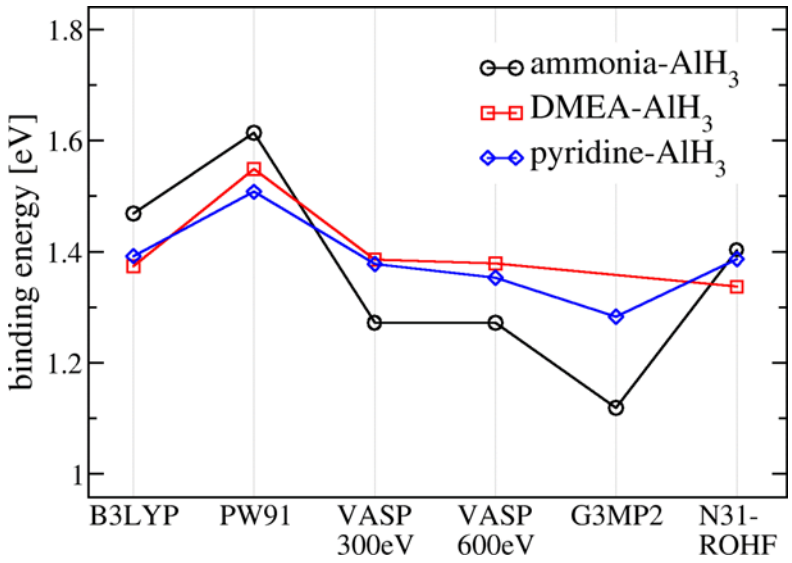

Figure 1. Benchmark calculations comparing gas-phase molecular binding energies from GAMESS and VASP.

In the case of three pyridinic nitrogens within a monovacancy, alane was observed to decompose into an AlH in the center of the monovacancy and gas-phase hydrogen. In larger defects the presence of hydrogen may prevent the alane from approaching the lone pairs closely enough, further inhibiting decomposition. As mentioned, graphene sheets were observed to self-terminate with hydrogen from the alane if it were placed closer to the sheet, also causing decomposition of the alane.

Density of States (DOS) for electron configurations were calculated using VASP. The electronic DOS indicate sharing of electron density between alane and terminating hydrogens of a graphene sheet. See Figure S4. Most adsorption relaxations ended with at least one terminated hydrogen protruding from the sheet towards the alane. The Al and

the terminating hydrogen closest to it share electron density between the Al p-orbital and the hydrogen s-orbital. The density in the Al s-orbital also increases as the number of terminating hydrogen atoms increases, and may explain the larger binding energies in Table 1. The proximity of one of the terminating hydrogen atoms to approach the AlH_3 may be an attempt at the formation of an AlH_4 moiety on the surface. But this cannot be completed because there is not enough electron density to donate; the surface chemistry is simply not favorable for this to occur.

Several adsorbate relaxations displayed significant curvature of the sheet geometry. As the terminating hydrogens flipped either downwards towards the alane or upwards, often in pairs, they would simultaneously pull carbon atoms in their vicinity with them, deforming the sheet around the defect. The DOS do not indicate a disparity in electron density between terminating hydrogens, so their displacement is not due to newly induced repulsion from reorganization of charge density around the sheet defect. Additionally, the pyridinic nitrogen to which the alane is initially closest is also pulled towards the alane, further deforming the sheet.

In addition to vacancy defects, adsorption energies on graphene *edge* sites were also examined. In these calculations a straight edge of graphene is available for heteroatom substitution or hydrogen termination. While a single pyridinic nitrogen at an edge site did not display a favorable adsorption energy, three and five adjacent pyridinic nitrogens along an edge displayed an adsorption energy that, while still not favorable, was much closer to the binding energy of DMEA- and pyridine-alane. This is unsurprising given that the structure of the sheet edge resembles a sequence of pyridine molecules increasingly close as the sheet approaches a completely nitrogen edge.

Charge transfer: Bader charge analyses at the gamma point for DMEA and DMEA-alane in Table 2 shows that the nitrogen in DMEA gains about 0.3 *e* in binding with the alane to form DMEAA. This is the difference $|Q_{NDMEA}-Q_{NDMEAA}|$. The bivacancy configuration with the strongest binding energy shows a Bader charge of -0.89 *e* for N, and +1.67 for Al, indicating more electron transfer to the Al. This pattern is evident in the Bader charges for the trivacancy with 1 N and 4 terminating hydrogens. In Table 1, this configuration has a binding energy just above the DMEAA, but below the bivacancy with the largest binding energy, and has Bader charges in between these two. Explicitly, from lowest to highest binding energy the N charge is -1.10 *e*, -0.96 *e*, -0.89 *e*, and the Al charge is +2.11 *e*, +1.78 *e*, +1.67 *e*. The larger the charge transfer, the stronger the binding.

DFT calculated borane binding energies are shown in Table S1. In the case of borane binding to the defected sheets we also see a clear correlation between an increase of the binding energy and more terminating hydrogen atoms. See Figure S5. Providing a comparison, the binding energy in ammoniaborane (H_3B-NH_3) is about 1.5 eV. The results again show that many defect configurations in the scaffold should be present that preferentially bind BH_3 over competing ligands.

Results of a Bader charge analysis of ammonia borane is included for reference and are shown in Table S2. A Born effective charge analysis of solid ammonia borane gives charges of about Q_N= -0.63 *e*, Q_B= +0.56 *e*.

Table 2. Bader charge analysis of DMEA and DMEAA at the gamma point. Total charge is given.

Atom	total no. *e*	Bader charge [*e*]
N (DMEAA)	8.10	-1.10
Al (DMEAA)	10.89	+2.11
H1, H2, H3 (AlH_3, DMEAA)	1.70	-0.70
N (DMEA)	7.80	-0.80
bivacancy/armchair_1H		
N no alane, with 5 terminating hydrogen	8.08	-1.08
N no alane, no terminating hydrogen	8.06	-1.06
N with alane and terminating hydrogen	7.89	-0.89
Al	11.33	+1.67
trivacancy/1H_CENT		
N	7.96	-0.96
Al	11.22	+1.78

In summary, the DFT and first-principles calculations indicate that many common defects in the carbons with heteroatom N will bind to the alane (borane) significantly

more strongly than does DMEAA (competing ligands) and should simply exchange the AlH_3 (BH_3) with the surface pyridinic nitrogens.

Experimental results and discussion: In this work we used two different carbon morphologies, namely NPC and CMK3. NPC geometry consists of cylindrical pores in the 2D hexagonal *P6m* symmetry[22] and CMK3 is composed of cylindrical carbon rods[25] exhibiting the inverse replica of NPC structure. In order to understand the interaction between the carbon scaffold and the metal hydrides we have used the ^{15}N enhanced version of the NCMK3 carbon (^{15}NCMK3). Figure S6 shows the nitrogen adsorption desorption isotherms and the pore size distributions (inset) for the NPC and ^{15}NCMK3. Both carbon scaffold samples show type IV isotherms[26] indicating microporosity and mesoporosity. Total surface area for the NPC and NCMK3 are 1290 m^2/g and 587 m^2/g respectively. According to the pore size distributions, NCMK3 has slightly smaller pores compared to NPC. Our previous studies show both of these geometries can be successfully infiltrated by complex metal hydrides such as $LiBH_4$ [3] and $NaAlH_4$[4]

Table 3. Summary of XPS results for carbon scaffolds.

Sample	carbon content [atom%]	oxygen content [atom%]	nitrogen total [atom%]	pyridinic nitrogen [atom%]	pyrrolic nitrogen [atom%]	quaternary nitrogen [atom%]	oxidized nitrogen [atom%]
^{15}NCMK3	79.3	11.3	9.5	3.8	4.8	0.6	0.3
NPC	95.7	3.9	< 1	-	-	-	-

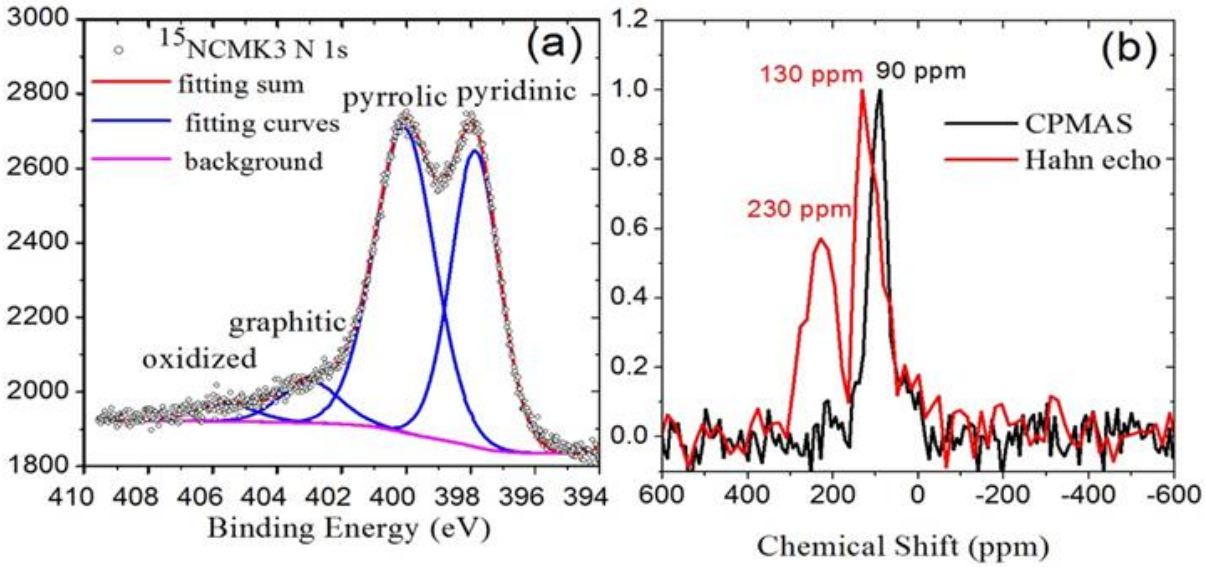

Figure 2. (a): N 1s spectra for ^{15}NCMK3 carbon. Four different chemical bonding environments were identified from the XPS measurement. They are pyridinic (~398 eV), pyrrolic (~400 eV), graphitic (~402 eV), and oxidized (402-405 eV) nitrogen. (b) ^{15}N MAS (f_S = 25 kHz) NMR spectra for ^{15}N labeled NCMK3 carbon scaffold. The spectra are normalized. The red one is obtained with Hahn Echo, tau time between 90^0 pulse and 180^0 pulse is 40 µs. The 230 ppm peak is the pyridinic and the 130 ppm peak is the pyrrolic. The black one is got with CPMAS from ^{1}H to ^{15}N, with contacting time 1 ms. In the CPMAS spectrum, there is only one peak around 90 ppm and no peak around 130 ppm. We assign the ^{15}N peak around 130 ppm as pyrrolic nitrogen which has lost the ^{1}H attached to it, the ^{15}N peak around 90 ppm as pyrrolic nitrogen has ^{1}H attached to it and the ^{15}N peak around 230 ppm as the pyridinic nitrogen.

Table 3 shows the summary of XPS survey scans and Figure 2a shows the N 1s spectra for ^{15}NCMK3 sample. In addition to the main carbon component both of the samples contain oxygen impurities according to the survey. Four different chemical bonding environments for nitrogen can be identified from the XPS analysis. They are pyridinic (~398 eV), pyrrolic (~400 eV), graphitic (~402 eV), and oxidized nitrogen.[27,28] Out of these four types of nitrogens, the pyridinic nitrogen which is in sp^2 hybridization and has a lone pair of electrons attracts the most attention. Because, these electrons are

available to bond with the host atoms. In an infiltrated system such as $LiBH_4$ or AlH_3, the pyridinic nitrogen can act as a Lewis base by donating its lone pair.

The Hahn echo instead of a simple pulse acquire is used here to get rid of the acoustic coil disease in the beginning part of the free induction decay (FID). From the Hahn echo spectrum in Figure 2b, there are two species of ^{15}N in the system. The two peaks (230 ppm and 130 ppm) of ^{15}N in the NMR Hahn echo spectra correspond to the pyridinic and pyrrolic nitrogen in the XPS spectra in Figure 2a because those two components are the dominating nitrogen types in Figure 2a. In Figure 2b, the CPMAS is used to enhance the signal of nuclei with a low gyromagnetic ratio, ^{15}N, by magnetization transferred from nuclei with a high gyromagnetic ratio, ^{1}H. To establish magnetization transfer, the RF pulses applied on the two frequency channels must fulfill the Hartmann–Hahn condition, that is the rotation frequencies in both rf fields must be identical. With CPMAS from ^{1}H to ^{15}N, the only ^{15}N signal that appears will come from the ^{15}N coupled with ^{1}H. So the 90 ppm peak comes from the ^{15}N coupled with ^{1}H. From the molecular structure, the pyrrolic nitrogen coupled to hydrogen while the pyridinic nitrogen does not. In the Hahn echo experiment, the signal from short T_2 component lost more than that for long T_2 component, especially when the tau time between the 90^0 pulse and the 180^0 pulse is long. If the pyrrolic nitrogen lost the ^{1}H attached to it, the spin-spin relaxation rate for it will be smaller because of no ^{1}H hopping around it, and then T_2 will be longer. It is reasonable to think some of pyrrolic nitrogen may lose the ^{1}H attached to them when the carbon scaffolds are baked before using and the non-protonated pyrrolic ^{15}N atoms are bonded to other ^{15}N or more likely to a carbon atom, otherwise there will be reactive fragments with an unpaired electron spin. In this situation, the Hahn echo ^{15}N NMR will

emphasize on the nitrogen without ^{1}H attached to it while lose some signal from the nitrogen with ^{1}H attached to it. For this reason, in Figure 2b, we assign the ^{15}N peak around 130 ppm as pyrrolic nitrogen which has lost the ^{1}H attached to it, the ^{15}N peak around 90 ppm as pyrrolic nitrogen has ^{1}H attached to it and the ^{15}N peak around 230 ppm as the pyridinic nitrogen. The ^{15}N CPMAS spectra with different contact times in Figure S13 also indicates the 230 ppm peak nitrogen is far away from ^{1}H, so it is the pyridinic nitrogen.

Figure 3 is the ^{15}N NMR spectra for four samples. ^{15}NCMK3 is the bare ^{15}NCMK3 carbon scaffold itself. AlH_3 in ^{15}NCMK3 low loading is the sample using DMEAA (AlH_3+ DMEA) solution infiltrated into the ^{15}NCMK3 carbon scaffold at 40 °C with the AlH_3:carbon weight ratio 1:10. AlH_3 in ^{15}NCMK3 high loading is the sample using DMEAA (AlH_3+DMEA) solution infiltrated into the ^{15}NCMK3 carbon scaffold 25 °C with the AlH_3:carbon weight ratio 1:1. $LiBH_4$ in ^{15}NCMK3 is the melt-infiltrated sample. The pyrrolic nitrogen peak does not change with different infiltrations. Evidently, the pyrrolic nitrogen sites have no chemical affinity for AlH_3 and $LiBH_4$, in agreement with chemical intuition. On the other hand, from DMFIT in Figure S9, Figure S10, Figure S11, Figure S12, the pyridinic peak for ^{15}NCMK3 is at 231 ppm, for AlH_3 in ^{15}NCMK3 low loading at 231 ppm, for AlH_3 in ^{15}NCMK3 high loading at 217 ppm, for $LiBH_4$ in ^{15}NCMK3 at 211 ppm. This means the pyridinic nitrogen environment has been changed by the infiltrated material. The peaks labelled with * are the spinning sidebands of the pyridinic nitrogen peak. We see the spinning sidebands from the pyridinic nitrogen but not from the pyrrolic nitrogen. This is because the 5 kHz MAS is not fast enough

compared with the chemical shift anisotropy (CSA) for pyridinic nitrogen peak but fast enough compared with the CSA for pyrrolic nitrogen.

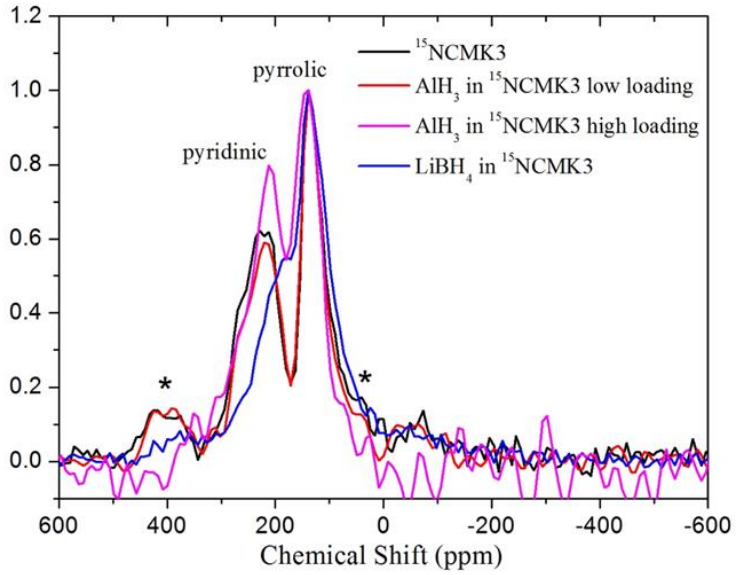

Figure 3. ^{15}N MAS (f_S = 5 kHz) NMR spectra got using Hahn echo, with tau time between 90 pulse and 180 pulse 200 µs. The spectra are normalized. The peaks labelled with * are spinning sidebands of the pyridinic nitrogen peak at 230 ppm. Pyrrolic nitrogen peak does not change with different loading. The pyridinic peak appear at for bare ^{15}NCMK3 at 231 ppm, for AlH_3 in ^{15}NCMK3 low loading at 231 ppm, for AlH_3 in ^{15}NCMK3 high loading at 217 ppm, for $LiBH_4$ in ^{15}NCMK3 at 211 ppm. The $LiBH_4$ appears to interact strongly with the pyridinic nitrogen sites compared with AlH_3.

AlH_3 infiltration: Originally, Brower et al. synthesized six different non-solvated alane phases α, α′, β, γ, δ and ε and a non-solvated or slightly solvated ζ phase using an organometallic synthesis.[29] The most commonly studied alane phases in the literature are α, β and γ. Of these phases the most stable phase, α, is known to be thermodynamically unstable at room temperature. But, this material can be prepared in a “kinetically stable” state with a surface oxide/hydroxide layer that prevents decomposition. Acording to a

thermal stability study of freshly prepared α, β and γ phases it was found that, during thermal treatments β and γ phases transition to more stable α phase prior to decomposition.[30] XRD spectrum for freshly made DMEAA powder prepared at room temperature is shown in the Figure 4a. The sample is a mixture of several different components with DMEAA powder, alane polymorphs and metallic Al according to XRD. Clearly, matching Bragg peaks for α AlH_3 and a predicted P63/m polymorph can be seen in the spectrum.[31] To our knowledge the P63/m structure has not been observed experimentally before. According to their DFT calculations, Ke et al., report two other computationally predicted polymorphs with orthorhombic and cubic symmetries that are more stable than the P63/m structure.[31] We suggest the occurrence of a metastable phase of alane in symmetry P63/m may have formed due to unique nucleation cites on the carbon surface, which suggests that the carbon surface may preferentially stabilize this polymorph. The formation of metallic Al observed in the spectrum is due to the decomposition of some alane during the drying of the DMEAA powder. A comparison of XRD results between freshly made DMEAA and DMEAA powder after one month is shown in the supplementary **S7**. According to the results freshly made DMEAA powder is not stable. The composition of the sample changes and partially decomposes over time with metallic Al and α alane peak intensities increased after one month.

For carbon scaffold mixed with DMEAA solution (0.5 M in toluene) during the infiltration, alane can either bind with the carbon or it can remain bound to DMEA as DMEAA. The goal is to vacuum dray all the DMEA and toluene away from the mixture to obtain a dry powder containing alane and carbon as the final product. However, some

solid DMEAA is still observed in the sample through XRD and is therefore outside the pores.

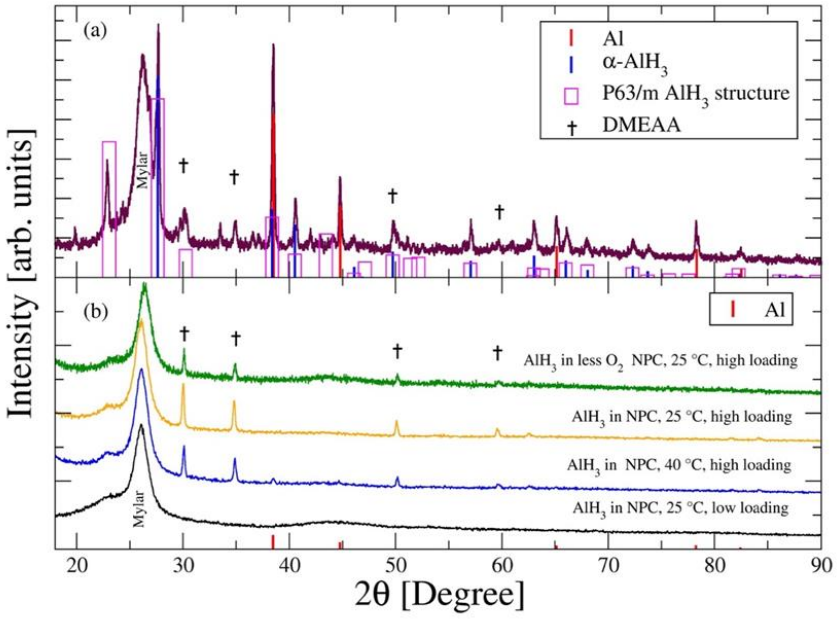

Figure 4. XRD results for DMEAA power (a) and infiltrated carbon samples (b). The peaks labelled with † are DMEAA peaks. DMEAA power shows two alane phases (alpha alane, p63/m).

Figure 4b includes spectra for higher loading alane samples prepared under different conditions, as well as a lower loading sample. The lower loading sample does not have any remaining DMEAA on the outside of the pores due to washing the process. But, higher loading samples have DMEAA and metallic aluminum outside the pores. There is a possibility of alane residing inside the pores of these samples. If alane is confined in the nanopores of the carbon, Bragg peaks for the alane are not expected to appear on the XRD spectrum. The amount of metallic aluminum observed depends on the synthesis conditions. All the higher loading samples showed metallic aluminum from the NMR measurements even though the sample prepared at 40 °C indicates no presence of

metallic aluminum from the XRD. This is probably due to the the small particle size of the metallic aluminum that has precipitated upon decomposition but has not agglomerated to a large enough particle size to be evident in the XRD.

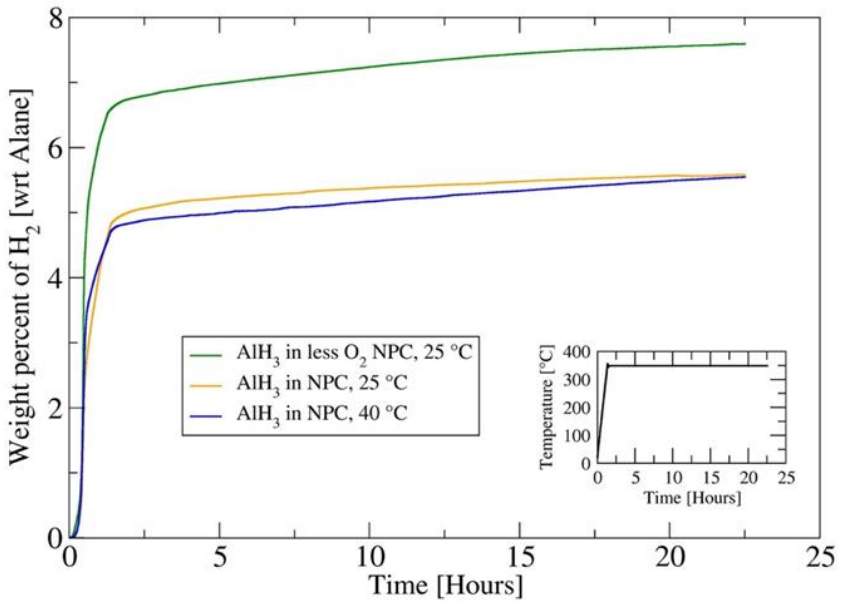

Figure 5. Desorption measurements for the higher loading alane infiltrated carbon samples. The highest hydrogen weight percent is for the AlH_3 in less O_2 NPC scaffold. The lower right inset shows the temperature vs time for the experiment.

Hydrogen gas desorption from the higher loading samples are shown in Figure 5. Weight percent numbers were calculated based on the initial added alane amount for the higher loading AlH_3 in NPC samples. According to the results, AlH_3 in the O_2 -reduced NPC, 25 °C, high-loading sample releases a higher amount of hydrogen compared to the other infiltrated samples. This indicates that reduction of surface oxygen in the carbons coupled with a larger loading of alane may allow infiltration. In the lower loading

samples, it is likely that almost all of the infiltrated alane was consumed in the formation of Al-O species.

In the higher loading samples Al-O species are still observed, but the additional H_2 gas desorption must be coming from either external or internal DMEAA, alane, or both. XRD also indicates that some DMEAA is outside the the carbon surface. For the reduced oxygen carbon sample, the weight percent with respect to alane and total mass is 7.59 % and 3.80 % respectively. The discrepancy between the pure alane (10.1 %) and the infiltrated sample could be due to the observed decomposition during infiltration. The weight percent can be increased by increasing the loading of alane. The pore filling of the higher loading samples are ~ 40 % of the pore volume (lower loading samples had a pore filling of ~ 4%) which indicates carbon scaffold has available free space for the more alane. It may be possible to increase the weight percent of hydrogen by synthesizing carbons with higher pore volumes.

The highest rate of desorption occurs around 135 °C for all the higher loading samples (see the Figure S8), while the highest desorption rate for pure AlH_3 occurs around 150 °C according to Temperature Programmed Decomposition (TPD) studies by Graetz, J et al.[32] Our ramp rate was 4 C/min, while Graetz et al. Used 2 C/min. The lowering of the desorption temperature in the infiltrated alane samples may be due to catalytic effects of carbon and may be purely kinetic.

In Figure 6, the ^{27}Al NMR spectra were acquired using a simple pulse-acquire method. The 1.2 μs pulse provides a broad RF excitation window, which is important for covering the large frequency shift range for different aluminum species. For AlH_3 in NPC, 40 °C, low loading sample, there is no aluminum metal at about 1640 ppm neither

before nor after desorbed at 350 °C, The peaks between 0 and 100 ppm are 4, 5 and 6 coordinates of aluminum oxide. These peaks are very stable that they do not change after exposed to air. After desorption at 350 °C, the ratio between 4, 5 and 6 coordinate aluminum atom of aluminum oxide changes slightly. These three peaks between 0 and 100 ppm cannot be AlH_3, otherwise aluminum metal will appear after desorption. From the XRD shown in Figure 4, there is nothing outside of the carbon scaffold, so for the low loading sample there is only aluminum oxide inside of the scaffold. The PDF measurements indicate low loading of AlH_3 in the scaffold results in an Al-O-C compound. The residual oxygen content in the scaffold synthesis process is the reason why low alane loading is not successful. The standard Gibbs Energy of Formation for Al_2O_3 is -16.40 eV[33] and oxygen clearly prefers to react with Al to form oxides rather than remain in the DMEA-alane complex or bind to a pyridinic nitrogen site in the carbon. Similar reactions of residual oxygen with infiltrated $NaAlH_4$ is also observed.[4] For AlH_3 in NPC, 40 °C, high loading sample, there are aluminum metal peak and aluminum oxide peaks before desorption. This means when we do the solution infiltration at 40 °C, some AlH_3 has already decomposed. The AlH_3 in DMEAA is not stable when it is dry even at room temperature and it decomposes into aluminum metal and H_2 gas slowly. (Figure S14) After desorption, the aluminum metal peak increases which means there is some AlH_3 before desorption. There is not a significant AlH_3 peak. It is because the AlH_3 peak is too broad and it is hard to see if it is a significant amount in the sample. For AlH_3 in NPC, 25 °C high loading sample, compared with AlH_3 in NPC, 40 °C high loading sample before desorption, there is less aluminum metal and there is a broad base within the +/- 500 ppm window. This means that in this sample less AlH_3 has

decomposed into aluminum metal during the infiltration and the AlH_3 peak is hidden in the broad base before desorption. For AlH_3 in O_2-reduced NPC, 25 °C high loading sample compared with a normal NPC carbon scaffold, there is more AlH_3 and less aluminum metal before desorption although there is still some aluminum oxide. For dry DMEAA powder itself the peak around 100 ppm is the AlH_3 which bonded to DMEA (DMEAA itself), because DMEAA solution has a peak around 100 ppm. The peak around 0 ppm is some mixed phase AlH_3 which does not bond to DMEA due to the DMEA being evacuated when the sample is dried. The AlH_3 peak is very broad so we can only get a rough estimate of the AlH_3 amount in the sample based on the +/- 500 ppm window. At the same time, we know all the aluminum metal that appears during desorption comes from the AlH_3. Aluminum oxide cannot become aluminum metal during desorption at 350 °C. So the area change of the aluminum metal peak indicates how much AlH_3 we had in each sample. Based on this, we calculate the relative AlH_3 amount in the five samples in Figure 6. From bottom to top they are 0: 3918: 6745: 10663: 33459. This agrees with the desorption measurements in Figure 5. The y axis of +/- 500 ppm window has been scaled by a factor of 10 compared with 1300 to 1900 ppm window to make them visible in the same spectra.

For the high loading samples, the integrated spectra area after desorption are bigger. This is because the ^{27}Al NMR signal for AlH_3 is too broad, about from -500 ppm to 500 ppm, when the magic angle spinning speed is 6 kHz. If the MAS speed is faster, the AlH_3 peak might be narrower but the rotors are not stable when we MAS faster than 6 kHz. The H_2 gas released from slow desorption and the leftover DMEA lead to the high pressure in the rotors during fast MAS because MAS will increase the rotor temperature.

To avoid a rotor crash, we can only spin below 6 kHz for the samples. When we analyze our NMR data, we left shift 15 µs on the FID to get rid of the dead time before taking the FFT. In this way, we will lose the broad signal on the order of 67 kHz (850 ppm). This is the reason the spectra areas are not the same before and after desorption. In short, a lower temperature drying step and less oxygen in the carbon are important for infiltrating AlH_3

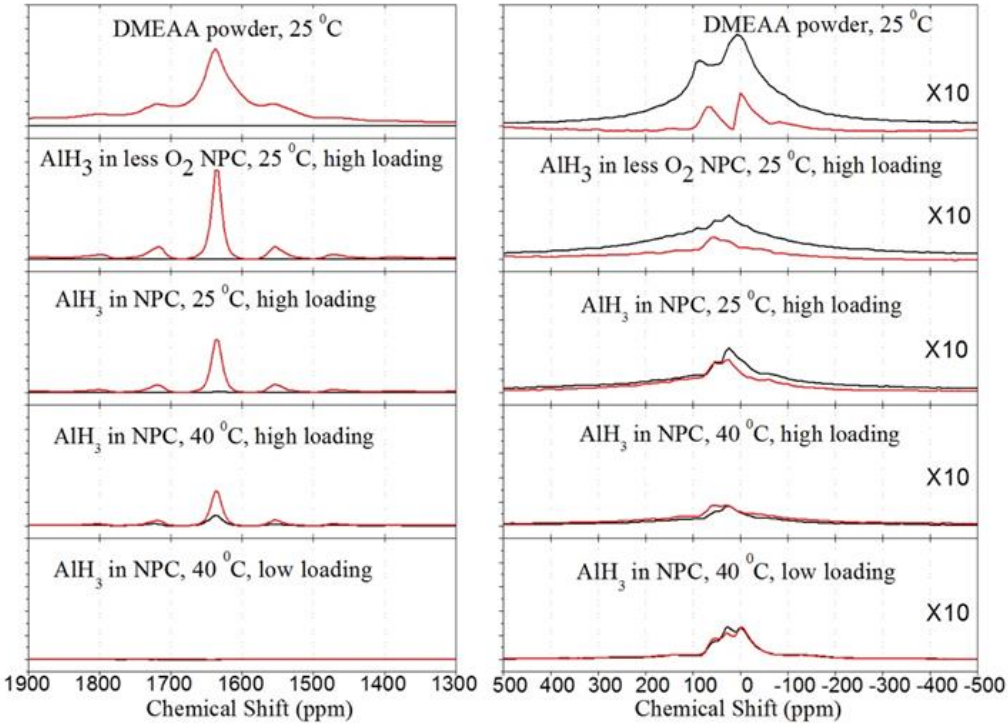

Figure 6. ^{27}Al MAS (f_S = 6 kHz) NMR spectra obtained using central transition pulse acquire. The black spectra are the samples before desorption, the red spectra are the samples after desorbed at 350 °C. The y axis of the spectra between +/- 500 ppm is zoomed in by 10 to make it visible on the spectra. In 1300-1900 ppm window, the peaks labelled with * are spinning sidebands of the (Knight-shifted) metallic aluminum peak.

5. CONCLUSIONS

Nitrogen-containing carbon scaffolds were studied as hosts for AlH_3 infiltration. XPS and ^{15}N NMR for ^{15}NCMK3 carbon scaffold confirm that two dominating nitrogen types on the carbon scaffold are pyridinic and pyrrolic. From the ^{15}N Hahn echo and CPMAS spectra, we assign the ^{15}N peak around 130 ppm as pyrrolic nitrogen which has lost the ^{1}H attached to it, the ^{15}N peak around 90 ppm as pyrrolic nitrogen has ^{1}H attached to it and the ^{15}N peak around 230 ppm as the pyridinic nitrogen. The pyridinic nitrogen peak in ^{15}N NMR spectra shifts to lower frequency when AlH_3 and $LiBH_4$ are infiltrated. The DFT and first-principles calculations indicate that many common defects in the carbons with heteroatom N will bind to the alane (borane) significantly more strongly than does DMEAA (competing ligands) and should simply exchange the AlH_3 (BH_3) with the surface pyridinic nitrogens. In ^{15}N NMR, this reflected in the chemical shift of the pyridinic nitrogen. $LiBH_4$ was observed to have a bigger influence on the pyridinic nitrogen peak chemical shift compared to AlH_3, so it coupled to the carbon scaffold wall more strongly than AlH_3. For pyrrolic nitrogen, the lone pair electrons of the nitrogen atom is actively involved with the two double bonds in the 5-member ring, making the ring aromatic, leading to greater stability of the molecule. While for pyridinic nitrogen, it has a stable conjugated system of 3 double bonds in the aromatic hexagonal ring, like benzene. For this reason, the lone pair electrons on pyridinic nitrogen can be easily donated to a Lewis acid, like BH_3 and AlH_3. BH_3 is stronger Lewis acidity compared to AlH_3, so we would expect the Lewis base/acid coupling for it is stronger.

From XRD and ^{27}Al NMR, the dry DMEAA powder has both DMEAA and some complex phase AlH_3 in it. It is not very stable and will decompose with time. Residual

oxygen in the scaffold from the carbon synthesis process reacts quickly with infiltrated DMEAA/alane to form Al-O and/or Al-O-C species for AlH_3 in NPC low loading sample. Lowering the oxygen content by passing a reducing gas over the carbons at elevated temperature is able to remove some of the surface oxygen in the carbons, but formation of Al-O species was still observed in ^{27}Al NMR. A more aggressive oxygen removal procedure appears necessary to achieve low loading of DMEAA/alane into the scaffolds. At higher loading, the infiltrated DMEAA/alane reacts with all of the available surface oxygen and allows the surviving material to either infiltrate the carbon or bind externally to the carbon surface. The ^{27}Al NMR signal for the AlH_3 is too broad to be seen on our 6 kHz MAS spectra, so the spectra intensities for the desorbed samples are bigger. If MAS speed is on the order of 100 kHz, we might be able to narrow down the AlH_3 peak for high loading samples. The aluminum metal amount after desorption in ^{27}Al NMR and the desorption measurements suggest that low-oxygen content scaffolds may provide the best hosts and using lower temperature can prevent the decomposition of AlH_3 during the infiltration.

ACKNOWLEGEMENTS

The authors acknowledge research support from the Hydrogen Materials Advanced Research Consortium (HyMARC), established as part of the Energy Materials Network under the U.S. Department of Energy, Office of Energy Efficiency and Renewable Energy, Fuel Cell Technologies Office, under Award Number DOE-EE0007656.

SUPPORTING INFORMATION

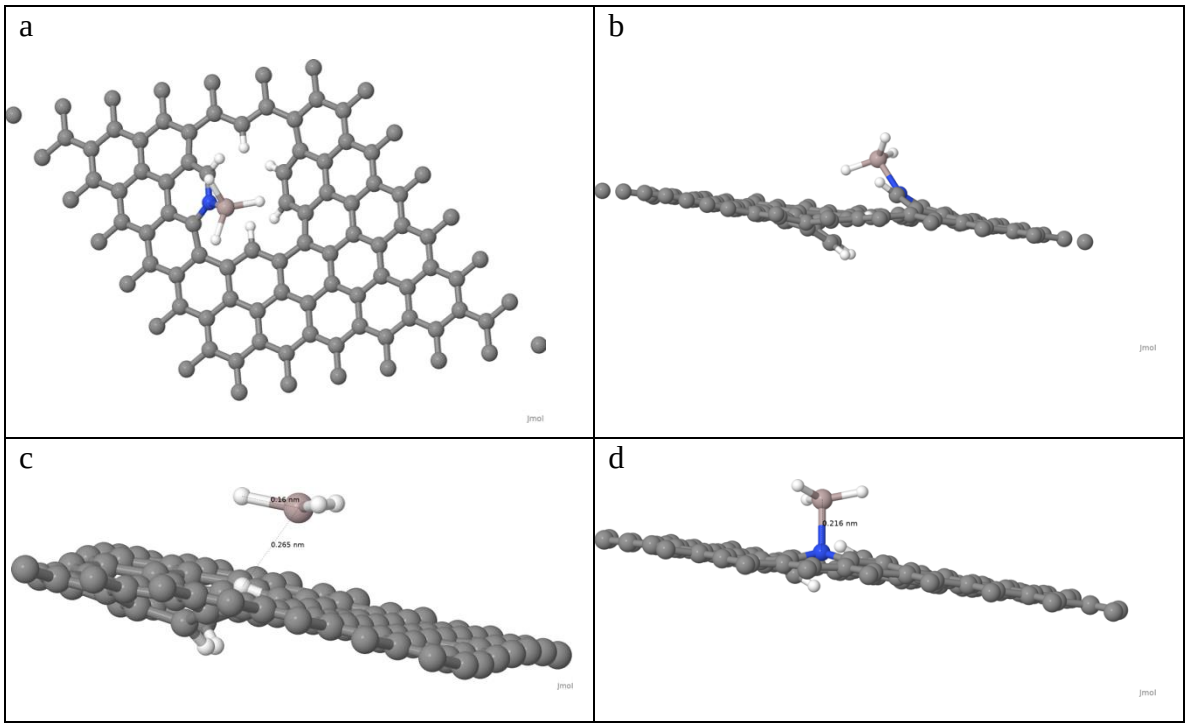

Figure S1. Bivacancy with 1 nitrogen, 5 terminating hydrogen atoms top view (a), side view (b). Monovacancy with 0 nitrogen, 3 termination hydrogen (c). Monovacancy with 1 nitrogen, 2 terminating hydrogen (d).

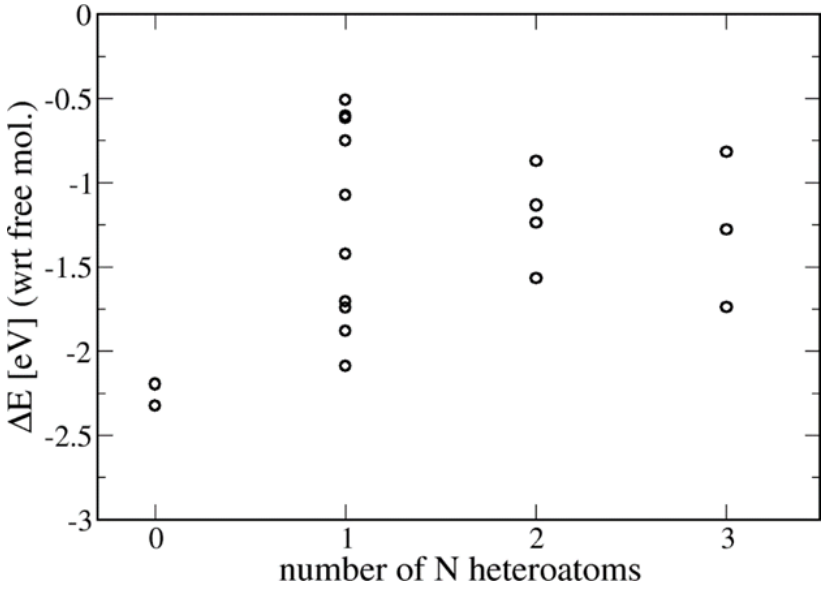

Figure S2. Alane binding energy as a function of the number of heteroatom nitrogen atoms.

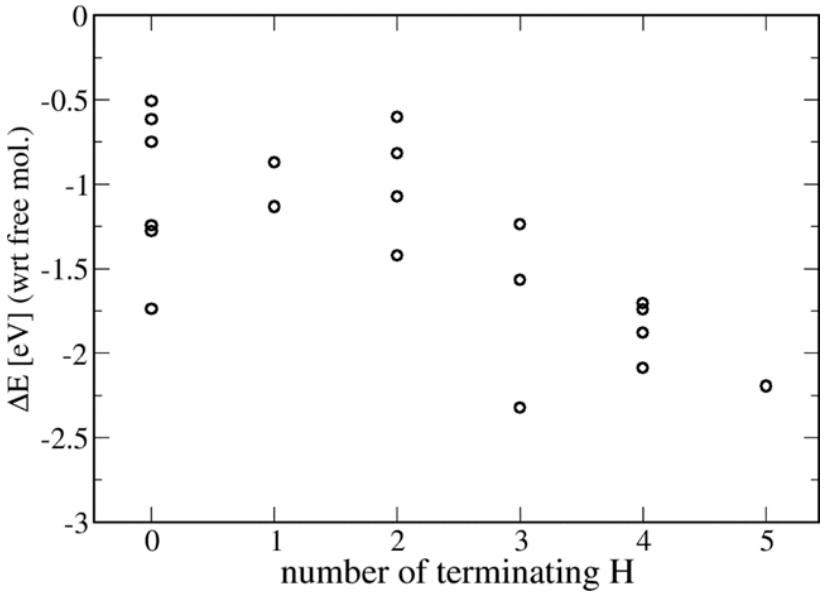

Figure S3. Alane binding energy as a function of the number of terminating hydrogen atoms.

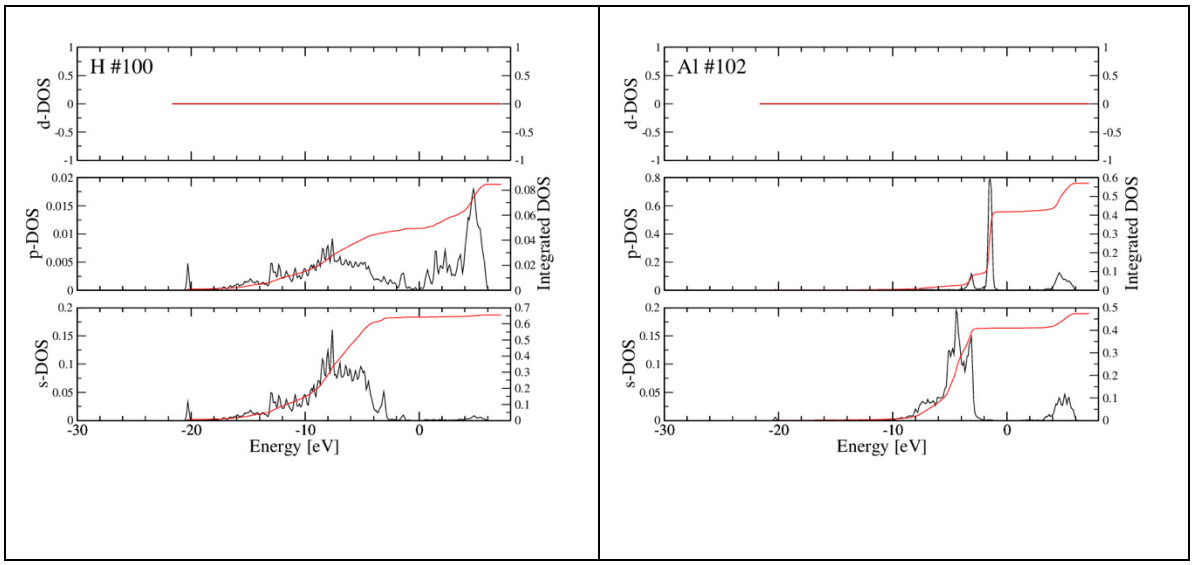

Figure S4. Electronic density of states for the closest terminating H near the Al in bivacancy/armchair_1H. The Al-H distance is 2.73 Å. The Fermi level is shifted to zero energy. Overlap in the DOS occurs for both p- and s-orbitals.

Table S1. Borane binding energies in eV. All calculations were performed in VASP with a cutoff of 300 eV. All structures below retain the BH_3 molecule integrity.

Structure	no.terminating hydrogen atoms	no. nitrogen atoms	Borane binding energy [eV]
tri_0H_perp	5	0	-2.110
tri_1H_perp	4	1	-2.175
tri_2H_perp	3	2	-1.206
mono_0H_PERP_SELDYN	3	0	-1.648
H_3B-NH_3	--	1	-1.530
mono_1H_PERP_SELDYN	2	1	-1.209
mono_1_PERP_SELDYN	0	1	-0.614
mono_2H_PERP_SELDYN	1	2	-1.025

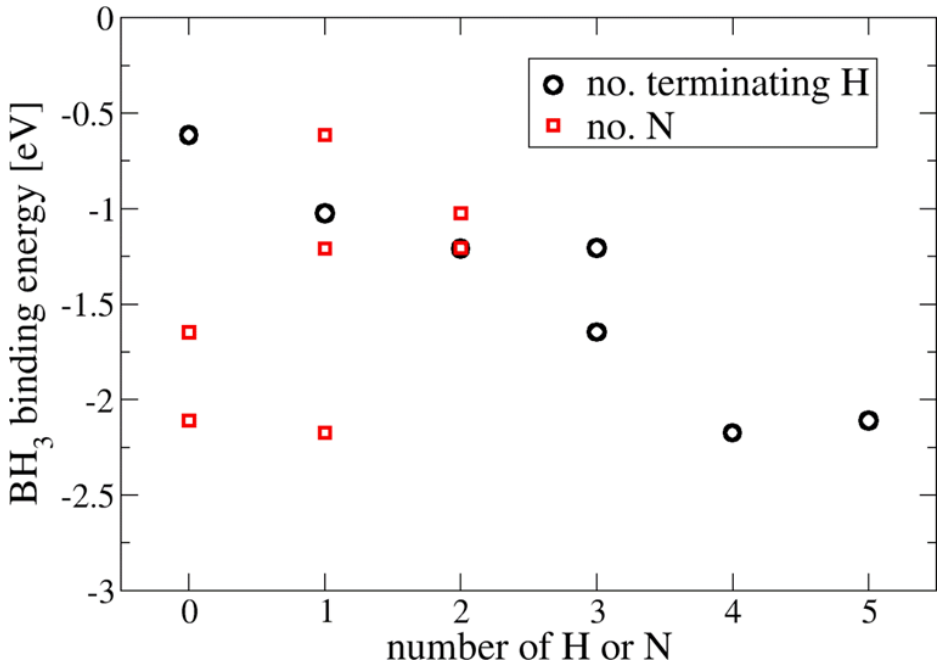

Figure S5. Binding energy of BH_3 to defective graphene sheets with nitrogen heteroatoms and terminating hydrogen atoms. Note the binding energy of (H_3B-NH_3) is about 1.53 eV.

Table S2. Bader charge analysis of gas-phase NH_3 and H_3B-NH_3 at the gamma point.

Atom	total no. *e*	Bader charge [*e*]
N (NH_3)	7.79	-0.79
N (H_3B-NH_3)	8.07	-1.07
B (H_3B-NH_3)	3.46	+1.54
H1, H2, H3 (H_3B)	1.56	-0.56
H1, H2, H3 (NH_3)	0.57	+0.57

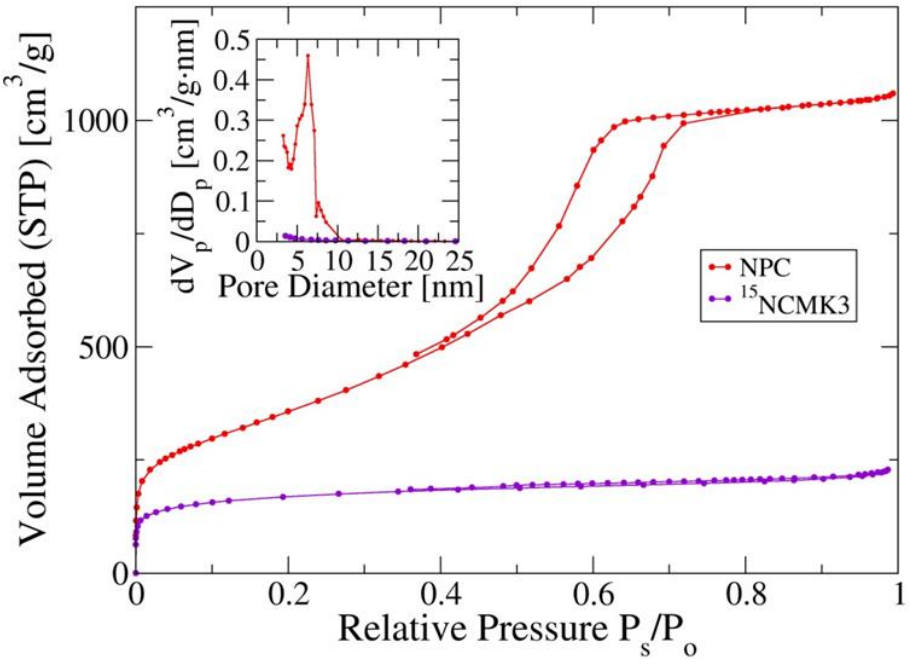

Figure S6. Nitrogen adsorption and desorption isotherms and the pore size distributions (inset) from the BJH (Barrett-Joyner-Halenda) model for NPC and ^{15}NCMK3 carbon scaffolds. Total surface area for the NPC and NCMK3 are 1290 m^2/g and 587 m^2/g respectively. The total pore volumes for the NPC is 1.63 cc/g and NCMK3 is 0.36 cc/g.

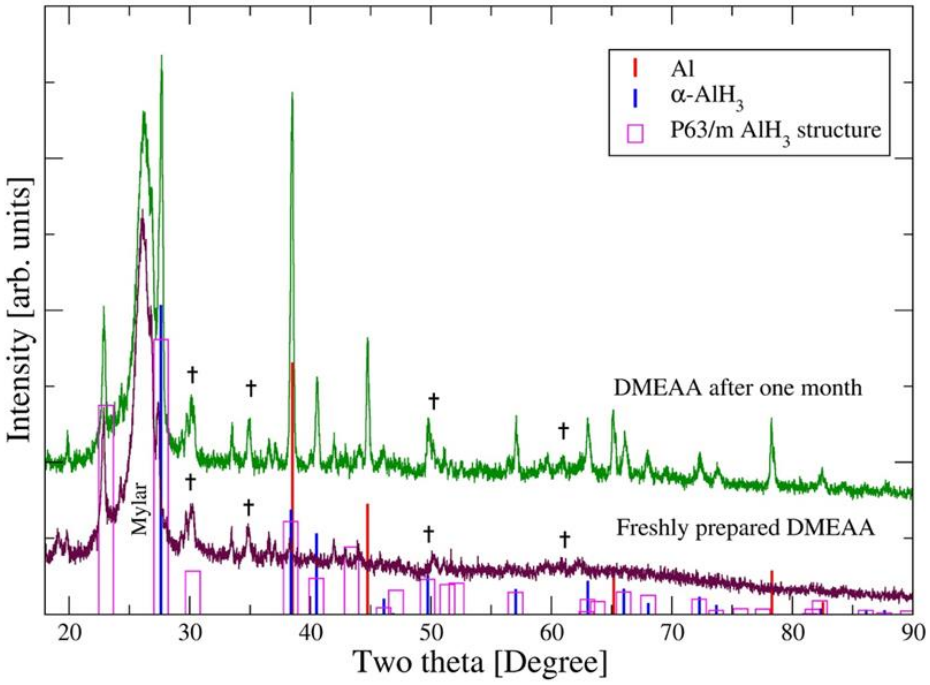

Figure S7. XRD results for the freshly made DMEAA (bottom, maroon) and DMEAA powder after one month stored in the glove box (top, green). The peaks labelled with † are DMEAA peaks. The intensity of the main Brag peak for Alpha alane (two theta = 27.62 degree) and metallic Al (two theta = 38.50 degree) have increased over the time.

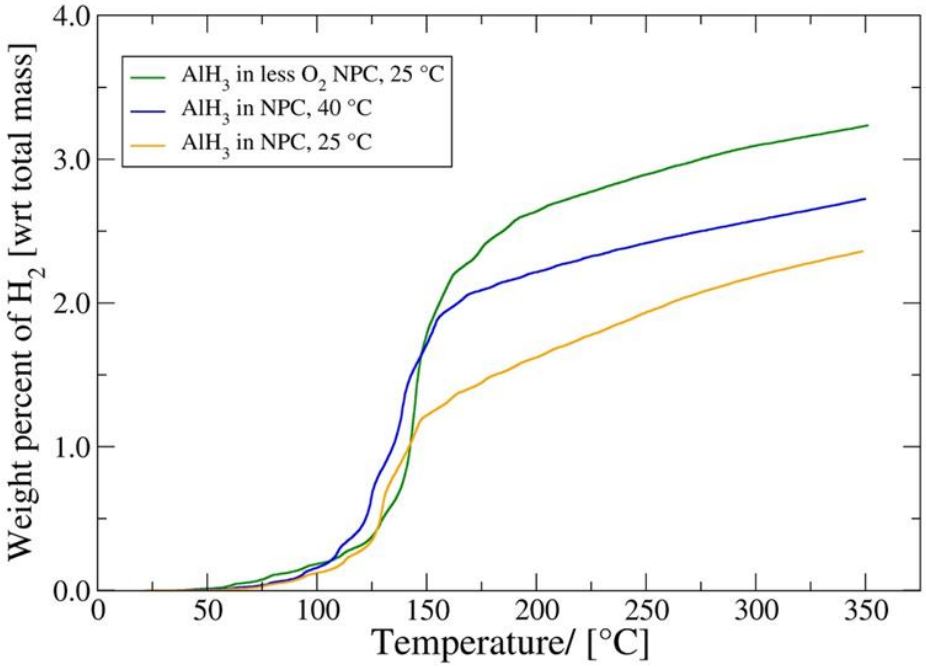

Figure S8. Desorption results of the higher loading samples upto 300 °C. Results indicate the highest hydrogen desorption rate is between 100-150 °C rage for all the samples.

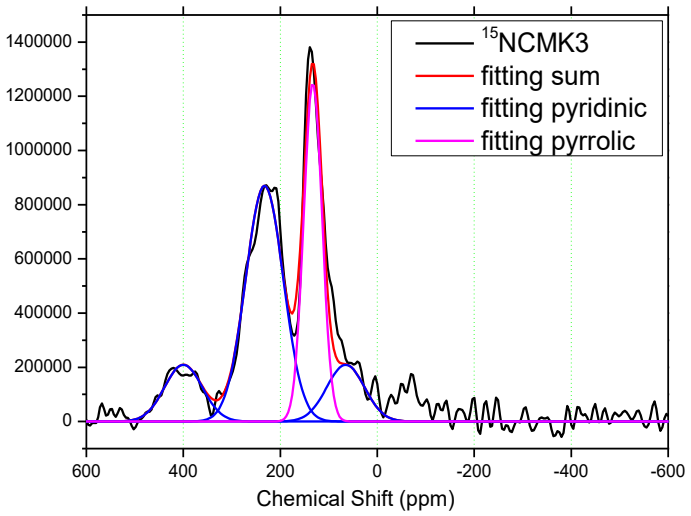

Figure S9. DMFIT for ^{15}N NMR of bare ^{15}NCMK3. Pyridinic nitrogen chemical shift is 231 ppm and pyrrolic nitrogen chemical shift is 133 ppm.

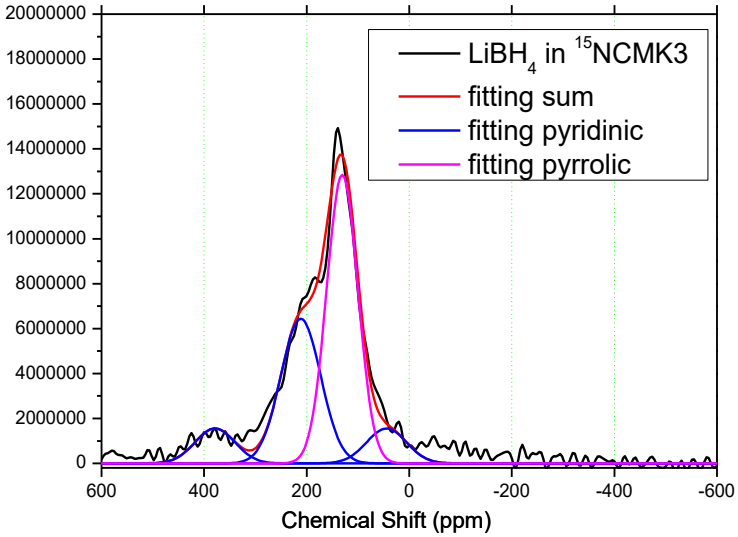

Figure S10: DMFIT for $LiBH_4$ in ^{15}NCMK3. Pyridinic nitrogen chemical shift is 211 ppm and pyrrolic nitrogen chemical shift is 131 ppm.

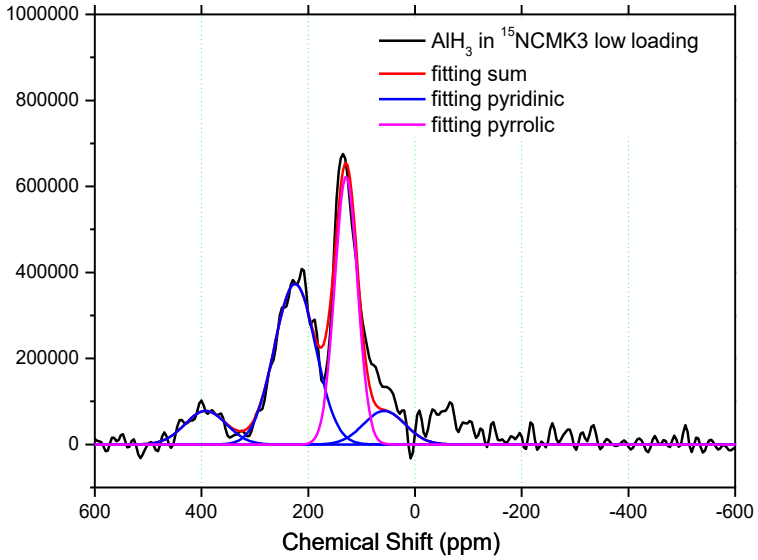

Figure S11. DMFIT for AlH_3 in ^{15}NCMK3 low loading. Pyridinic nitrogen chemical shift is 231 ppm and pyrrolic nitrogen chemical shift is 129 ppm.

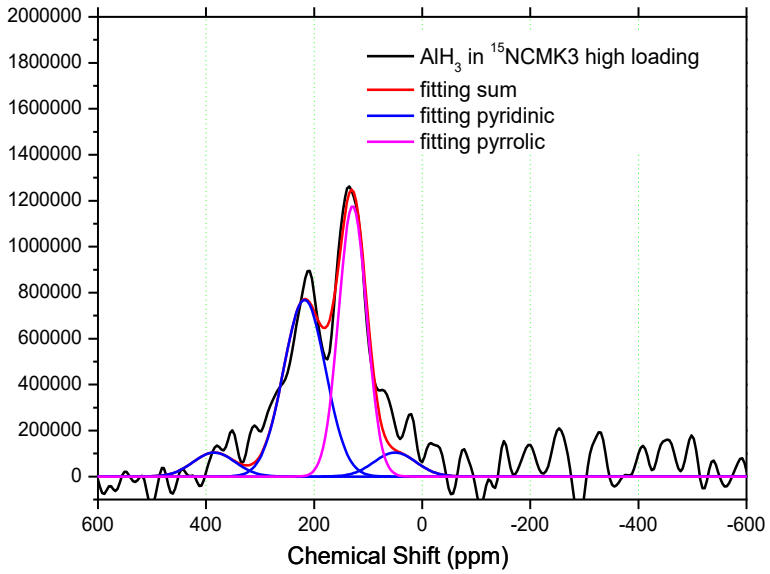

Figure S12. DMFIT for AlH_3 in ^{15}NCMK3 high loading. Pyridinic nitrogen chemical shift is 217 ppm and pyrrolic nitrogen chemical shift is 129 ppm

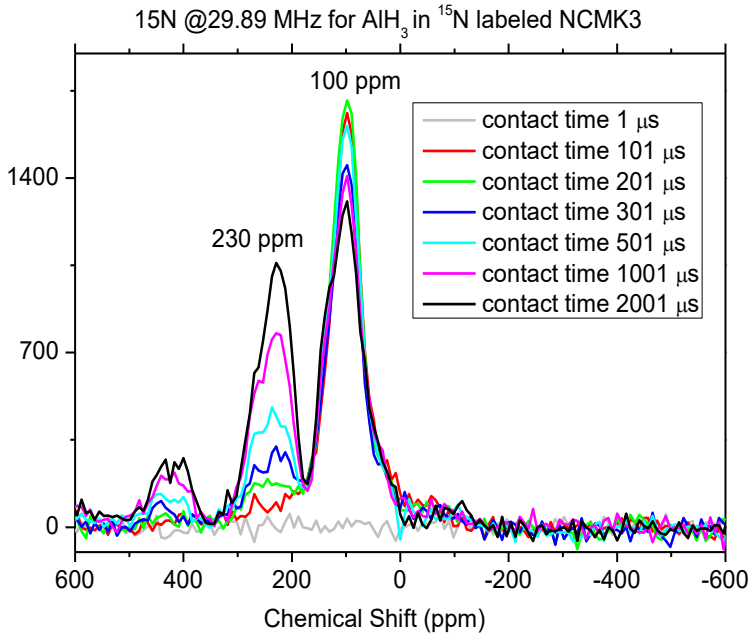

Figure S13. CPMAS (fs=5 kHz) from ^{1}H to ^{15}N for AlH_3 in $^{15}NCMK3$ low loading. The best contact time for pyrrole peak at 100 ppm is 0.2 ms and for pyridine peak at 230 ppm is more than 2 ms. Shorter best contact time means shorter distance between ^{1}H and ^{15}N. Compared with the bare $^{15}NCMK3$, the pyridine peak appears in AlH_3 in $^{15}NCMK3$ low loading sample. This is because there is some left over solvent (toluene) with ^{1}H, and we transfer the polarization from those ^{1}H to the pyridine ^{15}N.

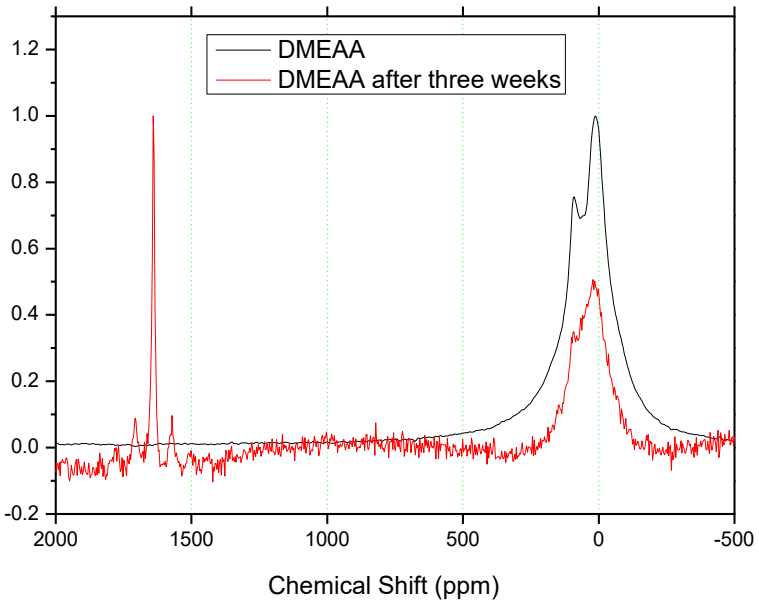

Figure S14. ^{27}Al MAS (f_S = 6 kHz) NMR spectra got using central transition pulse acquire. After three weeks, aluminum metal peak appears.

REFERENCES

1. Zou, H.; Gradišek, A.; Emery, S. B.; Vajo, J. J.; Conradi, M. S. LiBH4 in Aerogel: Ionic Motions by NMR. *J. Phys. Chem. C* **2017**, *121* (28), 15114–15119.

2. Sandrock, G.; Reilly, J.; Graetz, J.; Zhou, W.-M.; Johnson, J.; Wegrzyn, J. Accelerated Thermal Decomposition of AlH3 for Hydrogen-Fueled Vehicles. *Appl. Phys. A* **2005**, *80* (4), 687–690.

3. Carr, C. L.; Majzoub, E. H. Surface-Functionalized Nanoporous Carbons for Kinetically Stabilized Complex Hydrides through Lewis Acid–Lewis Base Chemistry. *J. Phys. Chem. C* **2016**, *120* (21), 11426–11432.

4. Carr, C. L.; Jayawardana, W.; Zou, H.; White, J. L.; El Gabaly, F.; Conradi, M. S.; Stavila, V.; Allendorf, M. D.; Majzoub, E. H. Anomalous H2 Desorption Rate of NaAlH4 Confined in Nitrogen-Doped Nanoporous Carbon Frameworks. *Chem. Mater.* **2018**, *30* (9), 2930–2938.

5. Stavila, V.; Bhakta, R. K.; Alam, T. M.; Majzoub, E. H.; Allendorf, M. D. Reversible Hydrogen Storage by NaAlH4 Confined within a Titanium-Functionalized MOF-74(Mg) Nanoreactor. *ACS Nano* **2012**, *6* (11), 9807–9817.

6. Nielsen, T. K.; Manickam, K.; Hirscher, M.; Besenbacher, F.; Jensen, T. R. Confinement of MgH2 Nanoclusters within Nanoporous Aerogel Scaffold Materials. *ACS Nano* **2009**, *3* (11), 3521–3528.

7. Chen, H.; Cong, T. N.; Yang, W.; Tan, C.; Li, Y.; Ding, Y. Progress in Electrical Energy Storage System: A Critical Review. *Prog. Nat. Sci.* **2009**, *19* (3), 291–312.

8. Liu, X.; Peaslee, D.; Majzoub, E. H. Tailoring the Hydrogen Storage Properties of Li4BN3H10 by Confinement into Highly Ordered Nanoporous Carbon. *J. Mater. Chem. A* **2013**, *1* (12), 3926–3931.

9. General atomic and molecular electronic structure system - Schmidt - 1993 - Journal of Computational Chemistry - Wiley Online Library https://onlinelibrary.wiley.com/doi/abs/10.1002/jcc.540141112 (accessed Sep 19, 2018).

10. Gordon, M. S.; Schmidt, M. W. Chapter 41 - Advances in Electronic Structure Theory: GAMESS a Decade Later. In *Theory and Applications of Computational Chemistry*; Dykstra, C. E., Frenking, G., Kim, K. S., Scuseria, G. E., Eds.; Elsevier: Amsterdam, 2005; pp 1167–1189.

11. Kresse, G.; Hafner, J. Ab Initio Molecular Dynamics for Liquid Metals. *Phys. Rev. B* **1993**, *47* (1), 558–561.

12. Kresse, G.; Furthmüller, J. Efficiency of Ab-Initio Total Energy Calculations for Metals and Semiconductors Using a Plane-Wave Basis Set. *Comput. Mater. Sci.* **1996**, *6* (1), 15–50.

13. Kresse, G.; Furthmüller, J. Efficient Iterative Schemes for Ab Initio Total-Energy Calculations Using a Plane-Wave Basis Set. *Phys. Rev. B* **1996**, *54* (16), 11169–11186.

14. Kresse, G.; Joubert, D. From Ultrasoft Pseudopotentials to the Projector Augmented-Wave Method. *Phys. Rev. B* **1999**, *59* (3), 1758–1775.

15. Blöchl, P. E. Projector Augmented-Wave Method. *Phys. Rev. B* **1994**, *50* (24), 17953–17979.

16. Perdew, J. P.; Burke, K.; Ernzerhof, M. Generalized Gradient Approximation Made Simple. *Phys. Rev. Lett.* **1996**, *77* (18), 3865–3868.

17. Perdew, J. P.; Chevary, J. A.; Vosko, S. H.; Jackson, K. A.; Pederson, M. R.; Singh, D. J.; Fiolhais, C. Atoms, Molecules, Solids, and Surfaces: Applications of the Generalized Gradient Approximation for Exchange and Correlation. *Phys. Rev. B* **1992**, *46* (11), 6671–6687.

18. Monkhorst, H. J.; Pack, J. D. Special Points for Brillouin-Zone Integrations. *Phys. Rev. B* **1976**, *13* (12), 5188–5192.

19. Mason, T.; Majzoub, E. H. Effects of a Carbon Surface Environment on the Decomposition Properties of Nanoparticle LiBH4: A First-Principles Study. *J. Phys. Chem. C* **2014**, *118* (17), 8852–8858.

20. Valencia, F.; Romero, A. H.; Ancilotto, F.; Silvestrelli, P. L. Lithium Adsorption on Graphite from Density Functional Theory Calculations. *J. Phys. Chem. B* **2006**, *110* (30), 14832–14841.

21. Pan, H.; Pruski, M.; Gerstein, B. C.; Li, F.; Lannin, J. S. Local Coordination of Carbon Atoms in Amorphous Carbon. *Phys. Rev. B* **1991**, *44* (13), 6741–6745.

22. Liu, R.; Shi, Y.; Wan, Y.; Meng, Y.; Zhao, D. Triconstituent Co-Assembly to Ordered Mesostructured Polymer- Silica and Carbon- Silica Nanocomposites and Large-Pore Mesoporous Carbons with High Surface Areas. *J. Am. Chem. Soc.* **2006**, *128* (35), 11652–11662.

23. Vinu, A.; Ariga, K.; Mori, T.; Nakanishi, T.; Hishita, S.; Golberg, D.; Bando, Y. Preparation and Characterization of Well-Ordered Hexagonal Mesoporous Carbon Nitride. *Adv. Mater.* **2005**, *17* (13), 1648–1652.

24. Wong, B. M.; Lacina, D.; Nielsen, I. M. B.; Graetz, J.; Allendorf, M. D. Thermochemistry of Alane Complexes for Hydrogen Storage: A Theoretical and Experimental Investigation. *J. Phys. Chem. C* **2011**, *115* (15), 7778–7786.

25. Jun, S.; Joo, S. H.; Ryoo, R.; Kruk, M.; Terasaki, O. Synthesis of New, Nanoporous Carbon with Hexagonally Ordered Mesostructure. *J. Am. Chem. Soc.* **2000**, *122* (43), 10712–10713.

26. Sing, K. S. W. Reporting Physisorption Data for Gas/Solid Systems with Special Reference to the Determination of Surface Area and Porosity (Recommendations 1984). *Pure Appl. Chem.* **1985**, *57* (4), 603–619.

27. Sun, F.; Liu, J.; Chen, H.; Zhang, Z.; Qiao, W.; Long, D.; Ling, L. Nitrogen-Rich Mesoporous Carbons: Highly Efficient, Regenerable Metal-Free Catalysts for Low-Temperature Oxidation of H2S. *ACS Catal.* **2013**, *3* (5), 862–870.

28. Zhao, Z.; Dai, Y.; Lin, J.; Wang, G. Highly-Ordered Mesoporous Carbon Nitride with Ultrahigh Surface Area and Pore Volume as a Superior Dehydrogenation Catalyst. *Chem. Mater.* **2014**, *26* (10), 3151–3161.

29. Brower, F. M.; Matzek, N. E.; Reigler, P. F.; Rinn, H. W.; Roberts, C. B.; Schmidt, D. L.; Snover, J. A.; Terada, K. Preparation and Properties of Aluminum Hydride. *J. Am. Chem. Soc.* **1976**, *98* (9), 2450–2453.

30. Graetz, J.; Reilly, J. J. Thermodynamics of the α,β and γ Polymorphs of AlH3. *J. Alloys Compd.* **2006**, *424* (1), 262–265.

31. Ke, X.; Kuwabara, A.; Tanaka, I. Cubic and Orthorhombic Structures of Aluminum Hydride $\mathrm{Al}{\mathrm{H}}_{3}$ Predicted by a First-Principles Study. *Phys. Rev. B* **2005**, *71* (18), 184107.

32. Graetz, J.; Reilly, J.; Sandrock, G.; Johnson, J.; Zhou, W. M.; Wegrzyn, J. Aluminum Hydride, AlH3, as a Hydrogen Storage Compound. In *Advanced Materials for Energy Conversion III: A Symposium in Honor of Drs Gary Sandrock, Louis Schlapbach, and Seijirau Suda*; **2006**; pp 57–63.

33. Dean, J. A. *Lange's Handbook of Chemistry*, 15th edition.; **1990**.

SECTION

3.INVESTIGATION OF NaAlH4 CONFINED IN NITROGEN FUNCTIONALIZED NANOPOROS CARBON SCAFFOLDS VIA DESORPTION MEASUREMENTS

$NaAlH_4$ is one of the most studied complex metal hydrides for hydrogen energy storage systems. The reversibility of the $NaAlH_4$ was first demonstrated by Bogdanovic et al. in 1997.[33] In this study, the system was doped with few mol % of some Ti compounds to obtain the reversibility.[33] But, these systems were suffered from the inadequate dehydrogenation/rehydrogenation rates, and insufficient cyclic stability and requirement of higher operating temperatures and pressures.[74] As an alternative, nano confined systems were investigated to obtain better hydrogen cycling, desorption properties and reversibility. When the decomposition reaction involves several steps, such as in $NaAlH_4$, nanoconfinement can have a significant impact on the reversibility of the hydrogen release.[75] Although the advantages of combining $NaAlH_4$ with carbon support were first mentioned in a patent application in 2004, first open literature appeared two years later.

Bulk $NaAlH_4$ releases a significant amount of hydrogen at a higher temperature without a catalyst. First, it starts to release small amount of hydrogen upon melting (around 180 °C) and a substantial amount of hydrogen during the decomposition to hexahydride phase (Na_3AlH_6, around 240-250 °C).[60] In one of the studies, Gao et al. showed that, hydrogen can be released in single step instead of multiple steps with low hydrogen releasing

temperature when $NaAlH_4$ confined in 2-3 nm of pores of the carbon. They were also able to obtain reversibility under mild reversibility conditions (24 bar at 150 °C).[60]

A previous study from our group has shown that, $LiBH_4$ can kinetically stabilized using nitrogen functionalized carbons demonstrating a higher activation energy of 30 kJ/mol for the nitrogen doped substrate compared to undoped version. Moreover, in this study they found that the diborane gas release temperature has shifted to a higher temperature value.[61] It is clear that nitrogen functionalization can have a significant effect on the infiltrated metal hydride as evident from the above finding. Even though there are several studies on $NaAlH_4$ with non-doped carbons, effects due the surface functionalization of carbon on the $NaAlH_4$ have not been investigated before. In this section, we investigate the desorption measurements for nitrogen doped carbon substrate and compare them with the undoped version with the similar geometry. Full published paper containing this section is included in the appendix.

3.1. EXPERIMENTAL

Four different types of carbons were synthesized according to previous literature. Carbons made with hard templating method were named as CMK3 and NCMK3 and carbons made with organic-inorganic self-assembly soft templating method were named as NPC and NNPC. Detailed descriptions of the synthesis methods for these nanoporous carbons were described in chapter 2. Nitrogen functionalized scaffolds were named as NCMK3 (nitrogen doped CMK3) and NNPC (nitrogen doped NPC).

Nitrogen adsorption desorption characterizations for the carbon samples were also explained in the chapter 2. Purified $NaAlH_4$ was used for the infiltration procedures. First,

$NaAlH_4$ was mixed with dried carbon using mortar and pestle for about 15 min. These mixtures were made to yield 20 wt % $NaAlH_4$ w.r.t total mass of the sample. Then, the mixture was packed into a Sievert type apparatus and was pressurized the system at room temperature using a high-pressure hydrogen tank. Melt infiltration carried out at two different hydrogen excess pressure values (200 bar and 350 bar) to investigate the decomposition behavior of the $NaAlH_4$ system. 200 bar infiltration was carried out in UMSL and 350 bar infiltration was carried out in Sandia National Lab, Livermore. For the $NaAlH_4$ infiltration at 200 bar, the same system described in the chapter 2 was used. For the $NaAlH_4$ infiltration at 350 bar, a similar type of custom built Sievert apparatus set up was used together with a heating tape. In this procedure, first sample was packed and pressurized using a compressed hydrogen gas tank up to 180 bar. Then, the sample holder was immersed in the liquid nitrogen bath until the system became 77 K. After that, sample holder was pressurized again and let it to heat up to room temperature. The final pressure of the system was obtained from applying the ideal gas law. Finally, sample was heated to 200 °C and dwelled at this temperature for 1 hour period and was cooled back to room temperature under high hydrogen pressure.

Desorption measurements were performed using the same previously described (chapter 2) Sievert type apparatus set up with 4 °C/min rate to 300 °C. These desorbed samples were previously desorbed and rehydrided two times. The rehydriding processes was performed under 180 bar of excess hydrogen pressure and 150 °C for 15 hours.

3.2. RESULTS AND DISCUSSION

Porosimetry measurements were performed to characterize the synthesized carbon samples. Nitrogen adsorption desorption isotherms and the pore size distributions (inset) are shown in the Figure 3.1. A summary of the porosimetry results are shown in the Table 3.1.

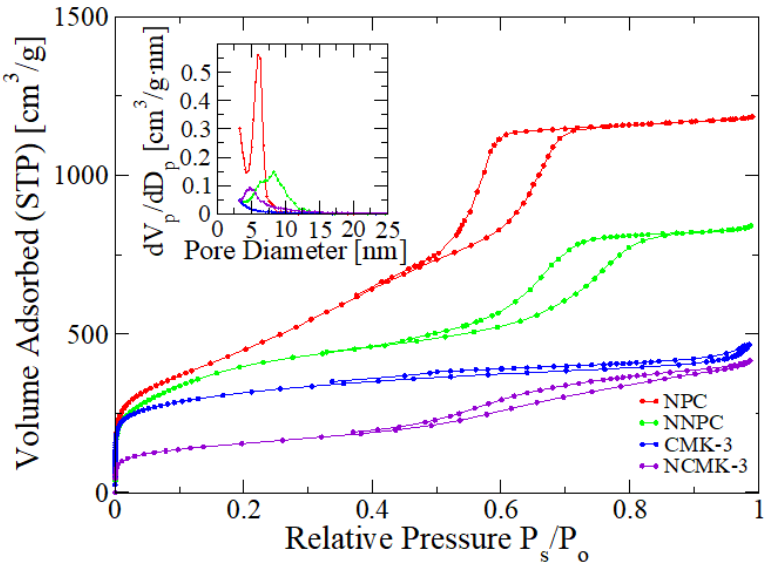

Figure 3.1. Nitrogen adsorption desorption isotherms and the pore size distributions (inset) measured at 77K. The NPC and NNPC isotherms have been shifted up 200 and 150 cm^3/g, respectively, for clarity.

All of the carbon display type IV isotherms indicating both mesoporous and microporous behavior according to Figure 1. During the adsorprion process, first, monolayer forms with the filling of micropores followed by the multi-layer adsorption in the lower relative pressure region. The hysteresis is generally representing sample mesoporosity. The relative pressure value for the sharp adsorb volume increase due to capillary condensation is higher for NPC type carbons compared to CMK3 type carbons.

This denotes higher pore sizes for NPC type carbons as evident from the inset pore size distributions. The hysteresis loop in NPC/NNPC is closer to H2 type hysteresis loop suggesting cylindrical nanopore channels in a 2D hexagonal arrangement. Based on the precursor material (SBA-15), CMK3 type has the inverse geometry of NPC, with carbon rods in the hexagonal symmetry. According to the isotherm, CMK3/NCMK3 has H1 type hysteresis loop suggesting more slit like structure pores. Total pore volumes and surface areas for NPC type carbon is significantly large compared to CMK3 type.

Table 3.1. Summary of Nitrogen adsorption desorption measurements.

Sample	Pore size[a,b] [nm]	S^{c}_{BET} [m^2/g]	V_T^{d} [cm^3/g]
NPC	6.0	1290	1.63
NNPC	7.5	1426	1.30
CMK3	3.5	1073	1.08
NCMK3	3.0	764	0.84

[a] Average pore diameter. [b] Calculated by the BJH mentioned using adsorption branch isotherm data. [c] Calculated using the BET method in a relative pressure range of 0.05 to 0.02. [d] Total pore volume: estimated from the amount adsorbed at a relative pressure (P_s/P_0) of 0.99.

PXRD scans are shown in Figure 3.2 for the infiltrated scaffolds. The absence of any $NaAlH_4$ peaks after infiltration confirms the successful infiltration indicating there is

little or no $NaAlH_4$ present outside the pores. Even though these measurements were performed above the equilibrium pressure (128 bar at 184 °C for bulk $NaAlH_4$[76]), decomposition of metallic Al can be observed. The same behavior was observed with separate set of samples infiltrated at 350 bar as shown in the Figure 3.3. This indicates the decomposition cannot be avoided from the increasing infiltration pressure. The decomposition may occur as a part of initial the substrate wetting. No Na_3AlH_6 was observed in the XRD for all types of substrates. The result agrees with the previous studied melt infiltrated $NaAlH_4$/carbon systems.[58–60]

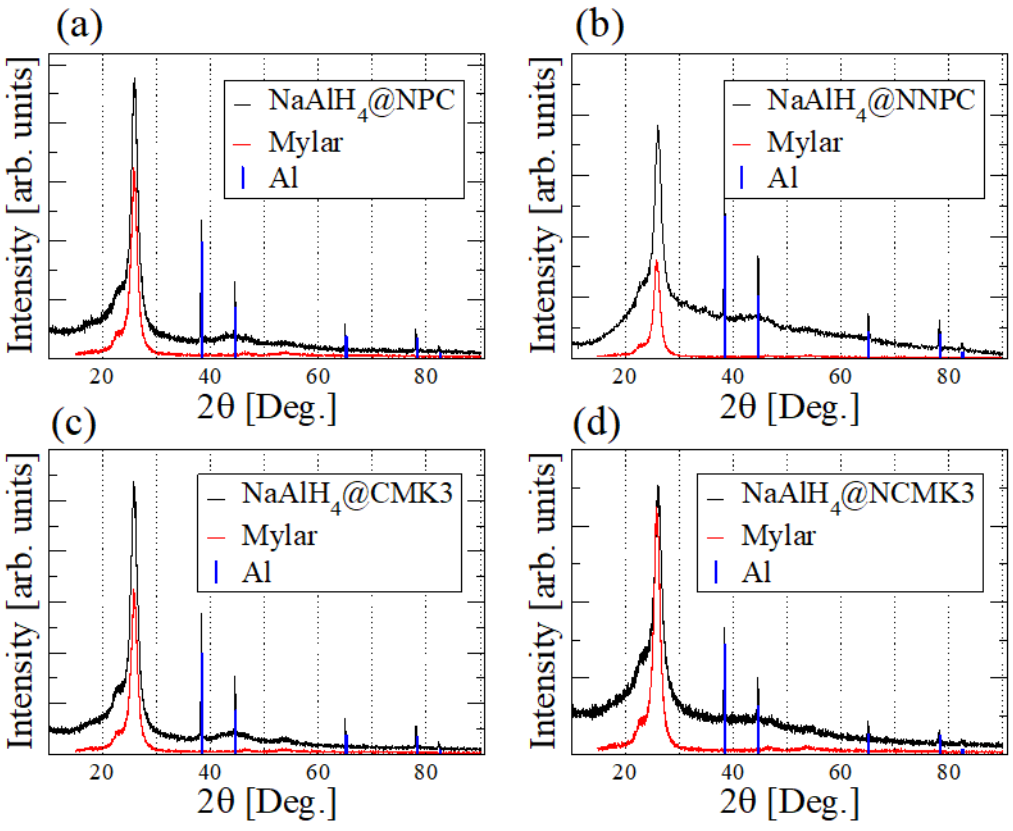

Figure 3.2. PXRD scans for samples infiltrated at 200 bar excess hydrogen pressure.

Third H_2 desorption cycle from room temperature to 300 °C at a ramp rate of 4 °C/min is shown in the Figure 3.4. The weight percent numbers in each of the sample has been normalized to the initial $NaAlH_4$ mass. The weight percent number is indicated a lower bound for each of the sample due to the observed decomposition of $NaAlH_4$ upon infiltration. According to results, all four of infiltrated $NaAlH_4$ systems show reversibility even in the third cycle.

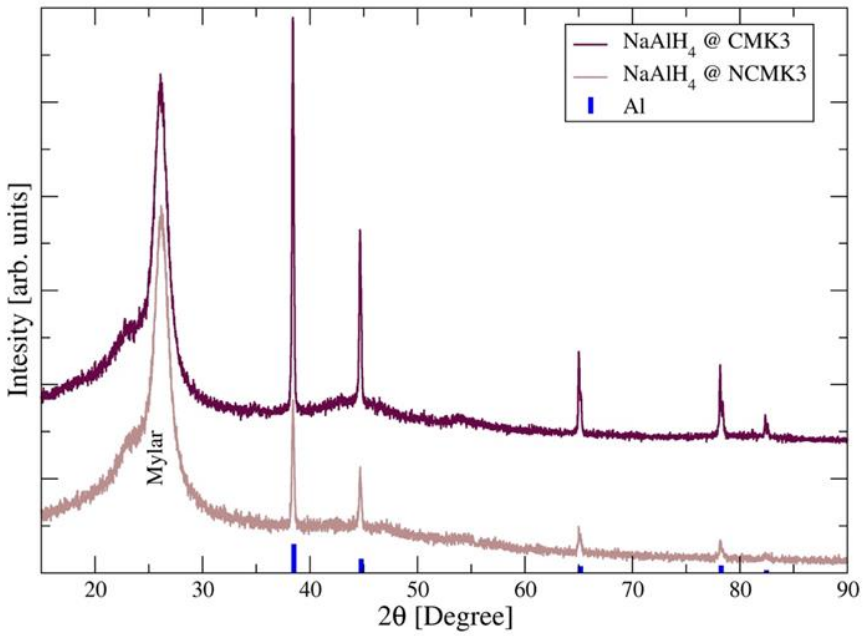

Figure 3.3. PXRD results for $NaAlH_4$ infiltrated carbons at 350 bar.

Non-nitrogen functionalized carbons have a higher reversible capacity (~ 3 wt %) compared to nitrogen functionalized carbons (~1 wt %). Clearly, nitrogen doped systems do not start to desorb large quantities of hydrogen until much higher temperature. Moreover, higher hydrogen rates can be seen for non-functionalized carbons.

The lowering of desorption temperature for nano confined $NaAlH_4$ systems relative to bulk have been observed before.[58–60,77,78] Non-functionalized carbons have shown similar results with the higher maximum hydrogen rates lower than 180 °C. However, the results for higher desorption temperatures for $NaAlH_4$ confined in nitrogen-functionalized scaffolds is surprising. The mechanism accountable for this behavior may be due to interactions between the hydride and the host surface. Some of the possible reasons are as follows. The transition of $NaAlH_4$ from the solid to liquid phase occur in the presence of nitrogen atoms for nitrogen functionalized carbons. Due to the decomposition of $NaAlH_4$, some Na ions can be intercalated into the framework. The intercalation of Na ions can increase the electron density in the scaffolds. The nitrogen doped carbon scaffolds already have increased electron density near the nitrogen hetero atom. So, the intercalation of Na atom can behave differently in the nitrogen doped carbons. These electron density changes in the scaffold may also lead to change desorption kinetics.

3.3. SECTION CONCLUSION

In this work, two different types of nanoporous carbons, both with and without nitrogen functionalization were used as porous substrates to melt infiltrate $NaAlH_4$. After the infiltration, systems were investigated using PXRD and desorption measurements. All the carbon samples used in the study composed of mesopores as well as micropores according to porosimetry results. No crystalline $NaAlH_4$ peaks were detected from PXRD for the infiltrated samples indicating the intact $NaAlH_4$ is amorphous and inside the pores of the scaffold. Decomposition of $NaAlH_4$ to metallic Al was observed even in the

samples made under very high-pressure conditions (~350 bar). All the infiltrated samples displayed reversibility in the third desorption cycle. Hydrogen desorption in the nitrogen functionalized carbons was delayed compared to the non-functionalized carbons. This is due to the surface interactions of $NaAlH_4$ and the hetero atom nitrogen in the carbon scaffold during desorption process.

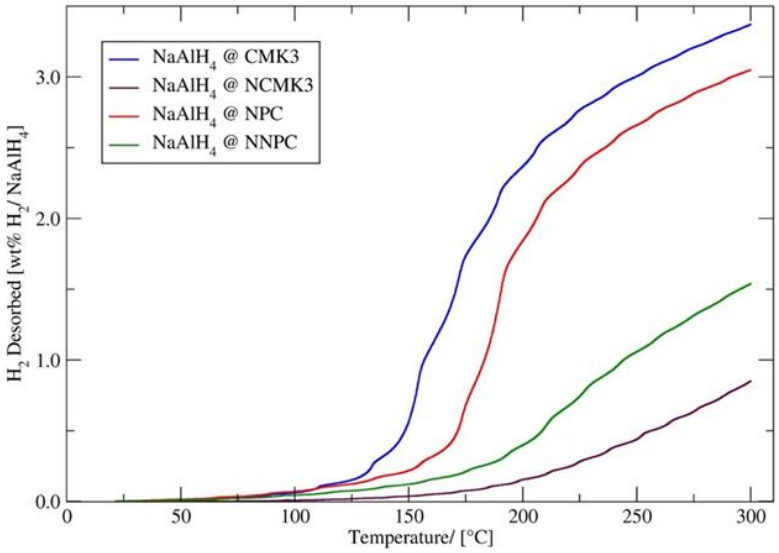

Figure 3.4. Desorption results for the $NaAlH_4$ infiltrated carbon

4. CONCLUSIONS

In this work, different types of mesoporous carbons were studied for energy storage applications. All the synthesized carbons composed with well ordered structures. Two different techniques, namely hard templating method and soft templating method were employed to obtain these carbon types. CMK3 type carbons were produced with slit like pores with the inverse replica of SBA-15 hard template structure. NPC type carbons were produced from soft templating technique with cylindrical pores arranged in 2D hexagonal symmetry. The addition of silicate into the soft templating technique (organic-inorganic self-assembly method) gives higher pore volumes and higher surface areas compared to the regular soft templating method (organic-organic self-assembly method). The nitrogen functionalization can introduce four different nitrogen environments to the scaffold namely pyridinic, pyrollic, graphitic, and oxidized nitrogens. Higher nitrogen doping can be obtained for NCMK3 carbon compared to NNPC carbon.

Diffusion coefficients for the pure forms of mesoporous carbon types were analyzed from a traditional Galvanostatic Intermittent Titration Technique (GITT) and a newly developed diffusion method named Voltage-relaxation Galvanostatic Intermittent Titration Technique (VR- GITT). Diffusion coefficients obtained from both methods show a good agreement and lie in the range of previously reported hard carbon diffusion coefficients. VR- GITT can also be used to obtain information on the geometry related or microstructural features of the sample. More importantly, the method is applicable along a flat voltage plateau.

Higher and lower doping alane infiltrated samples were investigated. Infiltration of lower loading samples were not successful as it reacts with the oxygen containing groups on the substrate upon infiltration. Higher loading alanes were successfully infiltrated even though, there were some DMEAA powder detected outside of the pores. Baked DMEAA solvent exhibits two different alane phases namely alpha and p63m phase. Reduced oxygen carbons infiltrated with alane show the highest desorption hydrogen wt % indicating that a higher amount of alane could be inside this sample compared to the other infiltrated samples. Synthesis temperature and the amount of the oxygen on the carbon have a great influence on the final infiltrated product. Moreover, interactions were observed for alane and $LiBH_4$ infiltrated into ^{15}NCMK3 carbon using NMR studies. Clearly, our results show evidence of interacting Al and B with the pyridinic nitrogen on the scaffold.

$NaAlH_4$ infiltrated into carbons with and without nitrogen functionalization were examined from the desorption measurements. Higher reversibility for non-functionalized carbons was observed relative to nitrogen doped carbons. Moreover, hydrogen desorption of nitrogen doped carbons has shifted to a higher temperature with respect to their non-doped version of carbon substrate. This significant shift is due to the surface interactions between the hydride and the nitrogen atoms present in the substrate.

APPENDIX

ANOMALOUS H_2 DESORPTION RATE OF $NaAlH_4$ CONFINED IN NITROGEN-DOPED NANOPOROUS CARBON FRAMEWORKS.

Christopher L. Carr,[†] Waruni Jayawardana,[†] Hongyang Zou,[§] James L. White,[‖] Farid El Gabaly,[‖] Mark S. Conradi[§,£], Vitalie Stavila,[‖] Mark D. Allendorf,[‖] and Eric H. Majzoub[†,‡,*]

[†]Center for Nanoscience and Department of Physics and Astronomy, [‡]Department of Chemistry and Biochemistry, University of Missouri-Saint Louis, One University Boulevard, Saint Louis, Missouri 63121, United States

[§]Department of Physics, Washington University, One Brookings Drive, Saint Louis, Missouri 63130, United States

[‖]Sandia National Laboratories, Livermore, California 94550, United States

[£]ABQMR Inc., Albuquerque, NM 87106, United States

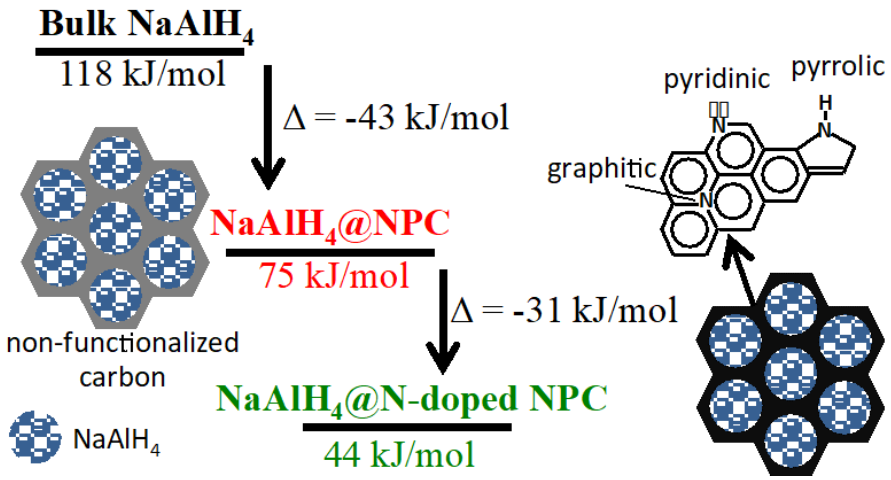

ABSTRACT

Confining $NaAlH_4$ in nanoporous carbon scaffolds is known to alter the sorption kinetics and/or pathways of the characteristic bulk hydriding reactions through interaction with the framework at the interface, the increased specific surface area of the resulting nanoparticles, decreased hydrogen diffusion distances, and prevention of phase segregation. Although the nano-size effects have been well studied, the influence of the carbon scaffold surface chemistry remains unclear. Here we compare the hydrogen sorption characteristics of $NaAlH_4$ confined by melt infiltration in nitrogen-doped/undoped ordered nanoporous carbon of two different geometries. ^{23}Na and ^{27}Al MAS NMR, N_2 sorption, and PXRD verify $NaAlH_4$ was successfully confined and remains intact in the carbon nanopores after infiltration. Both the N-doped/undoped nano-confined systems demonstrate improved reversibility in relation to the bulk hydride during hydrogen desorption/absorption cycling. Isothermal kinetic measurements indicate a lowering of the activation energy for H_2 desorption by as much as 70 kJ/mol in N-doped frameworks, far larger than the reduction in carbon-only frameworks. Most interestingly, this dramatic lowering of the activation energy is accompanied by an unexpected and anomalously low $NaAlH_4$ desorption rate in the N-doped frameworks. This suggests that the framework surface chemistry plays an important role in the desorption process and that the rate limiting step for desorption may be associated with interactions of the hydride and host surface. Our results indicate that functionalization of carbon scaffold surface chemistry with heteroatoms provides a powerful method of altering the characteristic hydrogen sorption properties of confined metal hydride

systems. This technique may prove beneficial in the path to a viable metal hydride-hydrogen storage system.

1. INTRODUCTION

In recent years, confining metal hydrides within porous scaffolds has been established as a useful method of favorably modifying the hydrogen sorption characteristics of the hydride relative to the bulk material. Studies of confined metal hydrides have reported enhanced desorption kinetics,[1-10] improved reversibility,[1,3,4,5,8-10] and, in some instances, altered system thermodynamics.[5] Despite these improvements and extensive search efforts to identify an ideal material, no complex metal hydride systems have been identified that meet all the DOE specifications for onboard hydrogen storage applications.[11] In general, of the complex metal hydrides available, the enthalpy of hydrogen desorption ($\Delta H°$) is either too high (e.g., $LiBH_4$) or too low (e.g., AlH_3) to provide adequate hydrogen pressures (~1–10 bar) for proton exchange membrane fuel cells (PEMFC) operating at a temperature of roughly 80 °C and/or the hydride is not reversible under modest conditions.

Porous substrates are able to alter hydrogen cycling of confined hydrides by utilizing the large surface-area-to-volume ratio and shifting the surface/interface energies facilitated by the scaffolds. Studies of $LiBH_4$ confined in nanoporous carbon (NPC) have indicated that, during melt infiltration of $LiBH_4$ into the scaffold, the interaction of the molten hydride with the scaffold inadvertently dopes the carbon surface with boron, resulting in a favorable energy for $LiBH_4$ to wet the carbon nanopores.[12] Additionally, neutron scattering and NMR studies of $LiBH_4$ confined within nanoporous carbon and

silica scaffolds found that the layer of confined hydride in closest proximity to the pore walls of the scaffolds exhibited rapid reorientations[13-15] or enhanced translational diffusion[16-17] of BH_4^- anions compared to a more bulk-like slower population at the pore interior, suggesting the scaffold must alter the local potential of the anions through either induced lattice strain or electronic effects due to the chemical makeup of the scaffold.

The role of the scaffold chemistry in altering the observed hydrogen sorption properties of the confined metal hydride is less clear. Until recently, there has not been much work aimed at specifically investigating the chemical aspect of the scaffold's influence.[15,18] A study by our group indicated that functionalizing the surface of a nanoporous carbon scaffold with nitrogen heteroatoms can stabilize $LiBH_4$ kinetically, increasing the activation energy for hydrogen desorption by ~30 kJ/mol H_2 in relation to a comparative non-functionalized carbon scaffold.[18] Moreover, Suwarno and co-workers[16] studied the influence of scaffold chemistry by confining $LiBH_4$ in carbon and silica scaffolds of similar pore size, showing the $LiBH_4$ confined in the silica scaffold exhibited a thicker layer of non-bulk like $LiBH_4$ at the scaffold/hydride interface and a larger depression of the solid-solid phase transition than the carbon based system, together indicating that the chemical nature of the scaffold plays an important role in confined hydride systems.

Here we report on the modified hydrogen storage properties observed for $NaAlH_4$ confined in nanoporous carbon surface functionalized with nitrogen heteroatoms with respect to a similar non-functionalized system. Since the initial work by Bogdanovic et al. describing the use of $NaAlH_4$ as a hydrogen storage medium,[19] $NaAlH_4$ has been perhaps the most studied complex metal hydride. Considerable attention has been focused

on $NaAlH_4$ confined in nanoporous scaffolds. For this reason, $NaAlH_4$ naturally presents itself as an ideal system to test the effect that modifying nanoporous carbon surface chemistry has on the hydrogen storage properties of confined $NaAlH_4$ compared to a base non-functionalized system that is relatively well studied. In the present work, matched pairs of nitrogen functionalized/non-functionalized carbon scaffolds of two different geometries were used. Our results indicate the activation energy for hydrogen desorption is lowered by more than ~20 kJ/mol H_2 in the nitrogen functionalized systems of both geometries. Despite the lowered activation energies for hydrogen desorption, an anomalous hydrogen desorption bottleneck occurs for the nitrogen-functionalized systems in the high temperature region, indicating that the presence of nitrogen may restrict the formation of H_2 at the hydride/scaffold interface in this region.

2. EXPERIMENTAL SECTION

Chemicals/Materials*:*_$NaAlH_4$ (93%), pentane, and THF were purchased from Sigma Aldrich. Nanoporous carbon (NPC), nitrogen-doped nanoporous carbon (NNPC), CMK-3 type porous carbon, and nitrogen doped CMK-3 (NCMK-3) were synthesized using published literature methods.[20-23] Detailed synthesis procedures are provided in the Supporting Information.

$NaAlH_4$ Purification: Before use, 7.5 g of the as-received $NaAlH_4$ was dissolved in 400 mL of freshly dried/distilled THF. After stirring for 4 hours the insoluble impurities were allowed to precipitate from the solution. The supernatant was transferred to a separate flask, where the solution was concentrated to a volume of ~125 mL under vacuum. Under stirring 375 mL of dried/distilled pentane was added to the solution,

separating $NaAlH_4$ from the solution as a fine precipitate. After removal of the supernatant $NaAlH_4$ was washed using ~100 mL of dried/distilled pentane. $NaAlH_4$ in the form of a fine white powder was obtained after drying under vacuum. All operations were carried out using Schlenk line techniques.

Melt Infiltration of $NaAlH_4$ into Carbon Scaffolds: The synthesized carbon scaffolds were infiltrated with $NaAlH_4$ using a custom-built Sieverts-type apparatus. The system consists of a cylindrical stainless-steel sample holder (Setaram) equipped with a manual valve allowing samples to be loaded in an argon filled glovebox (O_2 < 1 ppm) and transported to the apparatus without air exposure. The system manifold consists of calibrated volumes of different capacities, with connection ports for vacuum, H_2, and He gas. Manifold pressures are monitored with two calibrated pressure transducers (MKS model 870B). Sample and manifold temperatures were monitored using type K thermocouples. Pressures and temperatures were recorded with data acquisition software on an interfaced computer. Samples are heated using a cylindrical resistive heating element that fits around the outside of the sample holder connected to a PID controller. The sample holder/heating element is wrapped in an insulating glass fiber blanket to minimize heat flow to the surrounding environment during the heating process.

Prior to infiltration the substrate materials were dried under dynamic vacuum overnight at 300 °C. Samples were prepared by mixing $NaAlH_4$ in proportion with the respective carbon scaffold to produce a 20 wt% $NaAlH_4$ physical mixture (1.5 wt% H_2 w.r.t. the total sample mass). Mixing was carried out with a mortar and pestle for 10 minutes, followed by loading into an Al foil roll and placing into a stainless-steel sample holder equipped with a manual valve. All sample handling was performed in an argon-

filled glovebox (O_2 < 1 ppm). Samples were transported to the Sieverts apparatus without air exposure, where they were placed under 190 bar H_2 pressure and heated to 200 °C (~15 °C above the melting point of $NaAlH_4$), reaching a final pressure of 205 bar. Following a dwell period of 45 minutes at 200 °C, the samples were allowed to cool under pressure.

Hydrogen Cycling/Kinetics Measurements: Using the described Sieverts apparatus, Isothermal kinetics measurements and Arrhenius analyses were performed on the four composite samples to determine the activation energies of hydrogen desorption. The hydrogen evolution rates were recorded under isothermal conditions in temperature increments of ~10 °C. From room temperature the samples were heated initially to a temperature of 100 °C at an average ramp rate of 20 °C /min using the previously described PID controlled heating element, where the system was briefly evacuated (P < 1.5 X 10^{-3} MPa). As the samples evolved hydrogen during a 5 minute dwell period into the evacuated static vacuum of the Sieverts apparatus, the pressure within the volume was recorded as a function of time. Deviations of the temperature from the desired setpoint during the dwell period were < 1 °C. At the end of the dwell period the samples were heated to the next setpoint at an average ramp rate of 8 °C/min and the process repeated. At each respective temperature, the rate was determined from the change in pressure. Pressure changes with respect to time exhibited linear behavior over the measured time period, with correlation coefficients exceeding 0.98. The rate of hydrogen desorption can be related to the temperature of the sample through the Arrhenius equation:

$$\text{Rate} = \frac{d[H_2]}{dt} = K_0 e^{-\frac{E_A}{RT}} \quad (1)$$

where K_0 is the pre-exponential rate constant or frequency factor, E_A is the activation energy, and $[H_2]$ is the concentration of hydrogen. In the form presented, the equation describes the temperature dependence of the H_2 desorption rate for a single step process. Following the isothermal kinetics measurements the samples were heated to 250 °C from the final measurement temperature at a ramp rate of 4 °C/min and held at temperature until desorption ceased (~1 hour). Sample rehydriding was carried out at 150 °C under 180 bar H_2 for 15 hours. To ensure repeatability the isothermal kinetics measurements were repeated a second time using the rehydrided samples. After a second rehydriding cycle, desorption of hydrogen from the composite samples into a carefully measured static volume was recorded at a linear ramp rate of 4 °C/min up to 300 °C.

Characterization Measurements: N_2 sorption isotherms were recorded using a SA3100 (Coulter) analyzer at 77 K. Before analysis, the bare carbon samples were outgassed at 300 °C for 10 hours and the infiltrated carbon samples outgassed at 40 °C for 30 minutes. Samples were loaded into glass analysis vessels in an argon filled glovebox (O_2 < 1 ppm) and transported to the analyzer without air exposure. The specific surface area S_{BET} was calculated using the Brunauer-Emmett-Teller (BET) method in a relative pressure range of 0.05 to 0.2. Pore size distributions and total pore volume were calculated using the Barrett, Joyner, and Halenda (BJH) calculation model using data from the adsorption isotherm. The total pore volume was estimated by the amount adsorbed at a relative pressure (P_s/P_0) of .99. Powder X-ray diffraction (PXRD) measurements were acquired using a Rigaku Ultima IV X-ray diffractometer with a Cu

K_α radiation source. Samples containing hydrides were sealed using Mylar film in an argon filled glovebox (O_2 < 1 ppm) to prevent air exposure during measurements. For nuclear magnetic resonance (NMR) studies, samples were packed into 5 mm OD pencil rotors inside an argon glove box (O_2 < 1 ppm). The packed rotors were transported without air exposure. N_2 gas boil-off from a liquid nitrogen dewar supplied pure N_2 gas for the bearing and drive gas needed to spin the rotors, thus inhibiting air-related degradation of the samples. Magic angle spinning (MAS) NMR measurements were performed using a home-built spectrometer and Chemagnetics probe on a 7.04 T superconducting magnet. All MAS measurements were made at room temperature with a spinning frequency, f_S, of 5 kHz. X-ray photoelectron spectroscopy (XPS) was performed under UHV conditions (residual pressure better than 1×10^{-8} Torr) using a Physical Electronics 10-360 electron energy analyzer and an Omicron DAR400 Al K-alpha (photon energy = 1487 eV) or Mg K-alpha (photon energy = 1254 eV) X-ray source. Dried samples were embedded in a piece of indium foil to avoid ambiguous quantitation from a carbon support. All XPS peaks were baseline corrected using a Shirley background, and synthetic peaks of mixed Gaussian-Lorentzian (70%/30%) line-shape were used to fit the spectra. Spectra were calibrated to the main C 1s peak at 284.5 eV.

3. RESULTS

Characterization of $NaAlH_4$ in Nanoporous Carbon Frameworks. In this work, nitrogen functionalized and non-functionalized carbon scaffolds of two different geometries were employed: (1) ordered mesoporous carbon (CMK-3, NCMK-3) type carbon produced via the nano-casting method using a SBA-15 silica template[22,23] and (2)

nanoporous carbon (NPC, NNPC) synthesized by the organic-inorganic evaporation induced self assembly method,[20,21] resulting in carbon consisting of cylindrical nanopore channels in a 2D hexagonal arrangement displaying P6m symmetry. Similarly, the SBA-15 silica template contains cylindrical mesopore channels in the P6m symmetry as well, with an additional network of smaller disordered micro channels connecting the main mesopores. Nano-casting results in carbon scaffolds with an inverse geometry of the SBA-15 template, consisting of ordered cylindrical nano-rods in P6m symmetry held in place by nano-fibrils formed from the disordered micropore array interconnecting the SBA-15 mesopores. Since the SBA-15 and NPC share a common geometry and symmetry of their main pore channels, CMK-3 is inverse to NPC as well, with the voids between the rods, somewhat slit-like in nature, acting as the mesopores of the CMK-3 type carbon.

Figure 1 displays the isotherms and pore distributions (inset) obtained from nitrogen sorption measurements of the prepared carbon scaffolds at 77 K. All of the scaffolds exhibit type IV isotherms, in addition to hysteresis, indicative of the existence of mesoporosity.[24] As adsorption proceeds in the low relative pressure region, the micropores are filled with adsorbate following monolayer and some multi-layer adsorption. In Figure 1 this corresponds roughly to the region where $P_s/P_0 < 0.1$. The increase in relative pressure in the region above 0.1 to the start of each sample's respective hysteresis loop can be mostly attributed to multilayer adsorption along the mesopore walls preceding capillary condensation. Hysteresis is generally indicative of sample mesoporosity,[24] with the loop onset shape relating to the size and shape of the mesopores. Onset of capillary condensation corresponding to the sharp increase in

adsorbed volume on the adsorption branch of the isotherm occurs at a relative pressure of ~0.4 in the NCMK-3/CMK-3 carbons. In contrast, the NNPC/NPC carbons display a sharp adsorbed volume increase at slightly higher relative pressures in the range 0.45-0.5, an indication of slightly larger mesopores. According to the IUPAC classifications,[24] the NNPC/NPC carbons most closely resemble type H_2 hysteresis loops, though the parallel arrangement of the adsorption/desorption isotherms over a considerable pressure range is a feature of type H1 loops. These features together suggest an ordered array of mesopores with a small distribution of sizes, and slight deviations from an idealized cylindrical mesopore as noted in SBA-15.[24-26] On the other hand, the CMK-3 type scaffolds have a hysteresis loop containing features of multiple classifications,[24] which is not surprising considering the reported structure of these materials.[22] The results suggest an ordered array of mesopores, containing sections that are more slit-like in nature.

Pore size distributions calculated using the BJH model are displayed in the inset of Figure 1. NPC and NNPC have average mesopore diameters of 6 and 7.5 nm respectively, with an indication of a micropore distribution below 3 nm as a result of removing silicate oligomers from the mesopore walls during HF etching following carbonization. The largest contribution to the pore volume in the CMK-3 and NCMK-3 scaffolds appears to be from pores $\leq$ 3.5 nm. Table 1 lists the average pore size diameter, surface area (S_{BET}), and total pore volume (V_T) obtained for the carbon scaffolds.

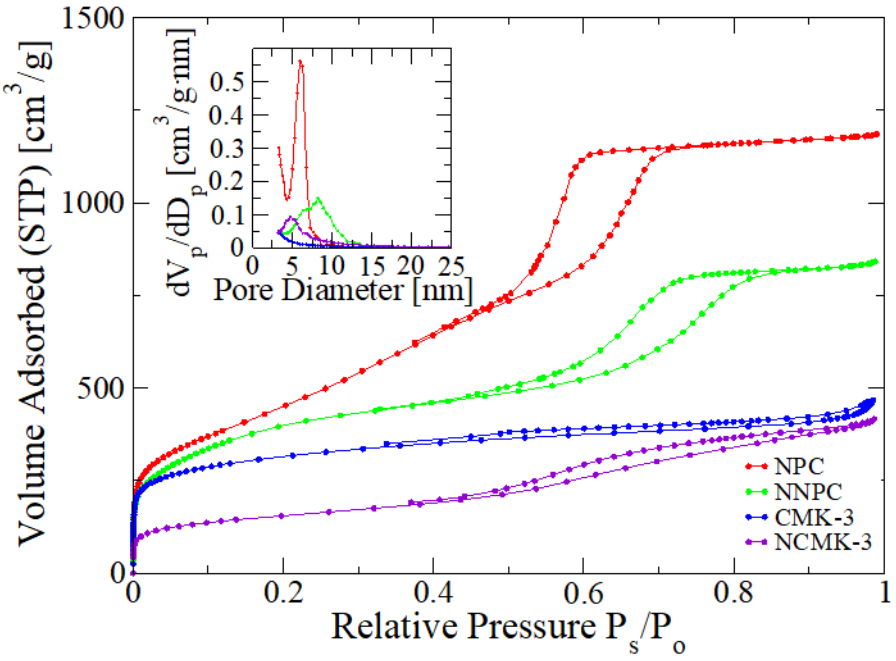

Figure 1. Nitrogen sorption isotherms and pore size distributions (inset) of synthesized porous carbon scaffolds. The NPC and NNPC isotherms have been shifted up 200 and 150 cm^3/g, respectively, for clarity.

Total pore volume and surface area of the NPC type scaffolds is considerably larger than those of the CMK-3 type. Surface area, pore volume, and average pore size of the respective doped/undoped scaffolds of each geometry are comparable, facilitating a minimization in the variation of substrate-induced effects that could alter the hydrogen sorption properties of an infiltrated metal hydride, allowing any influence of nitrogen-functionalizing the scaffolds to be more readily discerned.

Table 1. Summary of Carbon Physical Properties Measured with N_2 Physisorption at 77K.

sample	Pore size[a,b] [nm]	S_{BET}[c] [m^2/g]	V_T[d] [cm^3/g]
NPC	6.0	1290	1.63
NNPC	7.5	1426	1.30
CMK-3	3.5	1073	1.08
NCMK-3	3.0	764	0.84

[a] Average pore diameter. [b] Calculated by the BJH method using adsorption branch isotherm data. [c] Calculated using the BET method in a relative pressure range of 0.05 to 0.2. [d] Total pore volume: estimated from the amount adsorbed at a relative pressure (P_s/P_0) of 0.99.

X-ray photoelectron spectroscopy (XPS) measurements were employed to investigate the chemical makeup of the synthesized substrates. Analysis included a survey scan and detailed scans of the N 1s energy region for determination of nitrogen chemical bonding arrangements present in the samples. Survey scans indicated the NPC and CMK-3 substrates contained minor oxygen and nitrogen impurities, with carbon content exceeding 95 atomic percent as shown in Table 2. Figure 2(a) and 2(b) show the N1s spectrum recorded for the NNPC and NCMK-3 samples respectively. In the spectra of both doped samples, four different chemical bonding environments were identified, corresponding to pyridinic (~398 eV), pyrrolic (~400 eV), graphitic (~402 eV), and

oxidized nitrogen.[27,28] For each nitrogen bonding environment, the relative atomic concentration was calculated from the proportion of the area the fit function comprised of the total N 1s spectrum for each respective sample. Table 2 summarizes the relative atomic concentrations of each species obtained from the XPS analysis of the carbon samples. Of the identified nitrogen chemical bonding arrangements, the pyridinic nitrogen form is of considerable interest. In this state, a nitrogen atom is sp^2 hybridized within an aromatic ring, participating in one π and two σ bonds with the nearby carbon atoms, leaving a lone pair of electrons available for additional bonding.

Carbon scaffolds containing pyridinic nitrogen on their pore wall surface could act as a Lewis base and donate considerable electron density to a confined metal hydride within the nanopore volume, possibly resulting in an alteration of the hydriding properties observed for a metal hydride confined within a comparable non-functionalized carbon scaffold of the same geometry.

As a means of observing the effects nitrogen functionalization may have on the hydriding properties of a metal hydride confined within the pore volume of a carbon substrate, the four previously described scaffolds were infiltrated with 20 wt. % of $NaAlH_4$, followed by experimental activation energy and hydrogen cycling measurements of the respective composite systems. In order to verify that the $NaAlH_4$ was successfully infiltrated into the pores of the scaffolds, nitrogen sorption, powder X-ray diffraction (PXRD), and NMR measurements were taken. Figure S1 (Supporting Information) shows a representative plot comparing the isotherm and pore volume distribution of the NPC carbon scaffold before and after the hydride infiltration process. After infiltration, there is a considerable decrease in volume absorbed over the whole of

the isotherm indicating some portion of the substrate surface is now inaccessible to the nitrogen adsorbate, most likely due to the blocking or filling of substrate pores as evidenced by the shifted pore volume distribution shown in the inset.

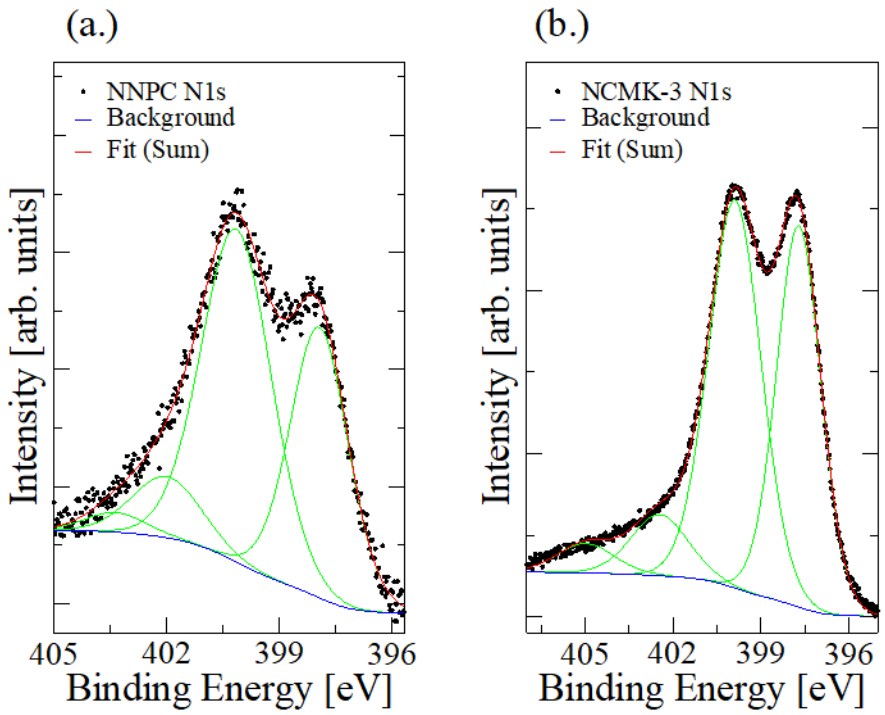

Figure 2. N 1s spectra for (a.) NNPC and (b.) NCMK-3. Four different chemical bonding environments were identified in the spectra of both samples. Namely, pyridinic (~398 eV), pyrrolic (~400 eV), graphitic (~402 eV), and oxidized (402-405 eV) nitrogen.[27,28]

All of the carbon scaffolds exhibited similar behavior after infiltration. We note here and from previous nitrogen sorption measurements that the observed decrease in substrate pore volume after $NaAlH_4$ infiltration is generally slightly higher than expected from a 20 wt.% $NaAlH_4$ loading, supporting the notion of minor pore blocking, but

consistent with previous studies.[4] Figure S2 shows the PXRD scans taken of the infiltrated and as-prepared substrates. The absence of any $NaAlH_4$ peaks after infiltration confirms there is little or no $NaAlH_4$ present outside the pores and any $NaAlH_4$ within the pores is amorphous, suggesting any intact hydride must be confined within the pore structure. Additionally, during this work we found that other samples having identical or slightly higher $NaAlH_4$ loadings and similar pore volume decreases to those described here also exhibited $NaAlH_4$ PXRD reflections, likely due to inadequate mixing of $NaAlH_4$/carbon substrate prior to the infiltration step. Subsequently, PXRD provides a much stronger indicator of successful pore infiltration.

NMR measurements were conducted to determine which amorphous hydride phases are present in the composite samples. ^{23}Na and ^{27}Al NMR measurements (Figures S3 to S9) show the existence of $NaAlH_4$ in the composite samples and no presence of the NaH or Na_3AlH_6 phases. The ^{23}Na local environment is strongly influenced by the electric field gradient and magnetic susceptibility of the carbon scaffold leading to the different line widths and chemical shifts of the samples. ^{23}Na NMR spectra (S3 to S5) for confined $NaAlH_4$ are significantly broadened and shifted compared to bulk $NaAlH_4$. It is difficult to determine through NMR whether this Na is intercalated into the framework, however, ^{23}Na and ^{27}Al NMR do not indicate the presence of NaH or Na_3AlH_6. Taken together with the N_2 sorption and PXRD measurements, the NMR results indicate that the confinement of $NaAlH_4$ within the carbon scaffold pores was indeed successful. Peaks corresponding to Al can be seen in both the ^{27}Al NMR and PXRD spectra, due to decomposition of a significant fraction of the hydride during infiltration, even at 200 bar H_2, which is considerably higher than the reported equilibrium pressure of 128 bar at 184

°C for the bulk hydride.[29] Measurements performed on a separate set of samples infiltrated at 350 bar H_2 still displayed the presence of Al, indicating decomposition occurs, presumably during the initial substrate wetting process. The spectra for all four composite samples show Al metal but are devoid of the Na_3AlH_6 phase, consistent with previous studies of $NaAlH_4$/C composite systems.[4,5,10,30] Table S1 lists the relative amounts of Al and $NaAlH_4$ calculated from the spectra. In general the decomposition on infiltration results in about 10 to 70% of aluminum in the metallic state. Although the samples are sealed in separate containers, some oxygen contamination is unavoidable given the surface areas and reactivity of the nanoparticle Al-containing phases. For this reason, peaks corresponding to Al_2O_3 are evident in some ^{27}Al spectra. Since large quantities of Al metal were detected in ^{27}Al NMR and PXRD measurements for both the nitrogen-functionalized and non-functionalized composite samples, the presence of nitrogen cannot be solely responsible for the noted decomposition. More likely, the catalytic effect of carbon itself during initial hydride wetting is the dominating feature, resulting in a favorable energy shift at the hydride/carbon interface that facilitates decomposition. In contrast, the NCMK-3/CMK-3 type scaffolds showed a higher decomposition compared to the NNPC/NPC versions, indicating the pore geometry might be a more important factor contributing to the degree of decomposition on initial wetting. In the previous study by[10] Nielson et al. the authors observed carbon aerogels with higher pore volumes and surface areas that appeared to stabilize molten $NaAlH_4$, resulting in less decomposition of $NaAlH_4$ to Al metal during the infiltration process. It is difficult to assess our samples for a similar trend, since the scaffolds of each type were purposely selected to match as closely as possible to minimize the impact of surface area and pore

volume in an attempt to elucidate the effect of nitrogen functionalization in contrast to the carbon aerogels used by Nielson et al. that had differences in surface area and pore volume of at least 44% and 30% respectively.[10] In the work here more decomposition upon infiltration was noted with the NNPC in comparison to NPC, with the NNPC having 10% more surface area, but 20 % less pore volume. In contrast a higher level of decomposition was noted during infiltration with the CMK-3 scaffold, having ~25% larger surface area and pore volume, displaying the opposite trend observed in the work by Nielson et al.[10]

Table 2. Summary of Relative Atomic Concentrations from XPS Measurements.

sample	carbon content [atom.%]	oxygen content [atom.%]	nitrogen total [atom.%]	pyridinic nitrogen [atom.%]	pyrrolic nitrogen [atom.%]	graphitic nitrogen [atom.%]	other nitrogen [atom.%]
NPC	95.7	3.9	< 1	-	-	-	-
NNPC	84.6	10.5	5.0	1.8	2.6	0.5	0.1
CMK-3	98.1	1.4	< 1	-	-	-	-
NCMK-3	77.8	11.2	11.0	4.4	5.3	0.9	0.4

Arrhenius Analysis. The results of an Arrhenius analysis performed utilizing the methods developed by Sandrock et al.[31] are presented in Figure 3. Data for the bulk $NaAlH_4$ sample recorded previously by Sandrock et al.[31] in a similar experiment is shown for comparison with the nanoconfined samples. In agreement with previous work,[1,8,18] the

activation energy for H_2 desorption is lowered with respect to the bulk hydride in all nanoconfined samples. Interestingly, $NaAlH_4$ confined in the nitrogen functionalized scaffolds of both geometries exhibits activation energies at least 20 kJ/mol H_2 lower than $NaAlH_4$ confined in the corresponding non-functionalized scaffold. Considering the similarity in physical properties with respect to surface area, pore volume and pore distribution of the respective functionalized/non-functionalized scaffold pairs, it appears the presence of nitrogen has a profound effect on the H_2 desorption process. Previous studies indicate that Arrhenius analysis can provide significant insight concerning the processes occurring during hydrogen desorption.[31] However, if desorption does not occur in a single reaction step, the measured activation energy will reflect the multiple competing decomposition mechanisms on the molecular level, making unique determination of the decomposition a challenge.[32] In this regard, $NaAlH_4$ nanoconfined in porous scaffolds has been observed to desorb hydrogen in an apparent single step, without the formation of intermediate phases.[4,5,30] However, multiple processes including nucleation, diffusion, hydride/substrate interactions, and hydride phase transitions may occur during thermal decomposition simultaneously. Consequently, the activation energy of hydrogen desorption measured from isothermal Arrhenius analysis should therefore be viewed as an amalgamation of the energies associated with each individual process. Calculated errors for the hydrogen desorption rate are less than 1.7×10^{-3} wt.%/min. All of the data in Figure 3 was recorded during the first desorption from the infiltrated samples. Following rehydriding the experiment was repeated. The measured activation energies from the second experiment agree well with the initial findings. Table 3 lists the activation energies and pre-exponential rate constants obtained from the Arrhenius

analysis. Physically the pre-exponential rate constant or frequency factor describes the frequency of collisions between reactant species, and therefore is directly related to the desorption mechanism. As shown in Table 3, the rate constants increase with the activation energy. Though a trend is evident, determining the relation to the desorption mechanism is not straightforward due to the existence of impurities and the multiple phases present. Although studies of the bulk decomposition processes in $NaAlH_4$ have been identified,[33,34] the mechanisms for diffusion in real experiments are dramatically altered by the presence of impurities, for example oxygen in particular. This is most obviously seen in the identification of a rapidly mobile Al species identified in $NaAlH_4$ when oxygen is present even in small quantities.[35] In our decomposing material there are multiple phases in contact including solid, liquid, and gas phase reactants in addition to the variable surface morphology of the carbon, and the impurities that are present in the carbon.

Gas Desorption. To investigate the dehydriding process of confined $NaAlH_4$ in the presence of nitrogen atoms, the desorption of hydrogen from the samples was recorded during the third cycle. Figure 4 displays the third H_2 desorption cycle from RT to 300 °C at a ramp rate of 4 °C/min. The H_2 weight percent has been normalized considering the mass of $NaAlH_4$ present in each respective sample prior to the infiltration procedure. Due to the noted decomposition of a portion of the sample during infiltration, the wt.% desorbed for each sample in Figure 4 represents a lower bound and the actual sample capacity is likely higher. Hydrogen desorption during the first two cycles was used to measure the rate of desorption under isothermal conditions at different set temperatures as previously described and therefore is not directly comparable with the

data presented in Figure 4 as the total desorption capacity during the first two cycles cannot be accurately assessed due to the evacuation of the desorption volume between successive measurement points.

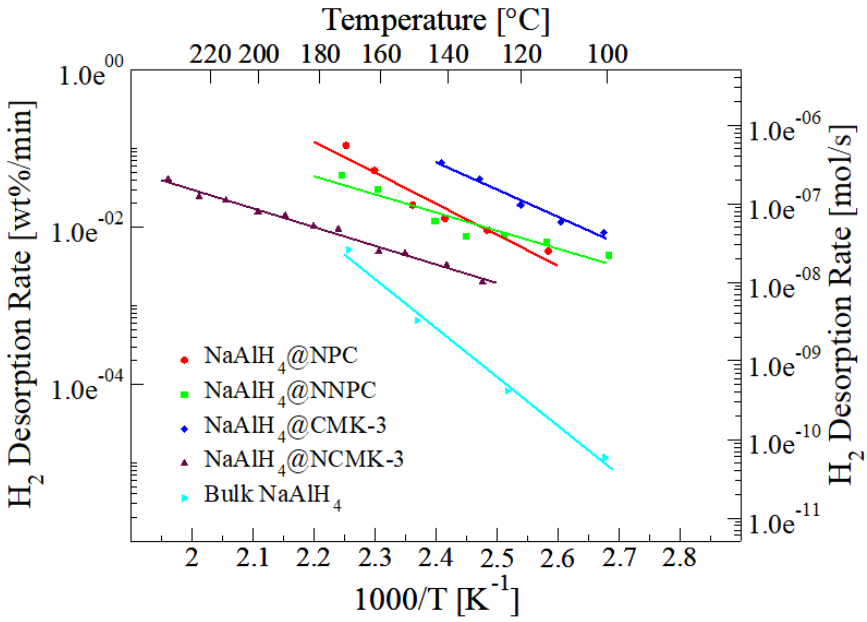

Figure 3. Arrhenius plots from isothermal desorption measurements. Data for the bulk $NaAlH_4$ was obtained from Sandrock et al.[31] and shown for comparison.

As displayed in Figure 4, all the samples still display reversibility after the initial two cycles noted. Additionally, Figure S9 shows $NaAlH_4$ is reformed following the third rehydriding cycle. Non-functionalized systems have a higher reversible capacity of ~3 wt% hydrogen with respect to the initial $NaAlH_4$ loading compared to ~1 wt% observed for the nitrogen functionalized samples. In Figure 4, the difference in the desorption profile between the nitrogen functionalized/non-functionalized systems is immediately apparent, as the composite systems functionalized with nitrogen do not desorb hydrogen in significant quantity until much higher temperature. Considering the results of the

Arrhenius analysis, which indicated activation energies for hydrogen desorption of at least 20 kJ/mol H_2 less in the nitrogen-functionalized samples, the behavior exhibited by these samples in the desorption profile is unexpected. To better understand the hydrogen desorption profile, it was instructive to consider the hydrogen desorption rate as a function of time. Using a forward difference routine, we calculated the derivative of the measured desorption data sets.

Table 3. Activation Energies Measured by Isothermal Arrhenius Analysis.

sample	activation energy [kJ/mol H_2]	rate constant [wt% H_2/min]	relative changes [kJ/mol H_2]
Bulk $NaAlH_4$	118.1[a]	3.3×10^{11} [a]	-
$NaAlH_4$@NPC	75.5 ± 10.4	5.9×10^{7}	Δ_{Bulk} = -42.6
$NaAlH_4$@NNPC	44.1 ± 6.6	5.1×10^{3}	Δ_{NPC} = -31.4
$NaAlH_4$@CMK-3	66.5 ± 5.7	1.5×10^{7}	Δ_{Bulk} = -51.6
$NaAlH_4$@NCMK-3	45.6 ± 1.7	1.7×10^{3}	Δ_{CMK3} = -20.9

[a]Data taken from Sandrock et al.[31]

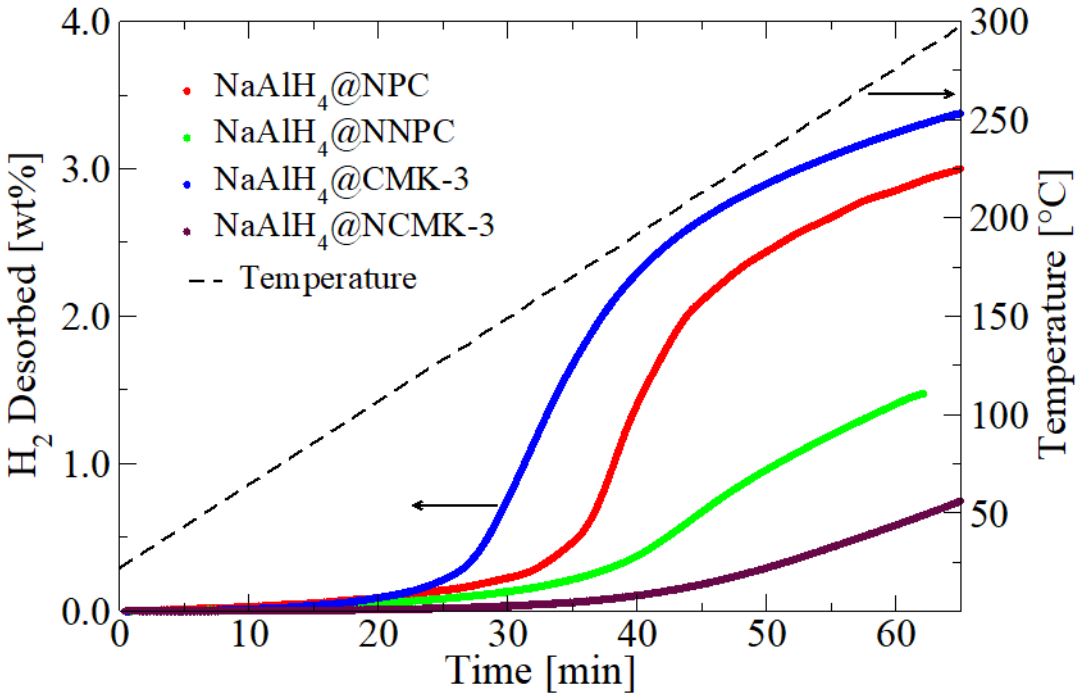

Figure 4. Hydrogen desorption (3rd cycle) from the $NaAlH_4$-infiltrated substrates. The black dashed trace displays the sample temperature profile.

Figure 5 shows the rate profiles resulting from differentiating the data presented in Figure 4. The rate curves are cut-off at the point corresponding to depletion of the $NaAlH_4$ reactant during decomposition. Profiles presented in Figure 5 highlight the significant difference in temperature at which hydrogen desorption from the nitrogen functionalized samples reach the highest rate of desorption in comparison to the respective non-functionalized scaffold. Small temperature fluctuations in the ramp rate are exacerbated in the forward difference resulting in, for example, the small deviations at 28 and 34 min for the data corresponding to $NaAlH_4$@NPC (red). This does not affect the clear difference in rates between nitrogen-doped and un-doped carbons. Black bars on the rate profiles indicate the temperature region where desorption rate measurements

were recorded during a separate isothermal Arrhenius experiment conducted to experimentally determine the activation energies in Table 3. We emphasize that the activation energies were not calculated using data from Figure 5; we show the temperature regions corresponding to the Arrhenius measurements for comparison only.

4. DISCUSSION

Previous studies of $NaAlH_4$ supported on nano-fibers[36] and $NaAlH_4$ nano-confined in a variety of materials including high surface area graphite,[4,5] carbon aerogels,[9,10,37] and metal organic frameworks (MOFs),[8,38] have all reported enhanced desorption kinetics and improved reversibility with regard to bulk $NaAlH_4$. In particular, the work by Balde et al.[36] demonstrated a correlation between decreasing nanoparticle size with a reduction in the activation energy and temperature of hydrogen desorption, in addition to a lower required pressure for hydrogen reloading. Balde et. al measured an activation energy of 58 kJ/mol H_2 for nanoparticles with a size distribution of 1-10 nm. A tighter bound on the nanoparticle size required to achieve activation energies below 60 kJ/mol H_2 was provided in subsequent studies of $NaAlH_4$ confined in highly ordered MOFs containing mono-disperse pore distributions near 1 nm,[8,38] reporting activation energies of 53.3 and 57.4 kJ/mol H_2. Our measured activation energies for the non-functionalized scaffolds in Table 3 are in relative agreement with the previous studies, measuring 75.5 and 66.5 kJ/mol H_2 for $NaAlH_4$ confined in NPC with an average pore size of 6 nm and CMK-3 with an average pore size of 3.5 nm. Considering the similar physical characteristics between the non-functionalized and functionalized scaffolds of both morphologies, it is interesting that the measured activation energies for $NaAlH_4$

confined in NNPC and NCMK-3 are reduced to 44.1 and 45.6 kJ/mol H_2 respectively. Based on previous studies, the hydride particle size alone in the surface functionalized systems cannot account for a decrease in activation below 50 kJ/mol H_2, suggesting the presence of nitrogen influences the hydrogen desorption process. In accordance with previous works on nano-confined $NaAlH_4$,[4,5,8-10,37,38] we observed significant temperature decreases for the onset of hydrogen desorption relative to bulk $NaAlH_4$ and maximum rates of hydrogen desorption <180 °C for the samples confined in non-functionalized scaffolds. In contrast, samples of $NaAlH_4$ confined in nitrogen-functionalized scaffolds show a less pronounced decrease in the onset of hydrogen desorption and display maximum rates of hydrogen desorption at temperatures exceeding 200 °C. In view of the further decreased activation energy for the nitrogen-functionalized samples the shift in maximum desorption rate to *higher* temperatures is unexpected. There appears to be some correlation between the shifting of maximum hydrogen desorption rate to higher temperature and nitrogen content of the carbon scaffolds, as the temperature shift is considerably larger for the CMK-3/NCMK-3 pair, where the NCMK-3 scaffold contains roughly 2 times more nitrogen than the NNPC scaffold. Although the magnitude of the temperature shift could be a function of the pore geometry, this seems less likely in view of the similarity in the shapes of the desorption and desorption rate profiles for the functionalized and non-functionalized samples respectively, even though the scaffolds have markedly different pore geometries.

It is difficult to determine uniquely the mechanism through which nitrogen addition to the scaffold surface acts to influence $NaAlH_4$ in this system, though previous studies concerning carbon scaffold surface chemistry may provide insight into some of

the general underlying features. Through modeling and experiment, Berseth et al.[39] found that the presence of carbon scaffolds (graphene, nanotubes, and C_{60}) destabilized the $NaAlH_4$ as a result of the charge transfer from Na atoms to the electronegative carbon scaffold at the hydride/scaffold interface, resulting in a weakening of the Na-AlH_4 ionic bond that is correlated with the electron affinity and curvature of the carbon substrate. Surface functionalization with nitrogen will increase the electron density in the scaffold but should remain localized near the nitrogen heteroatom, giving rise to the XPS spectra indicating pyridinic and pyrrolic signatures. The amorphous nature of our carbons and the presence of adsorbates (Na, NaH, Al, AlH_x, etc.) and impurities such as oxygen preclude a definitive explanation of the anomalous desorption rates. Putting aside these difficulties, first principles calculations of the electronic properties of N-doped graphene monolayers show the electronic DOS is shifted down with respect to a non-functionalized graphene sheet, due to additional filling of electronic states around the Fermi level from the increased number of valence electrons as a result of nitrogen inclusion.[40] There are unfilled electronic states in the vicinity of the Fermi level, indicating that the transfer of electron density from an adsorbate species in close proximity to the scaffold is allowed and should depend on the relative electronic energy levels of the scaffold and adsorbate species respectively. In regard to defects such as edge sites, measurements of the local DOS on the surface of nitrogen-functionalized graphite indicated nitrogen atoms in the pyridinic configuration are likely to be negatively charged and should act as Lewis bases with respect to adsorbate species.[41]

Although the exact mechanism responsible for the observed anomalous desorption is not fully understood, it must be associated with interactions between the

hydride and host surface. It is also important to note that the fastest desorption in the functionalized carbons takes place above 180 °C, the melting temperature of bulk $NaAlH_4$[5,29] and suggests the anomalous behavior is linked with the transition of $NaAlH_4$ from the solid to liquid phase in the presence of nitrogen atoms in the functionalized substrate. Desorption data in Figure 4 indicate that the majority of hydrogen is released above ~ 180 °C. Figure 5 shows the maximum desorption rate coincides with this observation as well. Further, NMR measurements confirmed considerable hydride decomposition occurs during infiltration where $NaAlH_4$ is in the liquid phase. Due to the partial decomposition of a fraction of $NaAlH_4$ during infiltration it is likely Al metal and some Na species coexist in the pores with the intact $NaAlH_4$. This Na species cannot be positively identified as NaH, and there is no indication from ^{27}Al NMR that Na_3AlH_6 has formed. Intercalated Na in the framework would generally increase the electron density in the local environment and this may influence the surface energies of adsorbed $NaAlH_4$ which could influence the desorption kinetics and/or mechanism. Finally, nano-confinement of $NaAlH_4$ causes a shift in melting temperature from that of the bulk phase due to mechanical effects such as substrate induced lattice strain, or through chemical interaction with the substrate, or electronic effects.[4,5]

5. CONCLUSIONS

We presented evidence from N_2 sorption, XPS, PXRD, and NMR measurements that indicate two different types of nanoporous carbon scaffolds, both with and without nitrogen surface functionalization, were successfully infiltrated with $NaAlH_4$. After infiltration no reflections from crystalline $NaAlH_4$ were detected during PXRD

measurements, indicating any intact $NaAlH_4$ is amorphous. ^{27}Al MAS NMR and PXRD detect the presence of Al metal revealing a fraction of $NaAlH_4$ decomposes during infiltration in the presence of all carbon scaffolds of both geometries at hydrogen pressures well in excess of the bulk equilibrium pressure at melting,[29] suggesting a strong interaction with the scaffold surface. Despite some decomposition, NMR confirms the existence of intact $NaAlH_4$, with no detection of the Na_3AlH_6 or NaH phases present in the samples. Isothermal Arrhenius analysis indicates the activation energy for hydrogen desorption from nitrogen-functionalized carbons is decreased by 20 kJ/mol or more over the non-functionalized carbons. The presence of nitrogen evidently has a significant influence on the desorption process. Hydrogen cycling measurements indicate that hydrogen can be reversibly stored within all the scaffolds examined, with a reversible storage capacity up to 3 wt% H_2 after 3 cycles with the pore loading achieved in this work. Higher levels of reversible capacity could likely be attained with higher pore loadings. During the hydrogen desorption process, the majority of hydrogen is not released until higher temperatures for $NaAlH_4$ confined in the nitrogen-functionalized scaffolds, despite the significantly lower measured activation energies. This indicates the existence of a rate-limiting step for desorption that may be linked to the level of nitrogen doping in the scaffolds and the onset of $NaAlH_4$ melting. Further investigation will include magic angle spinning nuclear magnetic resonance experiments using the NCMK-3 scaffold, but with labeled ^{15}N isotope-containing scaffolds.

Ultimately, our results show that nanoconfinement and surface functionalization of carbon substrates allows for dramatically altering the kinetic behavior, and possibly thermodynamics, governing the decomposition of $NaAlH_4$ and potentially related

complex hydrides. A detailed understanding of the basic mechanisms underlying these effects could yield a powerful tool for designing materials for hydrogen storage and other applications involving nanoporous carbon substrates.

ACKNOWLEDGMENT

Sandia National Laboratories is a multi-mission laboratory managed and operated by National Technology and Engineering Solutions of Sandia, LLC., a wholly owned subsidiary of Honeywell International, Inc., for the U.S. Department of Energy's National Nuclear Security Administration under contract DE-NA-0003525. The authors gratefully acknowledge research support from the Hydrogen Materials Advanced Research Consortium (HyMARC), established as part of the Energy Materials Network under the U.S. Department of Energy, Office of Energy Efficiency and Renewable Energy, Fuel Cell Technologies Office, under Award Number DOE-EE0007656.[42] The authors would like to thank Josh Whaley for the design and construction of clean-transfer holders for the XPS system.

SUPPORTING INFORMATION

Experimental Procedures:

Chemicals: Phenol, Formalin, tetraethyl orthosilicate (TEOS), Pluronic F-127 tri-block copolymer, dicyandiamide, carbon tetrachloride (CTC) and ethylenediamine

(EDA) were purchased from Sigma-Aldrich. SBA-15 silicate hard template was purchased from ACS Materials. Deionized water was used in all experiments.

NPC produced using inorganic/organic self-assembly method:[20:] Resol precursors: In a typical process, 6.1 g of phenol was melted in a Schlenk flask at 40 ºC and added to 1.3 g of 20 wt.% NaOH solution under stirring. At the end of 10 minutes, 10.5 g of formalin was added at a temperature below 50 ºC dropwise. The resulting mixture was placed in a water bath at 70 ºC under stirring for 80 minutes and then allowed to cool to room temperature (RT). Using 1 N HCl the pH of the solution was adjusted to ~7.0. Water was removed from the solution under vacuum at 45 ºC, producing a gel-like product. Ethanol was added to dissolve the product, producing a 20 wt.% resol-ethanol solution after mixing. The solution was allowed to settle and then poured off into a separate flask, leaving behind the salt from the acid-base neutralization.

NPC synthesis: In a typical process to produce 2D hexagonal carbon, 16 g F-127 tri-block copolymer was added to a solution consisting of 80 g ethanol and 10 g 0.2 M HCl. After stirring for 1 hour at 40 ºC, 20.8 g TEOS and 50 g of 20 wt.% resol-ethanol solution were added sequentially, followed by stirring for 2 hours at 40 ºC. The solution was poured into a glass pan and allowed to evaporate overnight at RT, producing a transparent film. In order to thermopolymerize the sample, heat treatment at 100 ºC was carried out in an oven for 24 hours. The sample was scraped from the pan, ground into a fine powder, and placed into a tube furnace under flowing nitrogen for calcination at 350 ºC for 3 hours, followed by carbonization at 900 ºC for 2 hours. During the heat treatment the ramp rate was 1 ºC/min below 600 ºC and 5 ºC/min after. To remove the silicate, the

sample was etched in 5 wt.% HF solution overnight twice under stirring, followed by washing with ethanol and deionized water. Finally, the carbon sample was dried for 24 hours at 100 ºC and additionally overnight at 300 ºC under dynamic vacuum. The final sample was transported without air exposure to an argon-filled glovebox for storage.

NNPC produced using inorganic/organic self-assembly method:[21:] In a typical process, 8 g of F-127 tri-block co-polymer and 7.5 g dicyandiamide are added to a solution consisting of 100 g ethanol, 50 g H_2O, and 10 g 0.2 M HCl. After stirring for 1 hour at 40 ºC, 10.4 g TEOS and 25 g of 20 wt.% resol-ethanol solution were added sequentially, followed by stirring for an additional 2 hours at 40 ºC. In order to evaporate the solvent, the mixture was poured into pans and placed in an oven at 45 ºC for 8 hours resulting in the formation of uniform films. In order to thermopolymerize the sample, heat treatment at 100 ºC was carried out in an oven for 24 hours. The sample was scraped from the pan, ground into a fine powder, and placed into a tube furnace under flowing nitrogen for calcination at 250 ºC for 2 hours, followed by carbonization at 700 ºC for 3 hours. During the heat treatment the ramp rate was 1 ºC/min. To remove the silicate, the sample was etched in 5 wt.% HF solution overnight twice under stirring, followed by washing with ethanol and deionized water. Finally, the carbon sample was dried for 24 hours at 100 ºC and additionally overnight at 300 ºC under dynamic vacuum. The final sample was transported without air exposure to an argon-filled glovebox for storage.

CMK-3 produced using the nanocasting method:[22:] In a typical synthesis, 6.25 g sucrose was dissolved in a mixture consisting of 0.7 g H_2SO_4 and 25 g H_2O, followed by

the addition of 5 g SBA-15 silicate hard template material. After 15 minutes of stirring, a uniform white slurry was obtained. Heat treatments of the sample at 100 ºC for 6 hours and 160 ºC for 6 hours were performed sequentially. The resulting black/brown powder sample was added to a solution consisting of 4 g sucrose dissolved in 0.45 g H_2SO_4 and 25 g H_2O. After 25 minutes of stirring the previous heat treatments were repeated, followed by carbonization of the sample in a tube furnace at 900 ºC under flowing argon for 3 hours. During the heat treatment the ramp rate was 1 ºC/min below 600 ºC and 5 ºC/min after. To remove the hard silicate template, the sample was etched in 5 wt.% HF solution overnight twice under stirring, followed by washing with ethanol and deionized water. Finally, the carbon sample was dried for 24 hours at 100 ºC and additionally overnight at 300 ºC under dynamic vacuum. The final sample was transported without air exposure to an argon-filled glovebox for storage.

NCMK-3 produced using the nanocasting method:[23:] In a typical process using Schlenk line techniques, 6.75 g EDA and 15 g CTC were added to a jacketed flask under stirring at RT. Next, 2.5 g SBA-15 silicate template was added to the mixture of EDA and CTC under stirring slowly. The resultant mixture was allowed to stir for 1 hour until a uniform white slurry was obtained. Under continuous stirring, the temperature was increased to 90 ºC, at which the mixture was refluxed and stirred for 6 hours. The obtained brown colored solid mixture was placed in a drying oven at 100 ºC for 12 hours, and subsequently ground into a fine powder. Sample calcination was carried out in a tubular furnace under flowing nitrogen at 600 ºC for 5 hours. A ramp rate of 3 ºC/min was used to bring the sample up to 600 ºC. After calcination, the composite carbon/silica

powder was immersed in 5 wt.% HF acid solution under stirring to dissolve the silica template. Carbon powder was recovered following filtration and several washings with ethanol and deionized water. Finally, the carbon sample was dried for 24 hours at 100 ºC and additionally overnight at 300 ºC under dynamic vacuum. The final sample was transported without air exposure to an argon-filled glovebox for storage.

Nitrogen Sorption Supporting Information:

Scans were recorded on a Coulter SA3100 at 77 K.

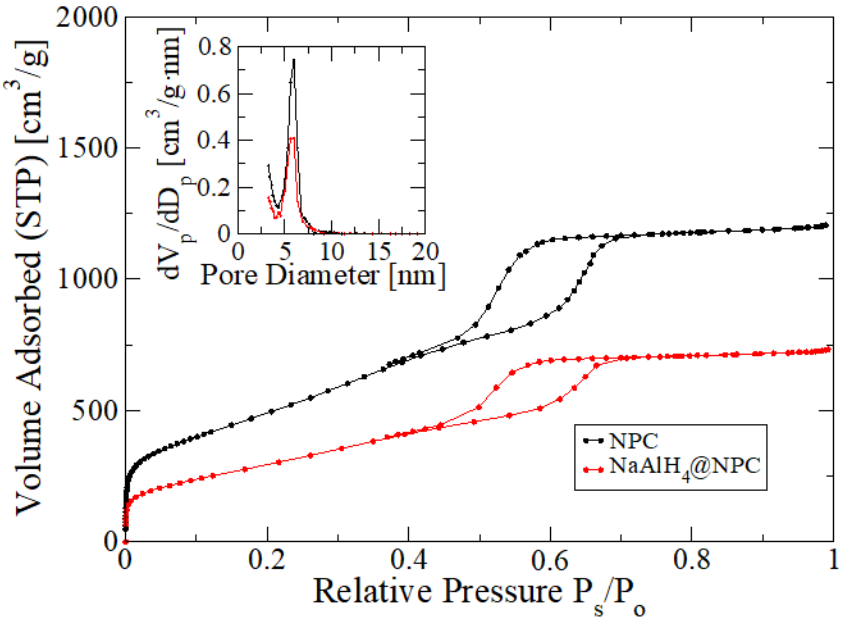

Figure S1. Nitrogen sorption isotherms and pore volume distributions (inset) for the NPC carbon substrate before and after infiltration with $NaAlH_4$. The decreased volume adsorbed over the whole of the isotherm indicates some portion of the available surface area is now inaccessible to the adsorbate, as a result of the filling or blocking of the substrate pores.

PXRD Supporting Information:

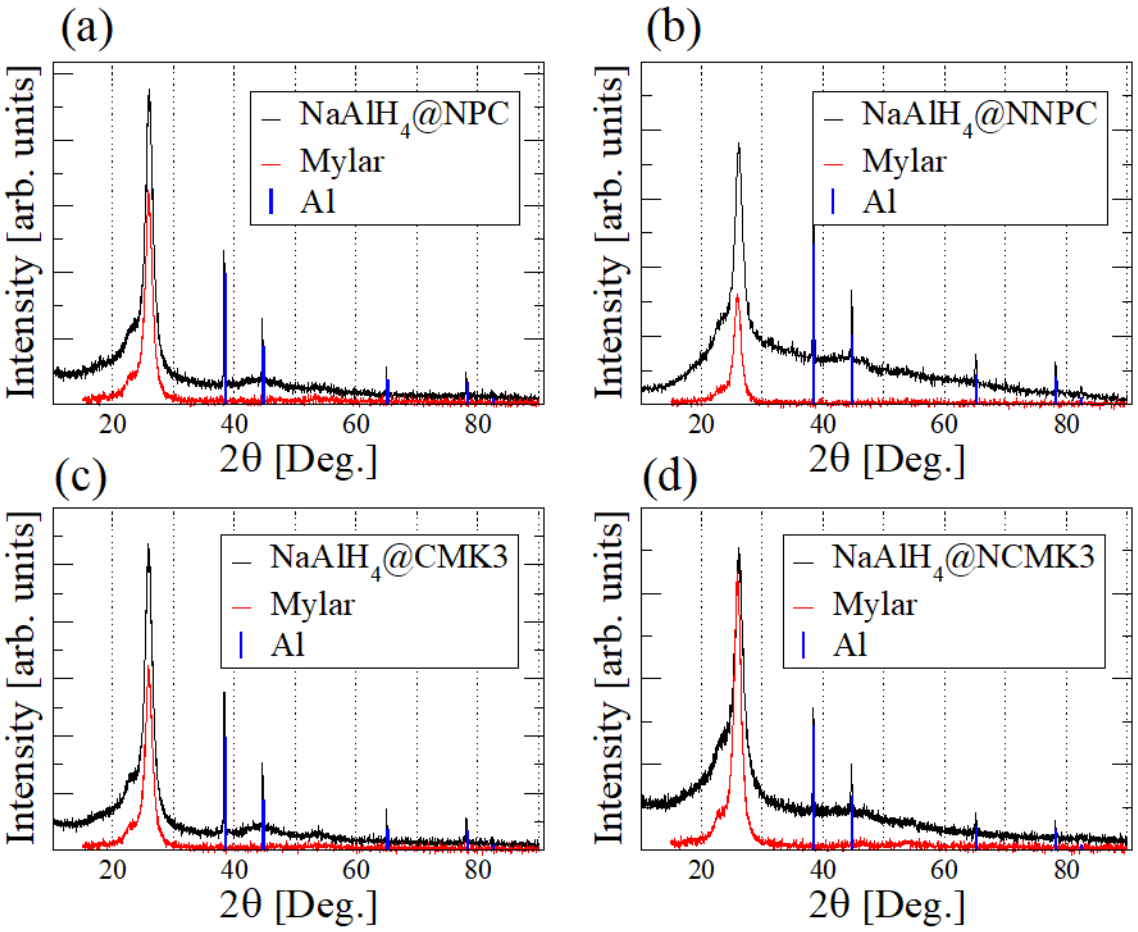

Figure S2. PXRD scans of infiltrated carbons: (a) NPC, (b) NNPC, (c) CMK-3, and (d) NCMK-3. Mylar film was used to cover the sample to avoid air exposure. No peaks from crystalline $NaAlH_4$ were detected, indicating the presence of little or no $NaAlH_4$ outside the pores, and indicating $NaAlH_4$ contained inside the pores is amorphous**.**

Table S1. $NaAlH_4$ and Al Metal Content of Infiltrated Carbon Scaffolds.

Sample	$NaAlH_4$	Al metal	Al_2O_3
$NaAlH_4$@CMK-3	26.5%	73.5%	0%
$NaAlH_4$@NCMK-3	68.0%	32.0%	0%
$NaAlH_4$@NPC	89.2%	10.8%	0%
$NaAlH_4$@NNPC	20.1%	22.3%	26.9%

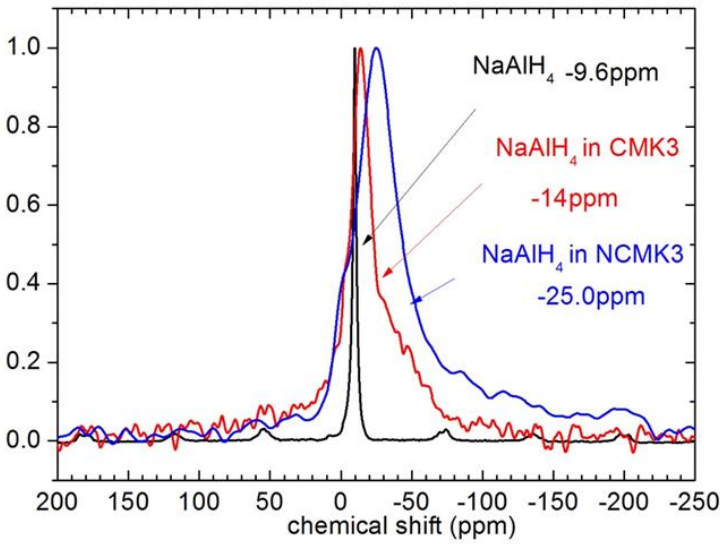

Figure S3. ^{23}Na 5 kHz MAS NMR spectra referenced to a 6 M NaCl solution showing measured chemical shifts for bulk $NaAlH_4$, $NaAlH_4$@CMK-3, and $NaAlH_4$@NCMK-3 indicating $NaAlH_4$ remains intact after confinement in the carbon scaffolds. The position of the observed $NaAlH_4$ line is consistent with previous studies of the bulk hydride.[42]

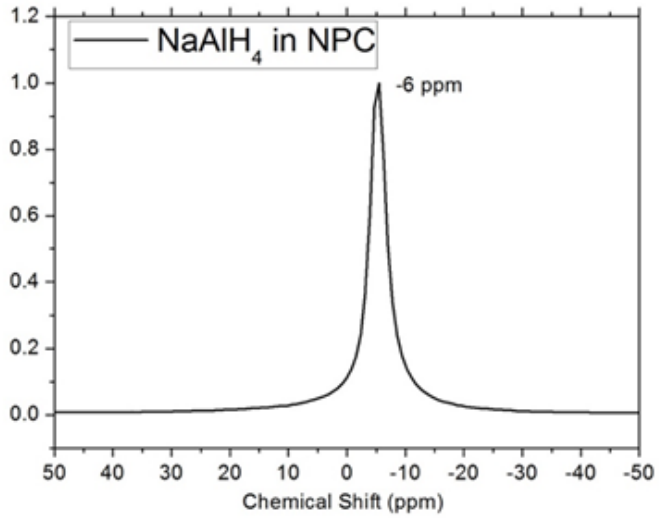

Figure S4. ^{23}Na 25 kHz MAS NMR spectra referenced to a 6 M NaCl solution at 156.022 MHz for $NaAlH_4$@NPC. The observed $NaAlH_4$ line position is consistent with previous studies of bulk $NaAlH_4$.[5]

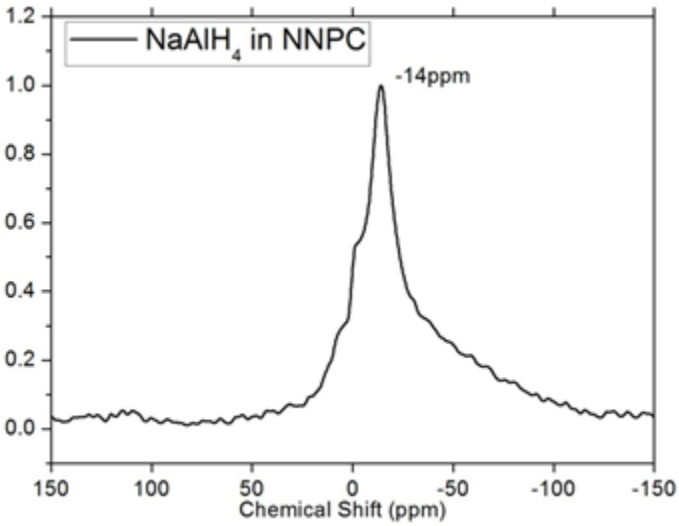

Figure S5. ^{23}Na 9 kHz MAS NMR spectra referenced to a 6 M NaCl solution at 79.27 MHz for $NaAlH_4$ in NNPC. The observed $NaAlH_4$ line position is consistent with previous studies of bulk $NaAlH_4$.[5]

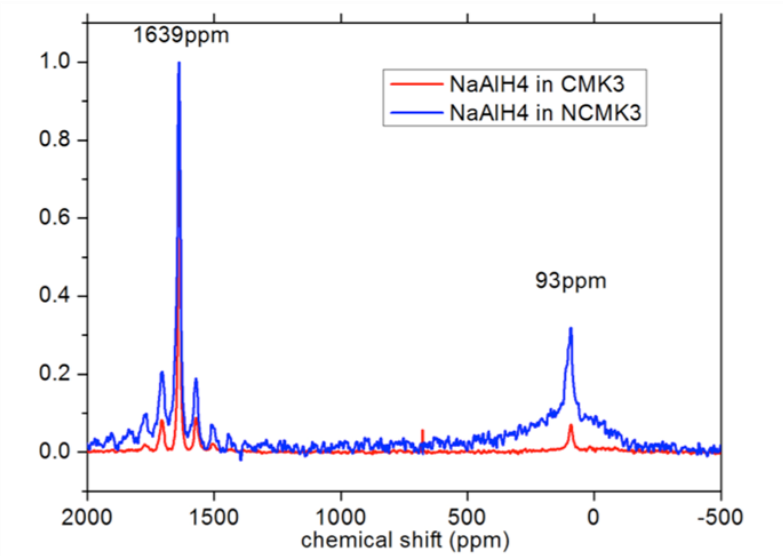

Figure S6. ^{27}Al 5 kHz MAS NMR referenced to 1 M $Al(NO_3)_3$ solution. $NaAlH_4$-infiltrated carbon samples have one Al metal peak at 1639 ppm and a $NaAlH_4$ peak at 93 ppm.[5]

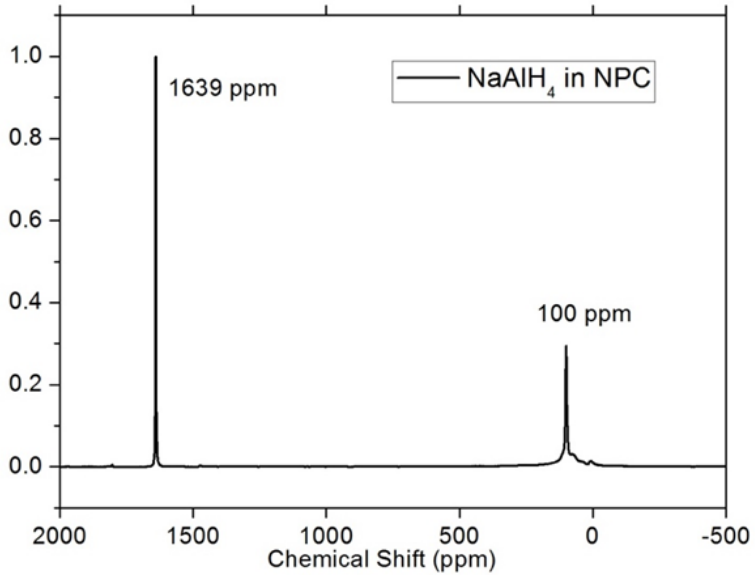

Figure S7. ^{27}Al 25 kHz MAS NMR referenced to 1 M Al(NO3)3 solution at 153.69 MHz for $NaAlH_4$@NPC. There is one Al metal peak at 1639 ppm and one $NaAlH_4$ peak at 100 ppm.

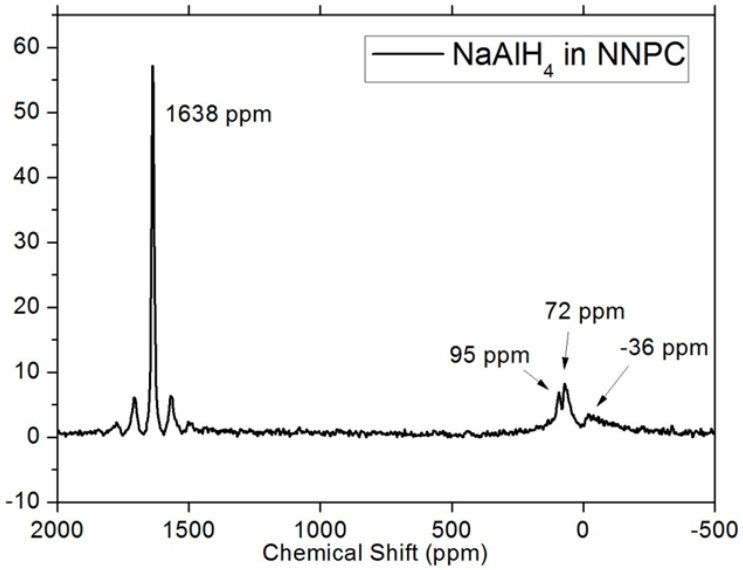

Figure S8. ^{27}Al 5 kHz MAS NMR referenced to 1 M Al(NO3)3 solution at 78.085 MHz. Although the samples are sealed in separate containers, some oxygen contamination is unavoidable given the surface areas and reactivity of the nanoparticle Al-containing phases. For this reason, peaks corresponding to Al_2O_3 are evident in the ^{27}Al spectra. There is still one Al metal peak at 1639 ppm and a $NaAlH_4$ peak at 95 ppm.[5]

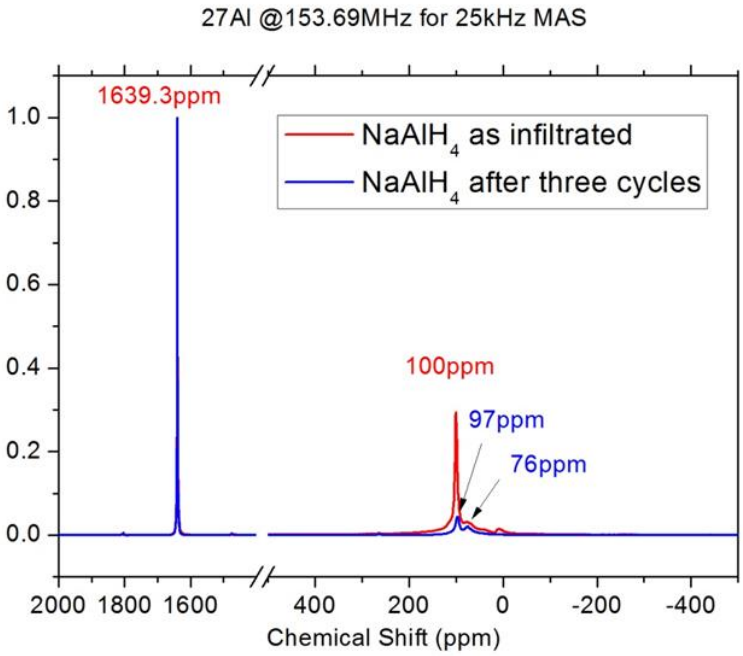

Figure S9. $NaAlH_4$@NPC as infiltrated and after three cycles ^{27}Al 25 kHz MAS NMR. Reference 1M $Al(NO_3)_3$ solution at 153.69 MHz. There is one Al metal peak at 1639 ppm and a $NaAlH_4$ peak at 97 ppm after 3 cycles.[5] Although the samples are sealed in separate containers, some oxygen contamination is unavoidable given the surface areas and reactivity of the nanoparticle Al-containing phases. For this reason, peaks corresponding to Al_2O_3 are evident in the ^{27}Al spectra.

REFERENCES

1. Gross, A. F.; Vajo, J. J.; Van Atta, S. L.; Olson, G. L. Enhanced Hydrogen Storage Kinetics of $LiBH_4$ in Nanoporous Carbon Scaffolds. *J. Phys. Chem. C* **2008**, *112*, 5651–5657.

2. Cahen, S.; Eymery, J.-B.; Janot, R.; Tarascon, J.-M. Improvement of the $LiBH_4$ Hydrogen Desorption by Inclusion into Mesoporous Carbons. *J. Power Sources* **2009**, *189*, 902–908.

3. Stephens, R. D.; Gross, A. F.; Van Atta, S. L.; Vajo, J. J.; Pinkerton, F. E. The Kinetic Enhancement of Hydrogen Cycling in $NaAlH_4$ by Melt Infusion into Nanoporous Carbon Aerogel. *Nanotechnology* **2009**, *20*, 204018.

4. Adelhelm, P.; Gao, J.; Verkuijlen, M. H. W.; Rongeat, C.; Herrich, M.; van Bentum, P. J. M.; Gutfleisch, O.; Kentgens, A. P. M.; de Jong, K. P.; de Jongh, P. E. Comprehensive Study of Melt Infiltration for the Synthesis of $NaAlH_4$/C Nanocomposites. *Chem. Mater.* **2010**, *22*, 2233–2238.

5. Gao, J.; Adelhelm, P.; Verkuijlen, M. H. W.; Rongeat, C.; Herrich, M.; van Bentum, P. J. M.; Gutfleisch, O.; Kentgens, A. P. M.; de Jong, K. P.; de Jongh, P. E. Confinement of $NaAlH_4$ in Nanoporous Carbon: Impact on H_2 Release, Reversibility, and Thermodynamics. *J. Phys. Chem. C* **2010**, *114*, 4675–4682.

6. Liu, X.; Peaslee, D.; Jost, C. Z.; Majzoub, E. H. Controlling the Decomposition Pathway of $LiBH_4$ via Confinement in Highly Ordered Nanoporous Carbon. *J. Phys. Chem. C* **2010**, *114*, 14036–14041.

7. Liu, X.; Peaslee, D.; Jost, C. Z.; Baumann, T. F.; Majzoub, E. H. Systematic Pore-Size Effects of Nanoconfinement of $LiBH_4$: Elimination of Diborane Release and Tunable Behavior for Hydrogen Storage Applications. *Chem. Mater.* **2011**, *23*, 1331–1336.

8. Stavila, V.; Bhakta, R. K.; Alam, T. M.; Majzoub, E. H.; Allendorf, M. D. Reversible Hydrogen Storage by $NaAlH_4$ Confined within a Titanium-Functionalized MOF-74(Mg) Nanoreactor. *ACS Nano* **2012**, *6*, 9807–9817.

9. Nielsen, T. K.; Javadian, P.; Polanski, M.; Besenbacher, F.; Bystrzycki, J.; Jensen, T. R. Nanoconfined $NaAlH_4$: Determination of Distinct Prolific Effects from Pore Size, Crystallite Size, and Surface Interactions. *J. Phys. Chem. C* **2012**, *116*, 21046–21051.

10. Nielsen, T. K.; Javadian, P.; Polanski, M.; Besenbacher, F.; Bystrzycki, J.; Skibsted, J.; Jensen, T. R. Nanoconfined $NaAlH_4$: Prolific Effects from Increased Surface Area and Pore Volume. *Nanoscale* **2014**, *6*, 599–607.

11. Klebanoff, L. E.; Keller, J. O. 5 Years of Hydrogen Storage Research in the U.S. DOE Metal Hydride Center of Excellence (MHCoE). *Int. J. Hydrogen Energy* **2013**, *38*, 4533–4576.

12. Mason, T.; Majzoub, E. H. Effects of a Carbon Surface Environment on the Decomposition Properties of Nanoparticle $LiBH_4$: A First-Principles Study. *J. Phys. Chem. C* **2014**, *118*, 8852–8858.

13. Remhof, A.; Mauron, P.; Züttel, A.; Embs, J. P.; Łodziana, Z.; Ramirez-Cuesta, A. J.; Ngene, P.; de Jongh, P. Hydrogen Dynamics in Nanoconfined Lithiumborohydride. *J. Phys. Chem. C* **2013**, *117*, 3789–3798.

14. Verdal, N.; Udovic, T. J.; Rush, J. J.; Liu, X.; Majzoub, E. H.; Vajo, J. J.; Gross, A. F. Dynamical Perturbations of Tetrahydroborate Anions in $LiBH_4$ due to Nanoconfinement in Controlled-Pore Carbon Scaffolds. *J. Phys. Chem. C* **2013**, *117*, 17983–17995.

15. Suwarno; Ngene, P.; Nale, A.; Eggenhuisen, T. M.; Oschatz, M.; Embs, J. P.; Remhof, A.; de Jongh, P. E. Confinement Effects for Lithium Borohydride: Comparing Silica and Carbon Scaffolds. *J. Phys. Chem. C* **2017**, *121*, 4197–4205.

16. Shane, D. T.; Corey, R. L.; McIntosh, C.; Rayhel, L. H.; Bowman, R. C.; Vajo, J. J.; Gross, A. F.; Conradi, M. S. $LiBH_4$ in Carbon Aerogel Nanoscaffolds: An NMR Study of Atomic Motions. *J. Phys. Chem. C* **2010**, *114*, 4008–4014.

17. Zou, H.; Gradišek, A.; Emery, S. B.; Vajo, J. J.; Conradi, M. S. $LiBH_4$ in Aerogel: Ionic Motions by NMR. *J. Phys. Chem. C* **2017**, *121*, 15114–15119.

18. Carr, C. L.; Majzoub, E. H. Surface-Functionalized Nanoporous Carbons for Kinetically Stabilized Complex Hydrides through Lewis Acid–Lewis Base Chemistry. *J. Phys. Chem. C* **2016**, *120*, 11426–11432.

19. Bogdanović, B.; Schwickardi, M. Ti-Doped Alkali Metal Aluminium Hydrides as Potential Novel Reversible Hydrogen Storage Materials. *J. Alloys Compd.* **1997**, *253-254*, 1–9.

20. Liu, R.; Shi, Y.; Wan, Y.; Meng, Y.; Zhang, F.; Gu, D.; Chen, Z.; Tu, B.; Zhao, D. Triconstituent Co-Assembly to Ordered Mesostructured Polymer−Silica and Carbon−Silica Nanocomposites and Large-Pore Mesoporous Carbons with High Surface Areas. *J. Am. Chem. Soc.* **2006**, *128*, 11652–11662.

21. Song, Y.; Li, L.; Wang, Y.; Wang, C.; Guo, Z.; Xia, Y. Nitrogen-Doped Ordered Mesoporous Carbon with a High Surface Area, Synthesized through Organic-Inorganic Coassembly, and Its Application in Supercapacitors. *ChemPhysChem* **2014**, *15*, 2084–2093.

22. Jun, S.; Joo, S. H.; Ryoo, R.; Kruk, M.; Jaroniec, M.; Liu, Z.; Ohsuna, T.; Terasaki, O. Synthesis of New, Nanoporous Carbon with Hexagonally Ordered Mesostructure. *J. Am. Chem. Soc.* **2000**, *122*, 10712–10713.

23. Vinu, A.; Ariga, K.; Mori, T.; Nakanishi, T.; Hishita, S.; Golberg, D.; Bando, Y. Preparation and Characterization of Well-Ordered Hexagonal Mesoporous Carbon Nitride. *Adv. Mater.* **2005**, *17*, 1648–1652.

24. Pierotti, R.; Rouquerol, J. Reporting Physisorption Data for Gas/Solid Systems with Special Reference to the Determination of Surface Area and Porosity. *Pure Appl. Chem*. **1985**, *57*, 603–619.

25. Zhao, D.; Feng, J.; Huo, Q.; Melosh, N.; Fredrickson, G. H.; Chmelka, B. F.; Stucky, G. D. Triblock Copolymer Syntheses of Mesoporous Silica with Periodic 50 to 300 Angstrom Pores. *Science* **1998**, *279*, 548–552.

26. Kruk, M.; Jaroniec, M.; Ko, C. H.; Ryoo, R. Characterization of the Porous Structure of SBA-15. *Chem. Mater.* **2000**, *12*, 1961–1968.

27. Sun, F.; Liu, J.; Chen, H.; Zhang, Z.; Qiao, W.; Long, D.; Ling, L. Nitrogen-Rich Mesoporous Carbons: Highly Efficient, Regenerable Metal-Free Catalysts for Low-Temperature Oxidation of H_2S. *ACS Catal.* **2013**, *3*, 862–870.

28. Zhao, Z.; Dai, Y.; Lin, J.; Wang, G. Highly-Ordered Mesoporous Carbon Nitride with Ultrahigh Surface Area and Pore Volume as a Superior Dehydrogenation Catalyst. *Chem. Mater.* **2014**, *26*, 3151–3161.

29. Dymova, T. N.; Dergachev, Y. M.; Sokolov, V. A.; Grechanaya, N. A. Dissociation Pressure of $NaAlH_4$ and Na_3AlH_6. *Dokl. Akad. Nauk SSSR* **1975**, *224*, 591–592.

30. Verkuijlen, M. H. W.; Gao, J.; Adelhelm, P.; van Bentum, P. J. M.; de Jongh, P. E.; Kentgens, A. P. M. Solid-State NMR Studies of the Local Structure of $NaAlH_4$/C Nanocomposites at Different Stages of Hydrogen Desorption and Rehydrogenation. *J. Phys. Chem. C* **2010**, *114*, 4683–4692.

31. Sandrock, G.; Gross, K.; Thomas, G. Effect of Ti-Catalyst Content on the Reversible Hydrogen Storage Properties of the Sodium Alanates. *J. Alloys Compd.* **2002**, *339*, 299–308.

32. Poonyayant, N.; Stavila, V.; Majzoub, E. H.; Klebanoff, L. E.; Behrens, R.; Angboonpong, N.; Ulutagay-Kartin, M.; Pakawatpanurut, P.; Hecht, E. S.; Breit, J. S. An Investigation into the Hydrogen Storage Characteristics of $Ca(BH_4)_2/LiNH_2$ and $Ca(BH_4)_2/NaNH_2$: Evidence of Intramolecular Destabilization. *J. Phys. Chem. C* **2014**, *118*, 14759–14769.

33. Michel, K. J.; Ozoliņš, V. Native Defect Concentrations in $NaAlH_4$ and Na_3AlH_6. *J. Phys. Chem. C* **2011**, *115*, 21443–21453.

34. Michel, K. J.; Ozoliņš, V. Vacancy Diffusion in $NaAlH_4$ and Na_3AlH_6. *J. Phys. Chem. C* **2011**, *115*, 21465–21472.

35. Ivancic, T. M.; Hwang, S.-J.; Bowman, R. C.; Birkmire, D. S.; Jensen, C. M.; Udovic, T. J.; Conradi, M. S. Discovery of A New Al Species in Hydrogen Reactions of $NaAlH_4$. *J. Phys. Chem. Lett.* **2010**, *1* (15), 2412–2416.

36. Baldé, C. P.; Hereijgers, B. P. C.; Bitter, J. H.; Jong, K. P. de. Sodium Alanate Nanoparticles − Linking Size to Hydrogen Storage Properties. *J. Am. Chem. Soc.* **2008**, *130*, 6761–6765.

37. Nielsen, T. K.; Polanski, M.; Zasada, D.; Javadian, P.; Besenbacher, F.; Bystrzycki, J.; Skibsted, J.; Jensen, T. R. Improved Hydrogen Storage Kinetics of Nanoconfined $NaAlH_4$ Catalyzed with $TiCl_3$ Nanoparticles. *ACS Nano* **2011**, *5*, 4056–4064.

38. Bhakta, R. K.; Herberg, J. L.; Jacobs, B.; Highley, A.; Behrens, R.; Ockwig, N. W.; Greathouse, J. A.; Allendorf, M. D. Metal−Organic Frameworks As Templates for Nanoscale $NaAlH_4$. *J. Am. Chem. Soc.* **2009**, *131*, 13198–13199.

39. Berseth, P. A.; Harter, A. G.; Zidan, R.; Blomqvist, A.; Araújo, C. M.; Scheicher, R. H.; Ahuja, R.; Jena, P. Carbon Nanomaterials as Catalysts for Hydrogen Uptake and Release in $NaAlH_4$. *Nano Lett.* **2009**, *9*, 1501–1505.

40. Laref, A.; Ahmed, A.; Bin-Omran, S.; Luo, S. J. First-Principle Analysis of the Electronic and Optical Properties of Boron and Nitrogen Doped Carbon Mono-Layer Graphenes. *Carbon* **2015**, *81*, 179–192.

41. Kondo, T.; Casolo, S.; Suzuki, T.; Shikano, T.; Sakurai, M.; Harada, Y.; Saito, M.; Oshima, M.; Trioni, M. I.; Tantardini, G. F.; et al. Atomic-Scale Characterization of Nitrogen-Doped Graphite: Effects of Dopant Nitrogen on the Local Electronic Structure of the Surrounding Carbon Atoms. *Phys. Rev. B* **2012**, *86*, 035436.

42. Bogdanović, B.; Felderhoff, M.; Germann, M.; Härtel, M.; Pommerin, A.; Schüth, F.; Weidenthaler, C.; Zibrowius, B. Investigation of Hydrogen Discharging and Recharging Processes of Ti-Doped $NaAlH_4$ by X-Ray Diffraction Analysis (XRD) and Solid-State NMR Spectroscopy. *J. Alloys Compd.* **2003**, *350*, 246–255.

REFERENCES

1. EIA projects 28% increase in world energy use by 2040 - Today in Energy - U.S. Energy Information Administration (EIA) https://www.eia.gov/todayinenergy/detail.php?id=32912 (accessed Jun 20, 2018).

2. Olivier, J. G. J.; Schure, K. M.; Peters, J. Trends in Global CO2 and Total Greenhouse Gas Emissions. *Summ. 2017 Rep. PBL Neth. Environ. Assess. Agency Hague* **2017**.

3. Fossil Fuels — The National Academies http://needtoknow.nas.edu/energy/energy-sources/fossil-fuels/ (accessed Oct 11, 2018).

4. Winter, M.; Brodd, R. J. What Are Batteries, Fuel Cells, and Supercapacitors? *Chem. Rev.* **2004**, *104* (10), 4245–4270.

5. Armand, M.; Tarascon, J.-M. Building Better Batteries. *Nature* **2008**, *451* (7179), 652–657.

6. Huang, P.; Wang, Q.; Li, K.; Ping, P.; Sun, J. The Combustion Behavior of Large Scale Lithium Titanate Battery. *Sci. Rep.* **2015**, *5*, 7788.

7. Fuel Cell Applications - Fuel Cell Today http://www.fuelcelltoday.com/applications (accessed Jul 23, 2018).

8. Kirubakaran, A.; Jain, S.; Nema, R. K. A Review on Fuel Cell Technologies and Power Electronic Interface. *Renew. Sustain. Energy Rev.* **2009**, *13* (9), 2430–2440.

9. Barbir, F. PEM Fuel Cells. In *Fuel Cell Technology: Reaching Towards Commercialization*; Sammes, N., Ed.; Engineering Materials and Processes; Springer London: London, 2006; pp 27–51.

10. Niaz, S.; Manzoor, T.; Pandith, A. H. Hydrogen Storage: Materials, Methods and Perspectives. Renew. Sustain. Energy Rev. 2015, 50, 457–469.

11. Turner, J. A. Sustainable Hydrogen Production. Science 2004, 305 (5686), 972–974.

12. Alternative Fuels Data Center: Hydrogen Production and Distribution https://www.afdc.energy.gov/fuels/hydrogen_production.html (accessed Jul 23, 2018).

13. Navarro, R. M.; Peña, M. A.; Fierro, J. L. G. Hydrogen Production Reactions from Carbon Feedstocks: Fossil Fuels and Biomass. *Chem. Rev.* **2007**, *107* (10), 3952–3991.

14. Florin, N.; Harris, A. Hydrogen Production from Biomass. *The Environmentalist* **2007**, *27* (1), 207–215.

15. Wang, M.; Wang, Z.; Gong, X.; Guo, Z. The Intensification Technologies to Water Electrolysis for Hydrogen Production – A Review. *Renew. Sustain. Energy Rev.* **2014**, *29*, 573–588.

16. Züttel, A. Hydrogen Storage Methods. *Naturwissenschaften* **2004**, *91* (4), 157–172.

17. Hwang, H. T.; Varma, A. Hydrogen Storage for Fuel Cell Vehicles. *Curr. Opin. Chem. Eng.* **2014**, *5*, 42–48.

18. Zhou, L. Progress and Problems in Hydrogen Storage Methods. *Renew. Sustain. Energy Rev.* **2005**, *9* (4), 395–408.

19. Broom, D. P.; Webb, C. J.; Hurst, K. E.; Parilla, P. A.; Gennett, T.; Brown, C. M.; Zacharia, R.; Tylianakis, E.; Klontzas, E.; Froudakis, G. E.; et al. Outlook and Challenges for Hydrogen Storage in Nanoporous Materials. *Appl. Phys. A* **2016**, *122* (3).

20. Froudakis, G. E. Hydrogen Storage in Nanotubes & Nanostructures. *Mater. Today* **2011**, *14* (7), 324–328.

21. Rusman, N. A. A.; Dahari, M. A Review on the Current Progress of Metal Hydrides Material for Solid-State Hydrogen Storage Applications. *Int. J. Hydrog. Energy* **2016**, *41* (28), 12108–12126.

22. Graetz, J. New Approaches to Hydrogen Storage. *Chem. Soc. Rev.* **2009**, *38* (1), 73–82.

23. Rönnebro, E. C.; Majzoub, E. H. Recent Advances in Metal Hydrides for Clean Energy Applications. *MRS Bull.* **2013**, *38* (6), 452–458.

24. Oumellal, Y.; Rougier, A.; Nazri, G. A.; Tarascon, J. M.; Aymard, L. Metal Hydrides for Lithium-Ion Batteries. *Nat. Mater.* **2008**, *7* (11), 916.

25. Gaylord, N. G. Reduction with Complex Metal Hydrides. *J. Chem. Educ.* **1957**, *34* (8), 367.

26. Suda, S.; Sun, Y.-M.; Liu, B.-H.; Zhou, Y.; Morimitsu, S.; Arai, K.; Tsukamoto, N.; Uchida, M.; Candra, Y.; Li, Z.-P. Catalytic Generation of Hydrogen by Applying Fluorinated-Metal Hydrides as Catalysts. *Appl. Phys. A* **2001**, *72* (2), 209–212.

27. Sandrock, G.; Reilly, J.; Graetz, J.; Zhou, W.-M.; Johnson, J.; Wegrzyn, J. Accelerated Thermal Decomposition of AlH3 for Hydrogen-Fueled Vehicles. *Appl. Phys. A* **2005**, *80* (4), 687–690.

28. Graetz, J. Metastable Metal Hydrides for Hydrogen Storage. *ISRN Mater. Sci.* **2012**, *2012*.

29. Brower, F. M.; Matzek, N. E.; Reigler, P. F.; Rinn, H. W.; Roberts, C. B.; Schmidt, D. L.; Snover, J. A.; Terada, K. Preparation and Properties of Aluminum Hydride. *J. Am. Chem. Soc.* **1976**, *98* (9), 2450–2453.

30. Graetz, J.; Reilly, J.; Sandrock, G.; Johnson, J.; Zhou, W. M.; Wegrzyn, J. Aluminum Hydride, AlH3, as a Hydrogen Storage Compound. In *Advanced Materials for Energy Conversion III: A Symposium in Honor of Drs Gary Sandrock, Louis Schlapbach, and Seijirau Suda*; 2006; pp 57–63.

31. Srinivasan, S.; Escobar, D.; Goswami, Y.; Stefanakos, E. Effects of Catalysts Doping on the Thermal Decomposition Behavior of Zn(BH4)2. *Int. J. Hydrog. Energy* **2008**, *33* (9), 2268–2272.

32. Ley, M. B.; Jepsen, L. H.; Lee, Y.-S.; Cho, Y. W.; Bellosta von Colbe, J. M.; Dornheim, M.; Rokni, M.; Jensen, J. O.; Sloth, M.; Filinchuk, Y.; et al. Complex Hydrides for Hydrogen Storage – New Perspectives. *Mater. Today* **2014**, *17* (3), 122–128.

33. Bogdanović, B.; Schwickardi, M. Ti-Doped Alkali Metal Aluminium Hydrides as Potential Novel Reversible Hydrogen Storage Materials1. *J. Alloys Compd.* **1997**, *253*, 1–9.

34. (34) Züttel, A.; Rentsch, S.; Fischer, P.; Wenger, P.; Sudan, P. H.; Mauron, P.; Emmenegger, C. Hydrogen Storage Properties of LiBH4. *J. Alloys Compd.* **2003**, *356*, 515–520.

35. Eftekhari, A. Ordered Mesoporous Materials for Lithium-Ion Batteries. *Microporous Mesoporous Mater.* **2017**, *243*, 355–369.

36. Li, H.-Q.; Liu, R.-L.; Zhao, D.-Y.; Xia, Y.-Y. Electrochemical Properties of an Ordered Mesoporous Carbon Prepared by Direct Tri-Constituent Co-Assembly. *Carbon* **2007**, *45* (13), 2628–2635.

37. Saikia, D.; Wang, T.-H.; Chou, C.-J.; Tsai, L.-D.; Kao, H.-M. A Comparative Study of Ordered Mesoporous Carbons with Different Pore Structures as Anode Materials for Lithium-Ion Batteries. *Rsc Adv.* **2015**, *5* (53), 42922–42930.

38. Gross, A. F.; Vajo, J. J.; Van Atta, S. L.; Olson, G. L. Enhanced Hydrogen Storage Kinetics of LiBH4 in Nanoporous Carbon Scaffolds. *J. Phys. Chem. C* **2008**, *112* (14), 5651–5657.

39. Stephens, R. D.; Gross, A. F.; Atta, S. L. V.; Vajo, J. J.; Pinkerton, F. E. The Kinetic Enhancement of Hydrogen Cycling in NaAlH 4 by Melt Infusion into Nanoporous Carbon Aerogel. *Nanotechnology* **2009**, *20* (20), 204018.

40. Liu, X.; Peaslee, D.; Jost, C. Z.; Majzoub, E. H. Controlling the Decomposition Pathway of LiBH4 via Confinement in Highly Ordered Nanoporous Carbon. *J. Phys. Chem. C* **2010**, *114* (33), 14036–14041.

41. Song, Y.; Li, L.; Wang, Y.; Wang, C.; Guo, Z.; Xia, Y. Nitrogen-Doped Ordered Mesoporous Carbon with a High Surface Area, Synthesized through Organic–Inorganic Coassembly, and Its Application in Supercapacitors. *ChemPhysChem* **2014**, *15* (10), 2084–2093.

42. Zhang, L. L.; Zhao, X. S. Carbon-Based Materials as Supercapacitor Electrodes. *Chem. Soc. Rev.* **2009**, *38* (9), 2520–2531.

43. Li, W.; Liu, J.; Zhao, D. Mesoporous Materials for Energy Conversion and Storage Devices. *Nat. Rev. Mater.* **2016**, *1* (6), 16023.

44. Meng, Y.; Gu, D.; Zhang, F.; Shi, Y.; Stein, A. A Family of Highly Ordered Mesoporous Polymer Resin and Carbon Structures from Organic- Organic Self-Assembly. *Chem. Mater.* **2006**, *18* (18), 4447–4464.

45. Liu, R.; Shi, Y.; Wan, Y.; Meng, Y.; Zhao, D. Triconstituent Co-Assembly to Ordered Mesostructured Polymer- Silica and Carbon- Silica Nanocomposites and Large-Pore Mesoporous Carbons with High Surface Areas. *J. Am. Chem. Soc.* **2006**, *128* (35), 11652–11662.

46. Jun, S.; Joo, S. H.; Ryoo, R.; Kruk, M.; Terasaki, O. Synthesis of New, Nanoporous Carbon with Hexagonally Ordered Mesostructure. *J. Am. Chem. Soc.* **2000**, *122* (43), 10712–10713.

47. Vinu, A.; Ariga, K.; Mori, T.; Nakanishi, T.; Hishita, S.; Golberg, D.; Bando, Y. Preparation and Characterization of Well-Ordered Hexagonal Mesoporous Carbon Nitride. *Adv. Mater.* **2005**, *17* (13), 1648–1652.

48. Ryoo, R.; Joo, S. H.; Jun, S. Synthesis of Highly Ordered Carbon Molecular Sieves via Template-Mediated Structural Transformation. *J. Phys. Chem. B* **1999**, *103* (37), 7743–7746.

49. Sayari, A.; Yang, Y. SBA-15 Templated Mesoporous Carbon: New Insights into the SBA-15 Pore Structure. *Chem. Mater.* **2005**, *17* (24), 6108–6113.

50. Lu, A.-H.; Li, W.-C.; Schmidt, W.; Kiefer, W.; Schüth, F. Easy Synthesis of an Ordered Mesoporous Carbon with a Hexagonally Packed Tubular Structure. *Carbon* **2004**, *42* (14), 2939–2948.

51. Che, S.; Lund, K.; Tatsumi, T.; Iijima, S.; Joo, S. H.; Ryoo, R.; Terasaki, O. Direct Observation of 3D Mesoporous Structure by Scanning Electron Microscopy (SEM): SBA-15 Silica and CMK-5 Carbon. *Angew. Chem. Int. Ed.* **2003**, *42* (19), 2182–2185.

52. Joo, S. H.; Choi, S. J.; Oh, I.; Kwak, J.; Liu, Z.; Terasaki, O.; Ryoo, R. Ordered Nanoporous Arrays of Carbon Supporting High Dispersions of Platinum Nanoparticles. *Nature* **2001**, *412* (6843), 169.

53. Liang, C.; Li, Z.; Dai, S. Mesoporous Carbon Materials: Synthesis and Modification. *Angew. Chem. Int. Ed.* **2008**, *47* (20), 3696–3717.

54. Benzigar, M. R.; Talapaneni, S. N.; Joseph, S.; Ramadass, K.; Singh, G.; Scaranto, J.; Ravon, U.; Al-Bahily, K.; Vinu, A. Recent Advances in Functionalized Micro and Mesoporous Carbon Materials: Synthesis and Applications. *Chem. Soc. Rev.* **2018**, *47* (8), 2680–2721.

55. Stoyanov, S. R.; Titov, A. V.; Král, P. Transition Metal and Nitrogen Doped Carbon Nanostructures. *Coord. Chem. Rev.* **2009**, *253* (23), 2852–2871.

56. de Jongh, P. E.; Adelhelm, P. Nanosizing and Nanoconfinement: New Strategies towards Meeting Hydrogen Storage Goals. *ChemSusChem* **2010**, *3* (12), 1332–1348.

57. Ngene, P.; Nale, A.; Eggenhuisen, T. M.; Oschatz, M.; Embs, J. P.; Remhof, A.; de Jongh, P. E. Confinement Effects for Lithium Borohydride: Comparing Silica and Carbon Scaffolds. *J. Phys. Chem. C* **2017**, *121* (8), 4197–4205.

58. Adelhelm, P.; Gao, J.; Verkuijlen, M. H. W.; Rongeat, C.; Herrich, M.; van Bentum, P. J. M.; Gutfleisch, O.; Kentgens, A. P. M.; de Jong, K. P.; de Jongh, P. E. Comprehensive Study of Melt Infiltration for the Synthesis of NaAlH4/C Nanocomposites. *Chem. Mater.* **2010**, *22* (7), 2233–2238.

59. K. Nielsen, T.; Javadian, P.; Polanski, M.; Besenbacher, F.; Bystrzycki, J.; Skibsted, J.; R. Jensen, T. Nanoconfined NaAlH 4 : Prolific Effects from Increased Surface Area and Pore Volume. *Nanoscale* **2014**, *6* (1), 599–607.

60. Gao, J.; Adelhelm, P.; Verkuijlen, M. H. W.; Rongeat, C.; Herrich, M.; van Bentum, P. J. M.; Gutfleisch, O.; Kentgens, A. P. M.; de Jong, K. P.; de Jongh, P. E. Confinement of NaAlH4 in Nanoporous Carbon: Impact on H2 Release, Reversibility, and Thermodynamics. *J. Phys. Chem. C* **2010**, *114* (10), 4675–4682.

61. Carr, C. L.; Majzoub, E. H. Surface-Functionalized Nanoporous Carbons for Kinetically Stabilized Complex Hydrides through Lewis Acid–Lewis Base Chemistry. *J. Phys. Chem. C* **2016**, *120* (21), 11426–11432.

62. Bruce, P. G.; Scrosati, B.; Tarascon, J.-M. Nanomaterials for Rechargeable Lithium Batteries. *Angew. Chem. Int. Ed.* **2008**, *47* (16), 2930–2946.

63. Qiao, H.; Li, J.; Fu, J.; Kumar, D.; Wei, Q.; Cai, Y.; Huang, F. Sonochemical Synthesis of Ordered SnO2/CMK-3 Nanocomposites and Their Lithium Storage Properties. *ACS Appl. Mater. Interfaces* **2011**, *3* (9), 3704–3708.

64. Hassan, F. M.; Chen, Z.; Yu, A.; Chen, Z.; Xiao, X. Sn/SnO2 Embedded in Mesoporous Carbon Nanocomposites as Negative Electrode for Lithium Ion Batteries. *Electrochimica Acta* **2013**, *87*, 844–852.

65. Fan, J.; Wang, T.; Yu, C.; Tu, B.; Jiang, Z.; Zhao, D. Ordered, Nanostructured Tin-Based Oxides/Carbon Composite as the Negative-Electrode Material for Lithium-Ion Batteries. *Adv. Mater.* **2004**, *16* (16), 1432–1436.

66. Lei, Y.; Fournier, C.; Pascal, J.-L.; Favier, F. Mesoporous Carbon–Manganese Oxide Composite as Negative Electrode Material for Supercapacitors. *Microporous Mesoporous Mater.* **2008**, *110* (1), 167–176.

67. Yu, P.; Popov, B. N.; Ritter, J. A.; White, R. E. Determination of the Lithium Ion Diffusion Coefficient in Graphite. *J. Electrochem. Soc.* **1999**, *146* (1), 8–14.

68. Levi, M. D.; Aurbach, D. Diffusion Coefficients of Lithium Ions during Intercalation into Graphite Derived from the Simultaneous Measurements and Modeling of Electrochemical Impedance and Potentiostatic Intermittent Titration Characteristics of Thin Graphite Electrodes. *J. Phys. Chem. B* **1997**, *101* (23), 4641–4647.

69. Levi, M. D.; Wang, C.; Aurbach, D.; Chvoj, Z. Effect of Temperature on the Kinetics and Thermodynamics of Electrochemical Insertion of Li-Ions into a Graphite Electrode. *J. Electroanal. Chem.* **2004**, *562* (2), 187–203.

70. Weppner, W.; Huggins, R. A. Determination of the Kinetic Parameters of Mixed-Conducting Electrodes and Application to the System Li3Sb. *J. Electrochem. Soc.* **1977**, *124* (10), 1569–1578.

71. Wagemaker, M.; Borghols, W. J.; Mulder, F. M. Large Impact of Particle Size on Insertion Reactions. a Case for Anatase Li x TiO2. *J Am Chem Soc* **2007**, *129* (14), 4323–4327.

72. Zhou, H. Two-Phase Transition of Li-Intercalation Compounds in Li-Ion Batteries. *Mater. Today* **2014**, *17* (9), 451–463.

73. Vinu, A. Two-Dimensional Hexagonally-Ordered Mesoporous Carbon Nitrides with Tunable Pore Diameter, Surface Area and Nitrogen Content. *Adv. Funct. Mater.* **2008**, *18* (5), 816–827.

74. Bogdanović, B.; Brand, R. A.; Marjanović, A.; Schwickardi, M.; Tölle, J. Metal-Doped Sodium Aluminium Hydrides as Potential New Hydrogen Storage Materials. *J. Alloys Compd.* **2000**, *302* (1–2), 36–58.

75. Jongh, P. E. de; Allendorf, M.; Vajo, J. J.; Zlotea, C. Nanoconfined Light Metal Hydrides for Reversible Hydrogen Storage. *MRS Bull.* **2013**, *38* (6), 488–494.

76. Dymova, T. N.; Dergachev, M. Y.; Sokolov, V. Dissociation Pressure of Sodium Tetrahydroaluminate and Trisodium Hexahydroaluminate. In *Dokl. Akad. Nauk SSSR*; 1975; Vol. 224, pp 591–592.

77. Stavila, V.; Bhakta, R. K.; Alam, T. M.; Majzoub, E. H.; Allendorf, M. D.Reversible Hydrogen Storage by NaAlH4 Confined within a Titanium-Functionalized MOF-74(Mg) Nanoreactor. *ACS Nano* **2012**, *6* (11), 9807–9817.

78. Bhakta, R. K.; Herberg, J. L.; Jacobs, B.; Highley, A.; Behrens, R.; Ockwig, N. W.; Greathouse, J. A.; Allendorf, M. D. Metal−Organic Frameworks As Templates for Nanoscale NaAlH4. *J. Am. Chem. Soc.* **2009**, *131* (37), 13198–13199.

VITA

Waruni Jayawardana was born in Kandy, Sri Lanka. She obtained her Bachelor of Science degree in Applied Sciences in 2011 from University of Peradeniya, Sri Lanka. She joined University of Missouri St. Louis for her graduate studies and received a Master of Science degree in Physics in May 2014. She continued her studies further and received a Ph.D in Physics, jointly awarded by the Missouri University of Science and Technology and the University of Missouri St. Louis in December 2018.

Waruni gave two talks at the TMS Annual Meeting 2018 in Phoenix, Arizona. The names of those talks are “Electrochemical Characterization of Lithium Diffusion in Ordered Nanoporous Carbons via Voltage- relaxation GITT” and “Hydrogen Storage Using Alane Stabilized via Surface Functionalization of Nanoporous Ordered Hard Carbons”. During her graduate studies period, she was also awarded outstanding teaching assistant award.